

<https://doi.org/10.14379/iodp.proc.366.109.2018>

Site U1498¹



P. Fryer, C.G. Wheat, T. Williams, E. Albers, B. Bekins, B.P.R. Debret, J. Deng, Y. Dong, P. Eickenbusch, E.A. Frery, Y. Ichiyama, K. Johnson, R.M. Johnston, R.T. Kevorkian, W. Kurz, V. Magalhaes, S.S. Mantovanelli, W. Menapace, C.D. Menzies, K. Michibayashi, C.L. Moyer, K.K. Mullane, J.-W. Park, R.E. Price, J.G. Ryan, J.W. Shervais, O.J. Sissmann, S. Suzuki, K. Takai, B. Walter, and R. Zhang²

Keywords: International Ocean Discovery Program, IODP, *JOIDES Resolution*, Expedition 366, Site 1200, Site U1491, Site U1492, Site U1493, Site U1494, Site U1495, Site U1496, Site U1497, Site U1498, Mariana, Asùt Tesoru Seamount, Conical Seamount, Fantangisña Seamount, South Chamorro Seamount, Yinazao Seamount, Cretaceous seamount, subduction, subduction channel, forearc, seismogenic zone, mud volcano, fluid discharge, serpentinite, carbonate, harzburgite, clasts, ultramafic rock, breccia, gypsum, mudstone, chert, reef limestone, volcanic ash, guyot, CORK, CORK-Lite, screened casing

Site summary

Two holes were drilled at Site U1498 on the southwestern flank of Fantangisña Seamount (informally known as Celestial Seamount). This site is located along the southwestern flank because of its apparent stability relative to its deformed or slumped other flanks. It lies along multichannel seismic (MCS) Line EW0202 59-60. The general objective was to investigate the history of serpentinite flows by documenting their physical and compositional characteristics and their impact on the underlying pelagic-volcanic sediment. Hole U1498A was drilled close to the toe of the seamount where the serpentinite mud is ~50 m thick and penetrated an additional 100 m into the underlying pelagic muds. Hole U1498B was drilled ~700 m upslope and penetrated ~205 m of serpentinite matrix before penetrating the underlying pelagic sediment. This hole was logged using the triple combo wireline logging tool string to provide a continuous record with depth, especially through the transition from serpentinite to pelagic-volcanic sediment.

Hole U1498A penetrated 53 m of serpentinite matrix and 128.6 m of pelagic muds but only recovered 20.6 m (11%) of material, most of it in the upper 55 m of the hole. A higher percentage (32%) of material was recovered from Hole U1498B, which cored 205 m of the serpentinite mud matrix and 55 m of pelagic-volcanic sediment. This hole was sufficiently deep and stable enough to be logged with the triple combo tool string to measure magnetic susceptibility, natural gamma radiation (NGR), electrical resistivity, borehole diameter, and borehole fluid temperature. The tool string logged the transition to the subserpentinite sediments and reached to within 31 m of the bottom of the borehole.

Contents

- 1 Site summary
- 2 Background and objectives
- 4 Operations
- 5 Lithostratigraphy
- 12 Petrology
- 18 Structure
- 20 Fluid geochemistry
- 19 Rock and sediment geochemistry
- 23 Microbiology
- 23 Physical properties
- 30 Downhole measurements
- 31 Paleomagnetism
- 34 References

Site U1498 consists of a wide variety of materials, including multicolored serpentinite sands and silts, bluish gray serpentinite muds with ultramafic rock clasts (stones and boulders), metabasite boulders (Cores 366-U1498B-21R and 23R), cherty limestone (Core 21R), and microbreccia clasts that contain droplets of boninite glass, boulders of serpentinitized harzburgite, microfossiliferous sediment, and metavolcanic rocks in a vitric mesostasis (Core 366-U1498A-3R). These clasts and boulders are invariably embedded within serpentinite pebbly mud.

The clast-poor colorful serpentine sequences of lithostratigraphic Subunit IIIA in Hole U1498A are composed of aragonite-enriched brownish serpentinite mud (as much as 5% in Sample 4R-2, 45 cm), light green layers with clear serpentine grains, and a magnetite-enriched dark blue layer; they are exactly comparable with Unit I in Hole U1492A in both color and mineral composition. Because aragonite was suggested to be the product of reaction between serpentinite mudflow pore fluid and seawater and the limonite or hematite in the brownish layer suggests oxidation of magnetite, we infer that the brown and light green layers represent redox boundaries within a sequence of serpentinite mudflows.

Within Core 366-U1498B-21R, metabasite overlies cherty limestone and the preserved primary contact between them is inverted. The texture and mineralogical composition of both the metabasite (greenstone with chlorite and amphibole) and cherty limestone indicate low- to medium-grade metamorphic overprint of these lithologies. Preserved cataclastic faults and extensional structures within these metamorphic rocks (high-angle normal faults and extensional veins) might be related either to shearing within the subduction channel and bending of the lower plate during subduction or to

¹ Fryer, P., Wheat, C.G., Williams, T., Albers, E., Bekins, B., Debret, B.P.R., Deng, J., Dong, Y., Eickenbusch, P., Frery, E.A., Ichiyama, Y., Johnson, K., Johnston, R.M., Kevorkian, R.T., Kurz, W., Magalhaes, V., Mantovanelli, S.S., Menapace, W., Menzies, C.D., Michibayashi, K., Moyer, C.L., Mullane, K.K., Park, J.-W., Price, R.E., Ryan, J.G., Shervais, J.W., Sissmann, O.J., Suzuki, S., Takai, K., Walter, B., and Zhang, R., 2018. Site U1498. In Fryer, P., Wheat, C.G., Williams, T., and the Expedition 366 Scientists, *Mariana Convergent Margin and South Chamorro Seamount*. Proceedings of the International Ocean Discovery Program, 366: College Station, TX (International Ocean Discovery Program). <https://doi.org/10.14379/iodp.proc.366.109.2018>

² Expedition 366 Scientists' addresses.

MS 366-109: Published 7 February 2018

This work is distributed under the [Creative Commons Attribution 4.0 International](https://creativecommons.org/licenses/by/4.0/) (CC BY 4.0) license. 

faulting during the early stages of exhumation. In addition, the deformed sediments appear to contain microfossils such as radiolarians that are common in older sediments of the Pacific plate, and the presence of ultracataclasite requires severe brittle deformation that is not likely to occur in sediments lying on top of the upper plate but can begin as the Pacific plate deforms on approach to the trench and is typical within the subduction channel. For these reasons, the metabasite-carbonate interval is tentatively inferred to be a remnant of a subducted guyot from the Pacific plate. The lowermost cored intervals in Holes U1498A and U1498B are deposits of microfossil-bearing volcanic ash defining the seafloor upon which the mud volcano was built.

Similar to samples from the summit site (U1497) at Fantangisña Seamount, interstitial water CH_4 and C_2H_6 concentrations were below detection levels in samples from Hole U1498A; however, CH_4 and C_2H_6 were detected in several samples from Hole U1498B. The sample with the highest methane concentration had a C_1/C_2 ratio of 50. Similarly, dissolved hydrogen is below the detection limit in samples from Hole U1498A but not Hole U1498B. Only one sample had a measurable acid volatile sulfide (AVS) concentration (Section 366-U1498B-23R-3).

Seventeen whole-round samples were collected for pore water extraction. The two holes at Site U1498 reflect markedly different conditions in terms of their interstitial water chemical profiles. Chemical profiles from Hole U1498A, the farthest from the summit, are similar to those from the flanks of Yinazao Seamount (Site U1491). Here, pore waters have a seawater-dominated signature upon which diagenetic reactions with serpentinite muds, clasts, and sands and modified sediments impart changes to some ion profiles. In contrast, Hole U1498B is similar to Hole 779A on the flank of Conical Seamount, drilled during Ocean Drilling Program (ODP) Leg 125 (Mottl, 1992), where the interstitial water pH is consistently >10.5 at depths greater than 50 meters below seafloor (mbsf), consistent with ongoing serpentinitization.

The interstitial water “fingerprint” of the deep-sourced fluid (e.g., Site U1497) is evident in profiles of major and minor ions in Hole U1498B. Pore waters have elevated Sr and low B, K, Na, and Cl concentrations and salinity relative to bottom water. Imprinted upon these general trends are diagenetic reactions such as differences in Ca concentrations, perhaps indicating some diagenetic removal or production of Ca.

Samples were collected for shore-based microbiological analyses. To assess possible artifacts from drilling operations, tracers were pumped into the drill string prior to and during core recovery. Tracer analyses indicate that most of the whole-round samples collected for microbiology are suitable for shore-based analyses.

Physical property measurements highlight the heterogeneous materials described in the different lithostratigraphic units of the relatively low recovery Holes U1498A and U1498B. In the upper portion of each hole, only ultramafic rock clasts were recovered (e.g., Subunits IIA and IIB in Hole U1498A; Unit I in Hole U1498B); however, physical properties measurements on these clasts were consistent with others sampled during this expedition (e.g., Site U1496; see [Physical properties](#) in the Site U1496 chapter [Fryer et al., 2018f]). Measured physical properties of the serpentinite mud are consistent with those recovered from the southern flank of the Asùt Tesoru Seamount (Sites U1493–U1495; see [Physical properties](#) in the Sites U1493, U1494, and U1495 chapter [Fryer et al., 2018e]) and differ from those observed at active summit sites (e.g., Sites U1492 and Site U1496; see [Physical properties](#) in the Site U1492 chapter and [Physical properties](#) in the Site U1496 chapter

[Fryer et al., 2018d, 2018f]). In comparison to these summit sites, the serpentinite mud units from Holes U1498A and U1498B have higher average bulk densities ($2.0\text{--}2.3\text{ g/cm}^3$), higher P -wave velocities ($1700\text{--}1900\text{ m/s}$), higher thermal conductivities ($1.5\text{--}2.0\text{ W/[m}\cdot\text{K]}$), and lower porosities ($30\%\text{--}40\%$). Such materials from the flanks of a serpentinite mud volcano likely have been affected by long-term consolidation and/or low-temperature diagenetic processes, as well as by gravitational remobilization and sliding of the material along the flank.

Beneath the serpentinite matrix lies variably consolidated volcanic and pelagic sediments. These materials were reached at ~ 53 and ~ 205 mbsf in Holes U1498A and U1498B, respectively. Relative to the upper serpentinite muds, these deposits show lower bulk densities of $1.5\text{--}1.7\text{ g/cm}^3$ associated with higher porosities of $50\%\text{--}60\%$. These values probably reflect normal compaction processes compared to the overlying serpentinite muds, where additional post-depositional porosity-reducing processes likely occur, such as ongoing serpentinitization (see [Fluid geochemistry](#)).

The downhole log data show excellent agreement with the equivalent shipboard physical property data. The NGR data indicate that 9 m of pelagic sediments at the seabed were not recovered in cores and also show the cherty limestone and metabasalt units. Two possible internal flow boundaries marked by pelagic sediments may be present at 118 and 137 mbsf, based on small peaks in the NGR data. All three sensors, NGR, magnetic susceptibility, and resistivity, responded to the change in lithology at the base of the serpentinite mudflows. The resistivity data are also useful for highlighting very large clasts in the serpentinite mudflows.

The shipboard NRM of all archive section halves and 34 representative discrete samples from Holes U1498A and U1498B were measured using the shipboard superconducting rock magnetometer (SRM). Relatively high values of both magnetization and bulk magnetic susceptibility of discrete samples are related to ultramafic rocks, particularly dunites and peridotite clasts with magnetite-rich veins. Lastly, a strong overprint by the drilling process was evident, with values as high as 1 A/m even after 20 mT demagnetization.

Background and objectives

Site U1498 (proposed Site MAF-10B) is located on the southwestern flank of Fantangisña Seamount (Figure [F1](#)). Fantangisña Seamount is located at $16^\circ 32.25'\text{N}$, $147^\circ 13.25'\text{E}$, about 62 km from the trench (see Figure [F1](#) in the Expedition 366 summary chapter [Fryer et al., 2018b]). The base of the seamount is about 14 km above the subducting Pacific plate (Oakley et al., 2007). The forearc in the vicinity of the seamount was mapped (Oakley et al., 2007) with Hawaii Mapping Research Group's shallow-towed (60–100 m) bathymetry and side-scan system, MR1 (Rognstad, 1992). The edifice lies on the northern edge of a prominent forearc block that trends northwest. Side-scan backscatter of the seamount shows high intensity over the summit of the edifice and several deep erosional channels on the western flanks, suggesting rough seafloor texture on a local scale. At the base of the western flank of the seamount, numerous large blocks, as wide as 2 km, are the result of slumps that brought down large portions of the seamount (Oakley et al., 2007). A channel in the southwestern flank of the edifice may represent the boundary of a slump scar because the bathymetry curves concave toward the northwest, typical of a headwall slump scarp. In contrast, large mass-wasting structures are not apparent on the eastern or southern to southwestern flanks.

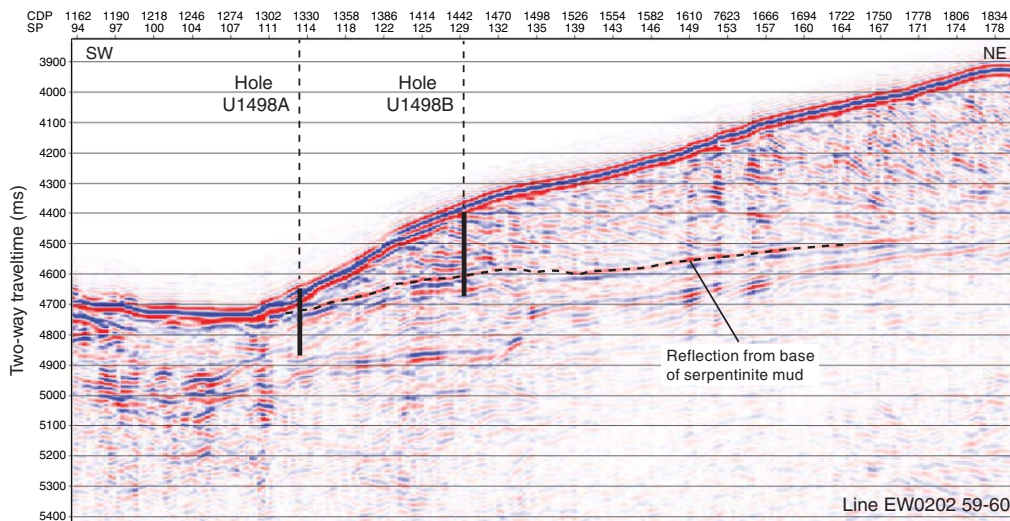
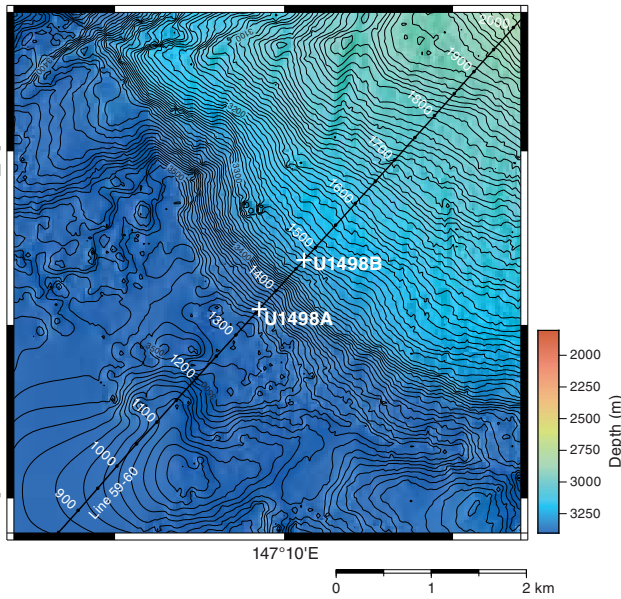
Site U1498 was located along the lower slope because of its apparent stability relative to its deformed or slumped other flanks and because it lies along MCS Line EW0202 59-60 (Figures F1, F2). The general objective was to elucidate the history of serpentinite flows by documenting their physical and chemical characteristics and

their impact on the underling pelagic-volcanic sediment. Specific objectives were to (1) intersect sediment and serpentinite mudflows and enclosed rock clasts on the distal-slope region of the southwestern flank; (2) date discrete mudflows paleontologically, should there be sediment layers between them; (3) determine variability of serpentinite mudflow and rock clast compositions and textures, as well as thicknesses of mudflow units; (4) investigate potential systematic variability in the degree of serpentinization within the flank and changes in physical properties; (5) examine transport and potential deformation characteristics of old mudflows in contact with pelagic/volcanic sediment; (6) provide an assessment of pore fluid composition; and (7) collect samples for microbiological analysis.

Figure F1. Bathymetric map of Fantangisña Seamount flank region, Holes U1498A and U1498B, and ship tracks for MCS Lines EW0202 59-60 with common midpoints labeled. Bathymetry data was collected by Simrad EM300 during a 2003 R/V *Thomas G. Thompson* cruise (Oakley et al., 2008).

To complete the stated objectives at this site, the plan was to drill two boreholes using the rotary core barrel (RCB) because the advanced piston corer (APC)/extended core barrel (XCB) system is inefficient to get to the desired depth in this mixed (rock, sand, and clay) serpentinite matrix. The goal was to drill one hole close to the toe of the seamount where the serpentinite is ~50 m thick and to penetrate another 100 m into the underlying pelagic/volcanic muds to collect sufficient material to date and assess the potential effects of serpentinite deposition. This hole (U1498A) is located about 1.4 km from the original planned position (Fryer et al., 2016). The second hole (U1498B) is located ~700 m upslope, where we anticipated encountering ~200 m of serpentinite matrix before penetrating the underlying pelagic sediment. Provided this hole was stable, the goal was to log it with the triple combo logging sensors to provide a continuous record with depth, especially through the transition from serpentinite to the underlying pelagic/volcanic sediment. Results from analysis of materials from the two holes will allow us to potentially correlate individual flows and to assess changes in flow properties as a function of distance downslope.

Figure F2. MCS Line EW0202 59-60 and Holes U1498A and U1498B with the estimated depth of penetration (Oakley et al., 2008; Oakley, 2008). The horizontal dashed line is the reflector that defines the contact between the serpentinite matrix and underlying pelagic sediment, which was recovered from both holes.



Operations

Hole U1498A

The 6.1 nmi transit to Site U1498 from Hole U1497D ended at 2300 h on 23 January 2017 (Table T1). The seafloor was eventually tagged at 0615 h on 24 January, establishing a seafloor depth of 3507.5 meters below rig floor (mbrf), which was 6.5 m below the deepest depth range provided in the *Scientific Prospectus* and 142.1 m deeper than the interpreted depth based on data from the precision depth recorder depth. Hole U1498A was spudded at 0620 h, and RCB coring continued until 1800 h on 25 January with the recovery of Core 19R from 181.6 mbsf (3689.1 mbrf). The pipe was pulled clear of the seafloor at 1930 h, ending Hole U1498A.

Hole U1498B

The positioning beacon was released and recovered because the 706 m move was thought to be marginal for dynamic positioning (DP) operations. The drill string was pulled to 3021.0 mbrf, and the

DP move was completed at 0035 h on 26 January 2017 (Table T1). The vibration isolated television (VIT)/subsea camera was deployed to determine the depth of the seafloor. At 0300 h, the seafloor was tagged, establishing a depth of 3296.0 mbrf. Hole U1498B was spudded at 0510 h on 26 January. RCB coring continued for the next few days, recovering Cores 1R–27R to 260 mbsf. The last core on deck was at 1730 h on 29 January. The bit was released to prepare for wireline logging. The triple combo tool string (magnetic susceptibility, NGR, resistivity, temperature, and caliper sensors) was prepared without nuclear sources and run in the hole. The casing remained ~54 m into the hole to ensure hole stability. A ledge prevented the logging sensors from reaching the lower 31 m of the hole; however, there was a sufficient amount of open hole for the 33 m long logging string to sense the transition from rock/serpentinite to pelagic/volcanic mud at 205 mbsf, a depth based on drilling operations. The logging tool string was laid out by 0530 h on 30 January, and the drill string was recovered. The ship was under way to Hong Kong at 1530 h on 30 January.

Table T1. Site U1498 coring summary. DRF = drilling depth below rig floor, DSF = drilling depth below seafloor, CSF-A, core depth below seafloor, Method A. Core type: R = rotary core barrel (RCB). (Continued on next page.) [Download table in CSV format.](#)

Hole U1498A							Hole U1498B				
Latitude: 16°27.0898'N							Latitude: 16°27.3716'N				
Longitude: 147°09.8502'E							Longitude: 147°10.1166'E				
Water depth (m): 3496.21							Water depth (m): 3284.7				
Date started (UTC): 1300 h, 23 January 2017							Date started (UTC): 0930 h, 25 January 2017				
Date finished (UTC): 0930 h, 25 January 2017							Date finished (UTC): 0530 h, 30 January 2017				
Time on hole (days): 1.85							Time on hole (days): 4.83				
Seafloor depth DRF (m): 3507.5							Seafloor depth DRF (m): 3296				
Seafloor depth est. method: TAG							Seafloor depth est. method: TAG				
Rig floor to sea level (m): 11.29							Rig floor to sea level (m): 11.3				
Penetration DSF (m): 181.6							Penetration DSF (m): 260				
Cored interval (m): 181.6							Cored interval (m): 260				
Recovered length (m): 20.59							Recovered length (m): 82.82				
Recovery (%): 11.34							Recovery (%): 31.85				
Total cores (no.): 19							Total cores (no.): 27				
RCB cores (no.): 19							RCB cores (no.): 27				

Core	Top depth drilled DSF (m)	Bottom depth drilled DSF (m)	Interval advanced (m)	Recovered length (m)	Curated length (m)	Core recovery (%)	Top depth cored CSF-A (m)	Bottom depth cored CSF-A (m)	Core on deck date (2017)	Core on deck time UTC (h)
366-U1498A-										
1R	0	6.3	6.3	5.40	5.40	86	0.0	5.40	23 Jan	2140
2R	6.3	16.0	9.7	0.14	0.26	1	6.3	6.56	24 Jan	0225
3R	16.0	25.8	9.8	1.62	2.03	17	16.0	18.03	24 Jan	0420
4R	25.8	35.6	9.8	4.15	4.15	42	25.8	29.95	24 Jan	0710
5R	35.6	45.4	9.8	2.81	2.81	29	35.6	38.41	24 Jan	0945
6R	45.4	55.1	9.7	0.11	0.11	1	45.4	45.51	24 Jan	1110
7R	55.1	64.8	9.7	0.03	0.03	0	55.1	55.13	24 Jan	1230
8R	64.8	74.6	9.8		2.81		64.8	64.80	24 Jan	1400
9R	74.6	84.3	9.7	0.20	0.21	2	74.6	74.81	24 Jan	1550
10R	84.3	94.1	9.8	0.15	0.15	2	84.3	84.45	24 Jan	1725
11R	94.1	103.8	9.7		2.81		94.1	94.10	24 Jan	1905
12R	103.8	113.5	9.7	0.10	0.10	1	103.8	103.90	24 Jan	2045
13R	113.5	123.2	9.7	1.74	1.87	18	113.5	115.37	24 Jan	2235
14R	123.2	132.9	9.7	0.18	0.18	2	123.2	123.38	25 Jan	0020
15R	132.9	142.7	9.8	1.65	1.65	17	132.9	134.55	25 Jan	0200
16R	142.7	152.4	9.7	1.00	1.00	10	142.7	143.70	25 Jan	0330
17R	152.4	162.2	9.8	0.40	0.43	4	152.4	152.83	25 Jan	0505
18R	162.2	171.9	9.7	0.76	0.76	8	162.2	162.96	25 Jan	0630
19R	171.9	181.6	9.7	0.15	0.15	2	171.9	172.05	25 Jan	0800
Hole U1498A totals:			181.6	20.59	26.91					
366-U1498B-										
1R	0	9.5	9.5				0.0	0.00	25 Jan	1955
2R	9.5	19.2	9.7	0.47	0.37	5	9.5	9.87	25 Jan	2120
3R	19.2	28.9	9.7	1.82	2.20	19	19.2	21.40	25 Jan	2315

Table T1 (continued).

Core	Top depth drilled DSF (m)	Bottom depth drilled DSF (m)	Interval advanced (m)	Recovered length (m)	Curated length (m)	Core recovery (%)	Top depth cored CSF-A (m)	Bottom depth cored CSF-A (m)	Core on deck date (2017)	Core on deck time UTC (h)
4R	28.9	34.7	5.8	1.89	2.36	33	28.9	31.26	26 Jan	0120
5R	34.7	44.4	9.7	1.64	2.07	17	34.7	36.67	26 Jan	0410
6R	44.4	54.1	9.7	0.98	1.36	10	44.4	45.76	26 Jan	0735
7R	54.1	63.8	9.7	3.97	4.28	41	54.1	58.38	26 Jan	1055
8R	63.8	73.6	9.8	4.58	4.73	47	63.8	68.53	26 Jan	1435
9R	73.6	83.3	9.7	1.61	1.61	17	73.6	75.21	26 Jan	1810
10R	83.3	93.1	9.8	3.02	3.02	31	83.3	86.32	26 Jan	2140
11R	93.1	102.8	9.7	5.87	5.87	61	93.1	98.97	27 Jan	0130
12R	102.8	112.5	9.7	6.79	6.79	70	102.8	109.59	27 Jan	0500
13R	112.5	122.2	9.7	3.54	3.84	36	112.5	116.34	27 Jan	0855
14R	122.2	132.0	9.8	6.95	6.95	71	122.2	129.15	27 Jan	1255
15R	132.0	141.7	9.7	3.60	3.60	37	132.0	135.60	27 Jan	1725
16R	141.7	151.4	9.7	0.32	0.32	3	141.7	142.02	27 Jan	2055
17R	151.4	161.2	9.8	9.22	9.22	94	151.4	160.62	28 Jan	0325
18R	161.2	170.9	9.7	0.89	1.14	9	161.2	162.09	28 Jan	0635
19R	170.9	180.6	9.7	5.69	5.69	59	170.9	176.59	28 Jan	1010
20R	180.6	185.9	5.3	0.87	0.85	16	180.6	181.45	28 Jan	1325
21R	185.9	190.4	4.5	2.46	2.46	55	185.9	188.36	28 Jan	1700
22R	190.4	200.1	9.7	8.08	8.08	83	190.4	198.48	28 Jan	2135
23R	200.1	209.9	9.8	2.80	2.84	29	200.1	202.94	29 Jan	0105
24R	209.9	219.6	9.7	2.06	2.06	21	209.9	211.96	29 Jan	0235
25R	219.6	229.3	9.7	0.67	0.67	7	219.6	220.27	29 Jan	0410
26R	229.3	239.1	9.8	1.54	1.54	16	229.3	230.84	29 Jan	0540
27R	239.1	260.0	20.9	1.49	1.49	7	239.1	240.59	29 Jan	0725
Hole U1498B totals:			260.0	82.82	85.41					

Lithostratigraphy

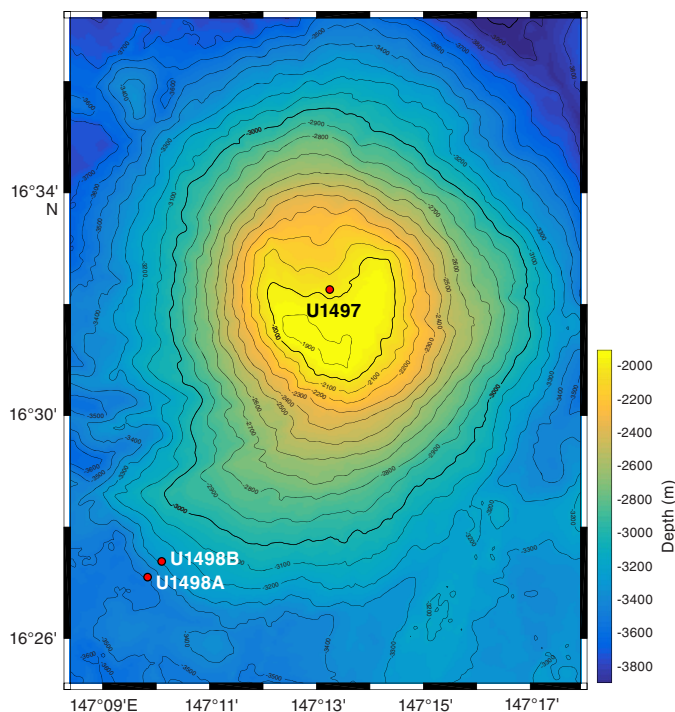
Site U1498 is located on the flank of Fantangisña Seamount (Figure F3). Hole U1498A is on the extreme southwestern flank, very close to the bottom of the physical seamount (3507.5 mbrf), and Hole U1498B is ~700 m upslope and closer to the summit (3296.0 mbrf). Lithologies recovered at Site U1498 include yellowish oxidized muds with pelagic microfossils; intercalated blue, green, and yellow-orange serpentinite silts and sands; partially serpentinitized ultramafic rocks (harzburgite and dunite); mafic metavolcanic rocks; and nannofossil- and volcanic ash-rich sedimentary rocks (siltstones and fine sandstones). In addition, Hole U1498B returned a large (2 m) compound clast of ultramafic rock, mafic metavolcanic rock, metalimestone, and metachert, all suspected to be part of a subducted Cretaceous seamount.

The lithostratigraphy changes significantly between Holes U1498A and U1498B. In Hole U1498A, we achieved a total depth of 181.6 mbsf (Figure F4; Table T2), and in Hole U1498B, we achieved a total depth of 260.0 mbsf (Figure F5; Table T3); both holes recovered a significant section of Miocene to Pliocene pelagic sediment and volcanic ash from below the mud volcano. Both holes were drilled using the RCB system, which results in low unconsolidated material yields but recovers hard rock layers, clasts, and indurated materials.

Hole U1498A

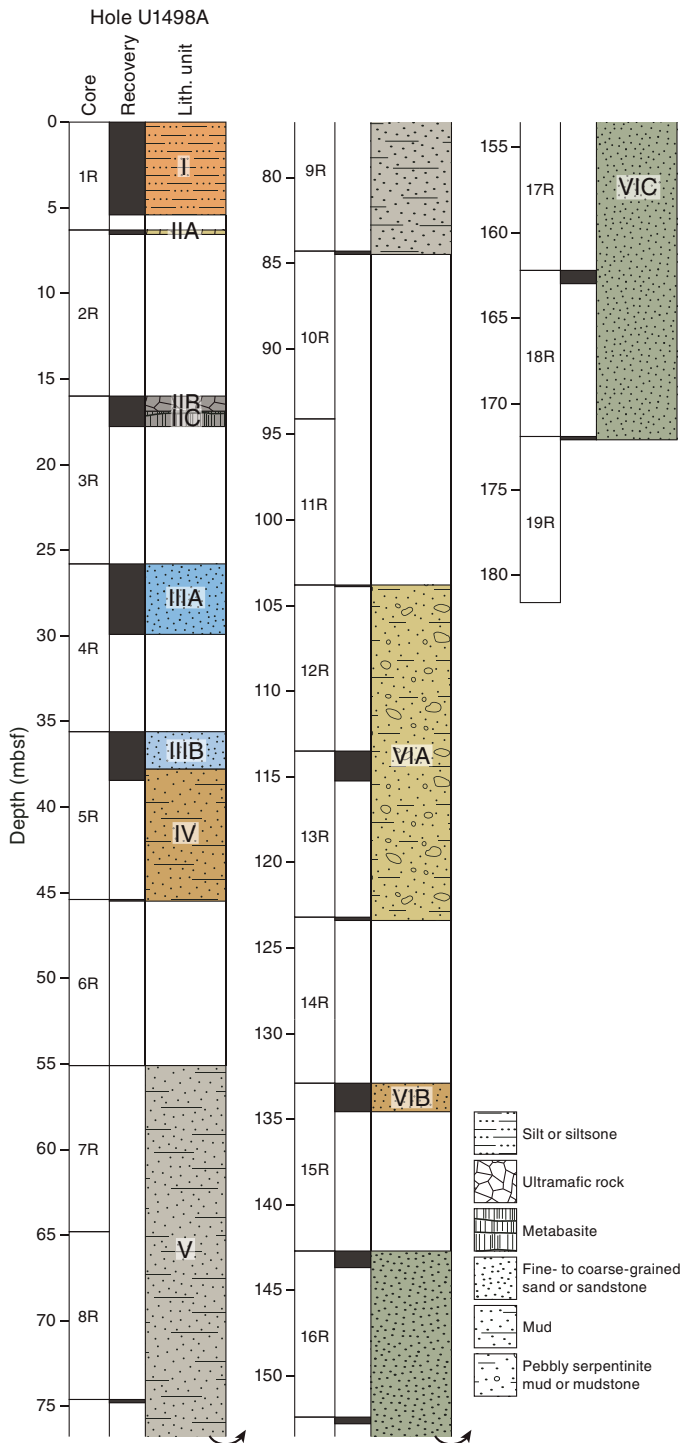
Hole U1498A was cored to 181.6 mbsf and recovered 20.59 m of core (11.3% recovery). Hole U1498A cores consist of six units (Figure F4; Table T2). Unit I is brown, fine-grained muddy silt with abundant microfossils and a few highly altered ultramafic clasts. Unit II contains serpentinitized ultramafic rock clasts (harzburgite and dunite) and mafic metavolcanic rock clasts, with no matrix returned. Unit III consists of intercalated blue, green, and yellow-orange serpentinite sand and silt. Unit IV is similar but also contains

Figure F3. Location map of Site U1498 showing its position on the flanks of Fantangisña Seamount.



volcanic ash and nannofossils. Unit V had minimal recovery of mafic metavolcanic and ultramafic rock clasts, with scraps of silty ash matrix. Unit VI consists of nannofossil- and ash-rich silts and sands, some of which are partially lithified. The common occurrence of Miocene- or Pliocene-age nannofossils in Unit VI shows that this hole penetrated the mud volcano edifice and sampled the

Figure F4. Lithostratigraphy, Hole U1498A. Colors are according to Figure F5 in the Expedition 366 methods chapter (Fryer et al., 2018a) with slight changes for subunits or when representative for the particular unit.



underlying pelagic sediments, which predate formation of the volcano. Examples of several lithostratigraphic units from Hole U1498A are shown in Figure F6.

Unit I

Interval: 366-U1498A-1R-1, 0 cm, to 1R-CC, 14 cm
Depth: 0–5.40 mbsf

Unit I is 5.40 m thick and consists of brown microfossil- and nannofossil-rich muddy silt with sandy horizons composed of serpentinite detritus. The sandy serpentinite-rich layers are yellowish in color from the oxidized ultramafic minerals. Small, ~2 cm pebbles of highly altered and oxidized ultramafic rock are rare (Sections 1R-2, 14.5–17 cm, 1R-2, 31–41 cm, and 2R-3, 13–15 cm), but the bottom of the core catcher (Section 1R-CC, 8 cm) contains a cluster of fragments of highly altered, subangular ultramafic pebbles and one pebble of fresher ultramafic rock. This cluster probably represents a single fragmented ultramafic rock clast.

Unit II

Interval: 366-U1498A-2R-CC, 0 cm, to 3R-3, 57 cm
Depth: 6.30–18.03 mbsf

Unit II is 11.73 m thick and consists almost entirely of individual clasts with no matrix. It is divided into three subunits based on the clast types and gaps in the recovery. The clasts are representative of some of the materials found at those depths but can by no means be considered to be a complete inventory of material present in the stratigraphy because of unconsolidated material washout during rotary coring.

Subunit IIA

Interval: 366-U1498A-2R-CC, 0 cm, to 2R-CC, 26 cm
Depth: 6.30–6.56 mbsf

Subunit IIA is 0.26 m thick and consists of serpentinitized ultramafic rock clasts, with no matrix material recovered. The clasts are strongly weathered, and all but one brecciated clast are massive and largely oxidized to orange-yellow in color. Some clasts are crosscut by serpentine veins, and the breccia contains some calcite cement. One clast is not oxidized; it is dark blue-gray harzburgite with orthopyroxene altered to bastite and multiple serpentine veins.

There is a 10 m gap between the base of this subunit and Subunit IIB.

Subunit IIB

Interval: 366-U1498A-3R-1, 0 cm, to 3R-2, 85 cm
Depth: 16.00–16.89 mbsf

Subunit IIB is 0.89 m thick and consists of serpentinitized ultramafic rock clasts, with no matrix material recovered, except in the uppermost 10 cm of Section 3R-1, which contains two separate pieces of blue sandy clay with granules of black serpentinite and orange oxidized serpentinite. The clasts, which begin in Section 3R-2 at 0 cm, are relatively fresh and unoxidized, consisting of five harzburgite clasts and two dunite clasts plus several small ultramafic rock fragments. All are dark gray to black, and one of the harzburgite pieces appears to contain a strong preferred fabric defined by aligned orthopyroxene grains. Several of these ultramafic clasts may be less than 50% serpentinitized. Others have thin serpentine veins, and some have wider veins with dark gray halos (which may also be cut by thin veins of pale green to white serpentine, suggesting volume expansion).

Subunit IIC

Interval: 366-U1498A-3R-2, 85 cm, to 3R-3, 57 cm
Depth: 16.89–18.03 mbsf

Subunit IIC is 1.14 m thick and consists of mafic metavolcanic and polymictic breccia clasts; the breccia is composed of small (2–3

Table T2. Lithostratigraphic units, Hole U1498A. [Download table in CSV format.](#)

Lith. unit	Top depth (mbsf)	Top core, section, interval (cm)	Bottom depth (mbsf)	Bottom core, section, interval (cm)	Unit thickness (m)	Lithology
		366-U1498A-		366-U1498A-		
I	0	1R-1, 0	5.40	1R-CC, 14	5.40	Brown muddy silt with microfossils
II	6.30	2R-CC, 0	18.03	3R-3, 57	11.73	See below
IIA	6.30	2R-CC, 0	6.56	2R-CC, 26	0.26	Serpentinized ultramafic rock clasts, no matrix
IIB	16.00	3R-1, 0	16.89	3R-2, 85	0.85	Serpentinized ultramafic rock clasts, no matrix
IIC	16.89	3R-2, 85	18.03	3R-3, 57	1.18	Mafic metavolcanics, breccias containing metavolcanics, minor serpentinized rocks
IIIA	25.80	4R-1, 0	29.95	4R-CC, 27	4.15	Layered blue, green, and yellow-orange serpentinite sand and silt, no clasts
IIIB	35.60	5R-1, 0	37.79	5R-3, 4	2.19	Blue sandy serpentinite mud with green sandy serpentine intercalations
IV	37.79	5R-3, 4	45.51	6R-CC, 11	7.72	Silty serpentinite mud with sand and volcanic ash
V	55.10	7R-CC, 0	84.45	10R-CC, 15	29.35	Minimal recovery (1.3%) of mixed ultramafic and volcanic rock clasts with some silty ash
VIA	103.80	12R-CC, 0	123.38	14R-CC, 18	19.58	Nannofossil-rich silty mud with ash; ultramafic rock and sandstone clasts; yellowish brown to gray-brown
VIB	132.90	15R-1, 0	134.55	15R-CC, 8	1.65	Mud, silt, and sand with ash; dark yellow-brown
VIC	142.70	16R-1, 0	172.05	19R-CC, 15	29.35	Nannofossil-rich sand with ash; dark greenish gray

cm) metavolcanic clasts in a matrix of fine-grained volcanic ash and serpentinite granules. Clasts of serpentinized ultramafic rock are rare but present in these breccias. Some of the metavolcanic clasts have small vesicles filled with a blue clay mineral, probably saponite, which indicates that their metamorphic grade is no higher than zeolite facies. They also have low TiO₂ concentrations (<0.4 wt%, as determined by pXRF), suggesting that they may be boninite lavas from beneath the mud volcano. There are also several serpentinized ultramafic rock clasts (Sections 3R-2 [Pieces 17 and 18] and 3R-3 [Pieces 1, 2, 6A, and 7]).

Unit III

Interval: 366-U1498A-4R-1, 0 cm, to 5R-3, 4 cm
Depth: 25.80–37.79 mbsf

Unit III is 11.99 m thick and divided into two subunits because of a ~6 m gap between them and subtle mineralogical differences.

Subunit IIIA

Interval: 366-U1498A-4R-1, 0 cm, to 4R-CC, 27 cm
Depth: 25.80–29.95 mbsf

Subunit IIIA is 4.15 m thick and consists of layered serpentinite silt and sand with beds of pelagic sediment, commonly internally graded. There is one dunite clast at the top of the unit (possible fall-in); otherwise, this unit is completely free of lithic clasts. Individual beds range from about 1 to 45–50 cm thick, and the bedding is typically lenticular. Grain size varies from silt to very coarse sand between beds, but individual beds are relatively well sorted. Contacts are sharp and may be horizontal, curvilinear, or inclined. Structures include internal flow structures (sliding and slumping folds) and internal layer unconformities.

Subunit IIIB

Interval: 366-U1498A-5R-1, 0 cm, to 5R-3, 4 cm
Depth: 35.60–37.79 mbsf

Subunit IIIB is 2.19 m thick and essentially identical to Subunit IIIA but is separated from it by a 6 m gap. Subunit IIIB consists of layered serpentinite silt and sand with beds of pelagic sediment, commonly internally graded, with few small lithic clasts (<1 cm diameter) only as fall-in in Section 5R-1, 5–11 cm, and in place in Section 5R-3, 37–42 cm. Individual beds range from about 1 to 45–57

cm thick, and the bedding typically is lenticular. There are gradual transitions from blue to green serpentinite sand in some layers. Grain size varies from silt to very coarse sand among beds, but individual beds are relatively well sorted. Contacts are sharp and may be horizontal, curvilinear, or inclined. Sedimentary structures include internal flow structures (sliding and slumping folds) and internal layer unconformities. Serpentine fibers are common in the lower half of this unit.

Unit IV

Interval: 366-U1498A-5R-3, 4 cm, to 6R-CC, 11 cm
Depth: 37.79–45.51 mbsf

Unit IV is 7.72 m thick and consists of laminated silty sand and volcanic ash with bluish gray serpentinite mud laminae (2 mm thick) and stratified, normally graded pelagic silt to fine sand. Rare clasts in the middle part of the unit are mainly ultramafic rock with coarse sand- to pebble-sized grains. This unit is characterized by the occurrence of serpentine fibers throughout. There is a 7 m gap between Sections 5R-3 and 6R-CC.

Unit V

Interval: 366-U1498A-7R-CC, 0 cm, to 10R-CC, 15 cm
Depth: 55.10–84.45 mbsf

Unit V is 29.35 m thick and consists of individual clasts and short sediment intervals from three cores (7R, 9R, and 10R) with minimal recovery; these cores returned a total of 39 cm of core from 29.35 m drilled (1.3% recovery). It is inferred that most of this unit consists of unconsolidated sand and silt that washed out during drilling. Recovery includes clasts of serpentinized ultramafic rock (2–5 cm in diameter) and metavolcanic rock (2 cm), as well as short (4–5 cm) intervals of unconsolidated silty ash.

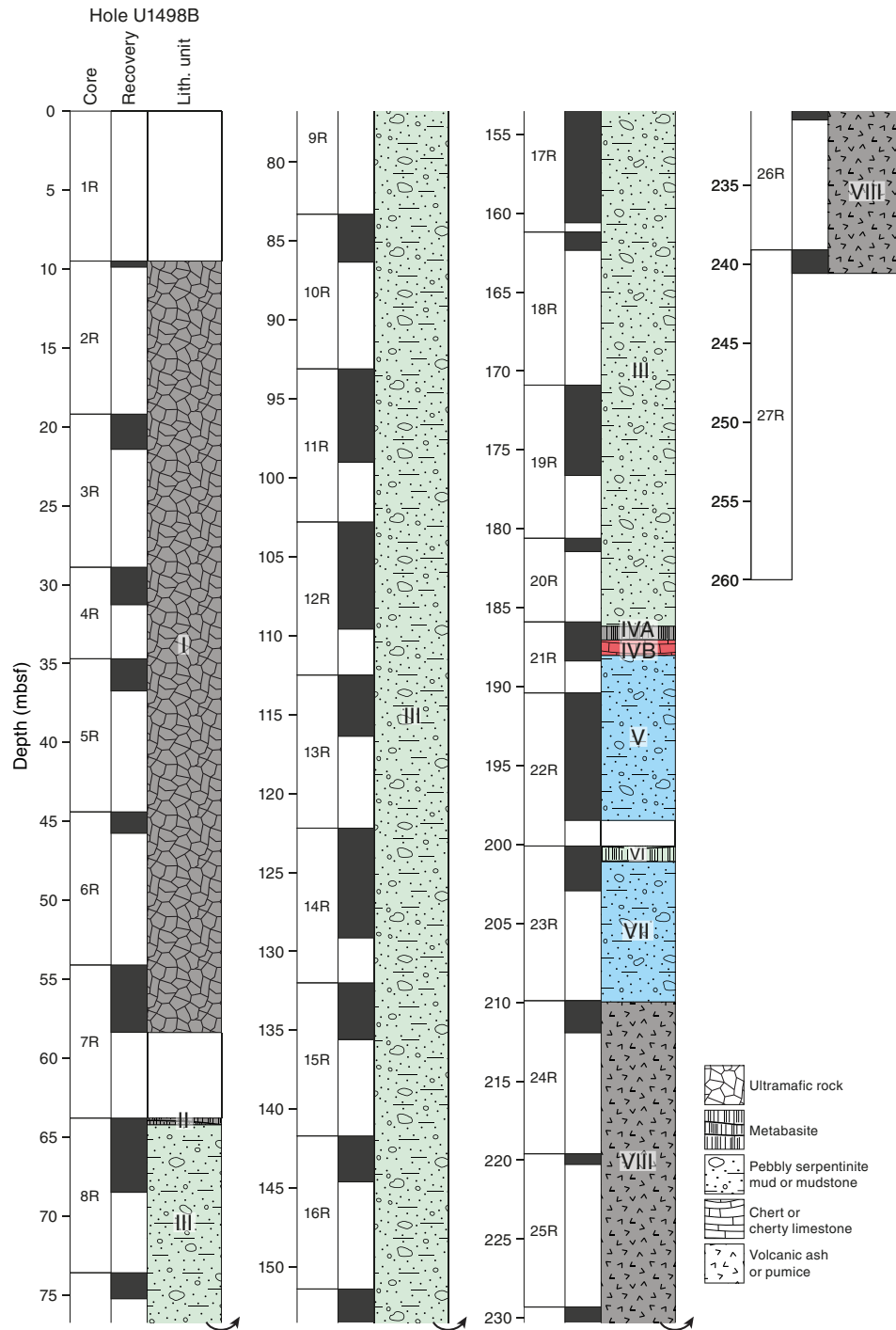
There is a 20 m gap between the bottom of this unit (as recovered) and the underlying Unit VI.

Unit VI

Interval: 366-U1498A-12R-CC, 0 cm, to 19R-CC, 15 cm
Depth: 103.80–172.05 mbsf

Subunit VIA is 68.25 m thick and split into three subunits based on ~7–10 m gaps in the recovered core and differences in color that reflect variations in ash and fossil content.

Figure F5. Lithostratigraphy, Hole U1498B. Colors are according to Figure F5 in the Expedition 366 methods chapter (Fryer et al., 2018a) with slight changes for subunits or when representative for the particular unit.



Subunit VIA

Interval: 366-U1498A-12R-CC, 0 cm, to 14R-CC, 18 cm
 Depth: 103.80–123.38 mbsf

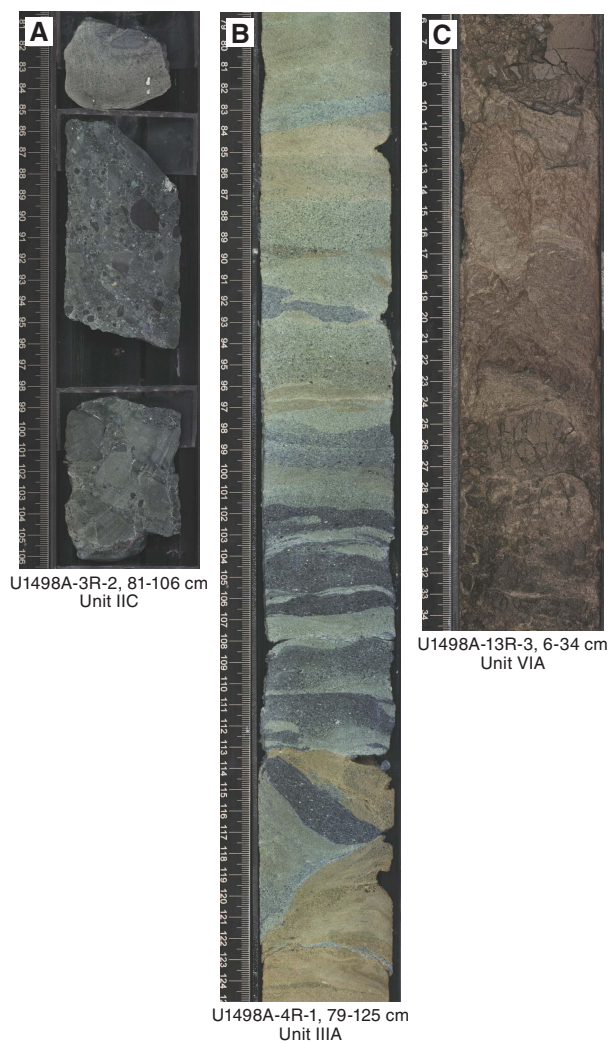
Subunit VIA is 19.58 m thick and consists of nannofossil-rich silt to fine sand with gray sandstone and brown siltstone, all containing a large proportion of volcanic ash (possibly as the dominant component). The subunit contains alternating layers with darker and lighter colors: light brown, black, and dark brown. Black layers

are slightly coarser grained. Contacts are planar to curvilinear and typically sharp or scoured. Bedding is bioturbated in places, with burrows that cross darker/lighter layers. Section 13R-1 (Piece 6, 21–24 cm) is light orange-brown polymict breccia. Section 13R-2, 50–57 cm, is a light tan nannofossil-rich ash layer that is distinct from the layers above and below. Section 13R-3, 25–38 cm, contains a layer with dark brown and light tan material broken up to form intraclasts of one within the other. These intraclasts may not be drilling induced, but the layer seems to be a primary sedimentary

Table T3. Lithostratigraphic units, Hole U1498B. [Download table in CSV format.](#)

Lith. unit	Top depth (mbsf)	Top core, section, interval (cm)	Bottom depth (mbsf)	Bottom core, section, interval (cm)	Unit thickness (m)	Lithology
		366-U1498B-		366-U1498B-		
I	9.50	2R-1, 0	58.38	7R-5, 39	48.88	Ultramafic rock with serpentinite mud
II	63.80	8R-1, 0	64.23	8R-1, 43	0.43	Metavolcanic rock and lithic clasts
III	64.23	8R-2, 0	186.18	21R-1, 28	121.95	Bluish gray serpentinite pebbly mud with lithic clasts
IVA	186.18	21R-1, 28	187.05	21R-1, 115	0.87	Metabasite
IVB	187.05	21R-1, 115	188.03	21R-2, 80	0.98	(Metamorphic) cherty limestone with thin chert layers
V	188.03	21R-2, 80	198.48	22R-CC, 22	10.45	Bluish gray serpentinite pebbly mud with lithic clasts
VI	200.10	23R-1, 0	201.10	23R-1, 100	1	Mafic metavolcanic rock (greenstone)
VII	201.10	23R-1, 100	209.98	24R-1, 8	8.88	Bluish gray serpentinite pebbly mud with lithic clasts
VIII	209.98	24R-1, 8	240.59	27R-CC, 20	30.61	Very dark gray nannofossil-bearing lithified volcanic ash

Figure F6. Major lithologies, Hole U1498A. A. Clasts of mafic metavolcanic rock in microbreccias (Subunit IIC). B. Lenticular bedding in pale green, pale yellowish orange, pale blue, and dark blue serpentinite sand (Subunit IIIA). Drilling disturbance is minimal. C. Nannofossil-rich silty mud and volcanic ash (Subunit IVA).



Subunit VIB

Interval: 366-U1498A-15R-1, 0 cm, to 15R-CC, 8 cm
 Depth: 132.90–134.55 mbsf

Subunit VIB is 1.65 m thick and consists of dark yellow-brown siltstone and sandstone, much of it broken up by drilling disturbance. The sandstone ranges from dark brown coarse grained to brown fine grained. The boundaries between the sandstones and siltstones are sharp and subhorizontal. Ultramafic and mafic rock clasts occur near the top of the subunit, along with small pebbled-sized clasts of lithic breccia, all probably fall-in.

Subunit VIC

Interval: 366-U1498A-16R-1, 0 cm, to 19R-CC, 15 cm
 Depth: 142.70–172.05 mbsf

Subunit VIC is 29.35 m thick and consists of dark greenish gray silty mudstone and nannofossil-rich sand and ash with lithic clasts of sandstone and ultramafic rock. The unit is highly drilling disturbed, with granules of mud, silt, and very fine sandstone, along with ultramafic rock clasts, in a matrix of the same material. There is a great deal of fall-in at the top of each section.

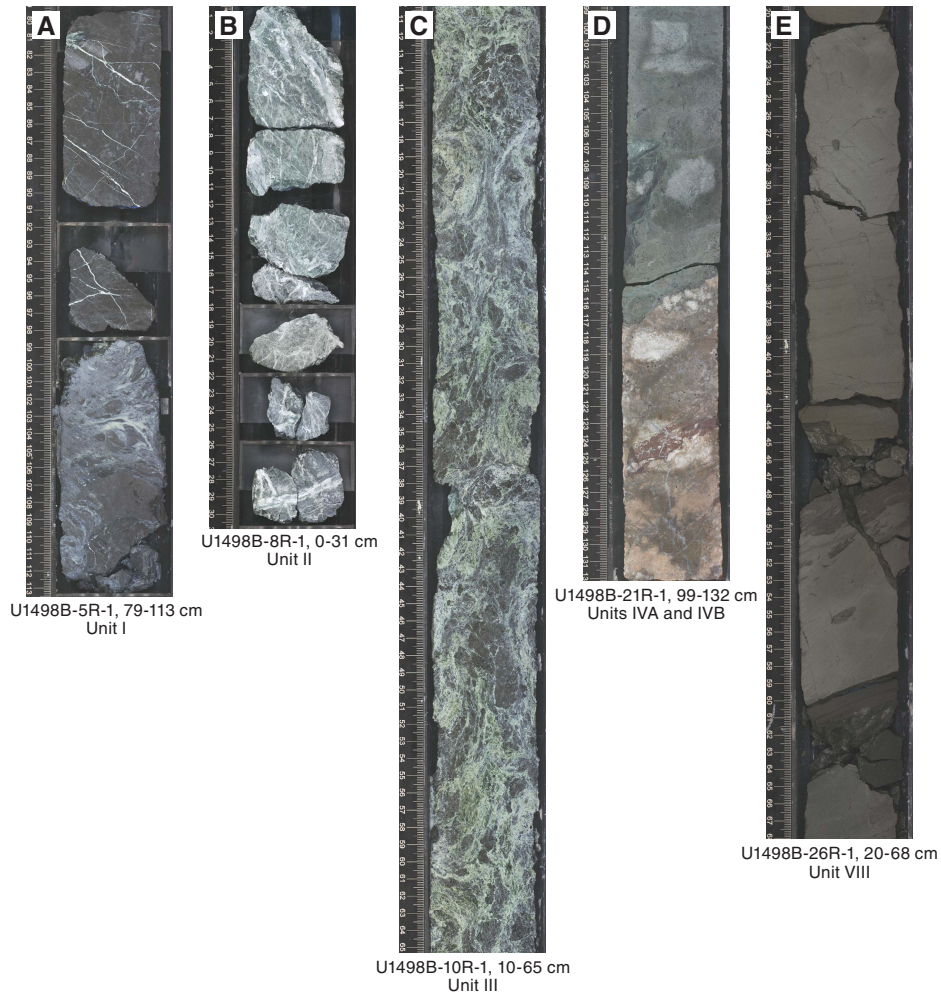
Hole U1498B

Hole U1498B was cored to 260.0 mbsf and recovered 82.82 m of core (31.85% recovery). Hole U1498B cores comprise eight units (Figure F5; Table T3).

Hole U1498B cores differ significantly from those recovered in Hole U1498A. Unit I consists of serpentinite mud with long intervals of mildly to highly serpentinitized ultramafic rock. Unit II is a short interval of extremely altered and carbonate-veined metavolcanic rock, possibly ophicarbonates. Unit III is a long interval of extremely drilling disturbed blue-gray serpentinite mud with plastically deformed completely serpentinitized ultramafic rock clasts with occasional clast-rich zones of coherent ultramafic rock tens of centimeters thick. Unit IV is an interval of gray metavolcanic rock and an adjacent interval of (metamorphic) cherty limestone with thin chert layers. Unit V is bluish gray serpentinite pebbly mud with highly serpentinitized and deformed lithic clasts and is interrupted by Unit VI, a 1 m interval of greenstone metavolcanic rock with a high density of very fine, oriented white veins. Unit VII is again bluish gray serpentinite pebbly mud with highly serpentinitized and deformed lithic clasts. Finally, Unit VIII, bioturbated volcanic ash with nannofossils, occupies the bottommost 30 m of the hole. Examples of several lithologic units in Hole U1498B are shown in Figure F7.

structure. The base of the subunit (Section 14R-CC) consists of dark gray siltstone pieces floating in dark matrix of similar material. This appears to have been a coherent layer broken up by drilling.

Figure F7. Major lithologies, Hole U1498B. A. Serpentinized ultramafic rock cut by bright serpentine veins (Unit I). Original mud matrix lost during rotary coring. B. Mafic metavolcanic rock cut by abundant veins of quartz and calcite (Unit II). C. Variiegated blue-green serpentinite mud with disaggregated clasts (Unit III). D. Large (meter scale) clast consisting of pink cherty limestone (pink; 116–132 cm) in depositional contact with mafic metavolcanic rock (green; 99–116 cm) (Subunit IVA). Cherty limestone is highly deformed by numerous small faults. E. Brown nannofossil-rich volcanic ash (Unit VIII).



Unit I

Interval: 366-U1498B-2R-1, 0 cm, to 7R-5, 39 cm
Depth: 9.50–58.38 mbsf

Unit I is 48.88 m thick and consists of slightly to highly serpentinized ultramafic rock clasts atop serpentinite mud. The uppermost recovery in the hole is from 9.5 mbsf and is reddish brown weathered pebbles of ultramafic rock, probably fall-in material. Section 2R-CC contains 27 cm of dark bluish gray serpentinite mud with rare small (~1 cm) clasts of serpentinized ultramafic rock and a few yellowish fall-in pebbles of altered ultramafic rock.

There was no recovery over the next 10 m, followed by recovery of variably serpentinized ultramafic rock containing white serpentine veins, often with blue serpentine cores. These serpentine veins often crosscut pre-existing black serpentine veins, producing “Frankenstein” veins, suggesting continued volume expansion during progressive serpentinization. In Section 3R-2, the same type of rocks make up the bulk of the recovery, but they are supported in a dark grayish blue serpentinite matrix that contains patches and streaks of white to pale gray. Sections 3R-3 and 3R-4 recovered solely hard serpentinite rock sections (except in Section 4F-1, 47–58

cm, which is dark bluish gray, pebbly serpentinite mud) containing many white veins. Section 4R-CC is mainly the same rock type but is matrix supported by dark bluish gray serpentinite mud with the same streaks and patches of pale gray. In Section 4R-CC, 32–38 cm, matrix support again appears, as it does in Sections 5R-1, 32–38 cm, 5R-1, 99–113 cm, 5R-CC, 0–18 cm, 6R-1, 64–70 cm, and 6R-1, 105–107 cm. In Section 7R-1, 0–11 cm, the core contains partially disaggregated, dark bluish gray serpentinite mud with pale gray streaks and a few very small (<<1 cm) serpentinite clasts. At about 53.4 mbsf (from Section 7R-1, 28 cm, to Section 7R-2, 35 cm) in the long rock interval from which a serpentinite mud matrix was most likely entirely washed away by circulation of mud during coring, an interval of lighter bluish gray serpentinite pebbly mud with patches and streaks of pale gray was recovered. In Section 7R-2, 50 cm was taken as whole rounds. Section 7R-3 recovered 92 cm of drilling-disturbed (sinuous and vertically streaked), serpentinite pebbly mud with mixed dark bluish gray, pale gray, and greenish gray coloring that contains increasingly large clasts of serpentinized ultramafic rock (with pale gray veins) toward the bottom of the interval. Section 7R-4 recovered almost entirely serpentinized ultramafic rock except for light bluish gray serpentinite pebbly mud with patches

and streaks of pale gray at 32–43 cm. The base of the unit contains exclusively serpentinized ultramafic rock in Section 7R-5, 0–38 cm.

Unit II

Interval: 366-U1498B-8R-1, 0 cm, to 8R-1, 43 cm
 Depth: 63.80–64.23 mbsf

Unit II is 0.43 m thick and consists of light greenish gray metavolcanic clasts and/or breccia that are heavily veined with white carbonate and pale gray silica. A clump of green clay-sized mud in Section 8R-1, 34–36.5 cm, may represent the matrix in which these metavolcanic clasts were originally contained. It contains one siltstone clast. Section 8R-1, 0–34 cm, consists of several pieces of the same metavolcanic clast, pale gray-green to gray, cut by abundant veins of carbonate and a white mineral. The veins are 1–2 mm thick, with some composite veins up to 6 mm thick.

Unit III

Interval: 366-U1498B-8R-2, 0 cm, to 21R-1, 28 cm
 Depth: 64.23–186.18 mbsf

Unit III is 121.95 m thick and consists of blue-gray serpentinite pebbly mud with lithic clasts. In about Section 8R-2, 0–27 cm, the serpentinite pebbly mud matrix is dark bluish gray, with a sharp contact with serpentinite mud of a different color and texture. Below Section 8R-2, 27 cm, the dark bluish gray serpentinite mud is swirled with green and blue-green mud by drilling-induced deformation. Black serpentinized ultramafic clasts are typically plastically deformed, but occasional clasts are still rigid. In Section 8R-2, 65–72 cm, the color of the matrix is similar to that seen in Unit II in

Section 8R-1, 34–36.5 cm. Coherent, hard ultramafic clasts occur in Sections 10R-CC, 13R-1, 34–57 cm, 17R-CC, 18R-1, 0–50 cm, 18R-2, 4–28 cm, and 20R-1, 0–34 cm.

Whole rounds in this unit were taken from Sections 8R-3, 88–138 cm, 9R-1, 110–145 cm, 10R-1, 129–149 cm, 10R-2, 0–19 cm, 11R-3, 60–151 cm, 11R-4, 0–68 cm, 12R-5, 42–108 cm, 13R-4, 86–121 cm, 14R-4, 25–140 cm, 14R-5, 101–121 cm, 15R-2, 100–140 cm, 17R-3, 130–152 cm, 17R-4, 32–148 cm, 17R-7, 36–52 cm, 19R-3, 90–150 cm, and 19R-4, 81–101 cm.

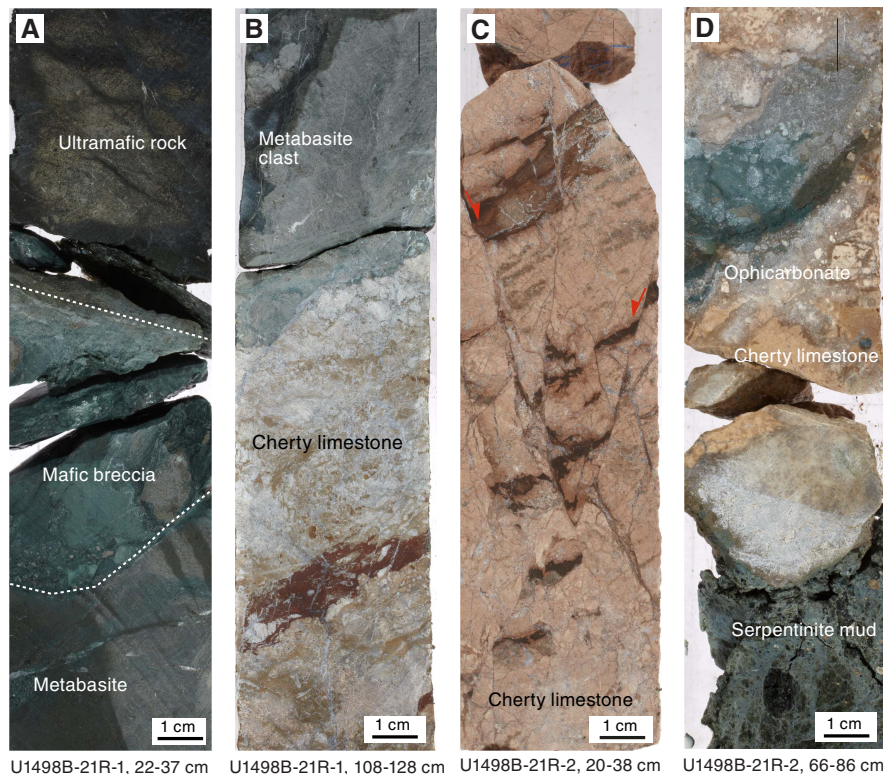
Unit IV

Interval: 366-U1498B-21R-1, 28 cm, to 21R-2, 80 cm
 Depth: 186.18–188.03 mbsf

Unit IV is 1.85 m thick. In general, it consists of greenish gray metabasite and low-grade metamorphic cherty limestone with millimeter- to centimeter-thick chert layers. The contact between the base of Unit III (ultramafic rock) and the top of Unit IV (metabasite) is sheared along a centimeter-thick cataclastic shear zone, comprising a fine-grained ultracataclastic matrix with millimeter- to centimeter-sized subangular to subrounded clasts of ultramafic rock and metabasite. Within Unit IV, the primary contact between the metabasite rock and the cherty limestone is preserved; however, it shows an inverted stratification (Figure F8). The layering and the carbonate/greenstone contact have dip angles of 5° to 30° within the drill hole.

The fine-grained, micritic carbonates are brecciated due to cataclastic deformation, macroscopically representing a protocataclastic cemented by coarse-grained sparitic calcite with a still discernible primary sedimentary layering, subsequently sheared

Figure F8. Contacts between ultramafic rock, mafic rock, metamorphic cherty limestone, ophicarbonates, and serpentinite mud (Core 366-U1498B-21R). A. Sheared contact between ultramafic rock and metabasite (21R-1, 22–37 cm). B. Primary contact between metabasite and cherty limestone (21R-1, 108–128 cm). C. Brecciated cherty limestone (21R-2, 20–38 cm). D. Ophicarbonates on the basal contact of cherty limestone and serpentinite mud (21R-2, 66–86 cm).



along conjugate high-angle normal faults with dip angles between 70° and 80° within the drill hole. Coarse-grained sparitic carbonate was precipitated within veins and gashes. Precipitation of carbonate from mobilized fluids was also observed along the bottom contact of the carbonates toward serpentinite mud, forming a reaction seam with ophicarbonates.

The Subunit IVA/IVB boundary is marked by the metabasite/limestone contact.

Subunit IVA

Interval: 366-U1498B-21R-1, 28 cm, to 21R-1, 115 cm

Depth: 186.18–187.05 mbsf

Subunit IVA is 0.87 m thick and consists of light greenish gray metabasite rock clasts that are locally brecciated at the contact with the overlying unit and at internal discontinuities. The metabasite also contains numerous lighter gray hair-like veins.

Subunit IVB

Interval: 366-U1498B-21R-1, 115 cm, to 21R-2, 80 cm

Depth: 187.05–188.03 mbsf

Subunit IVB is 0.98 m thick and consists of pinkish gray cherty limestone with sparitic carbonate gashes, carbonate veins, millimeter- to centimeter-thick chert laminae, stylolitic layer boundaries, and faulted and brecciated layers (millimeter to centimeter angular clasts) with high-angle normal faults. The contact with the next unit appears to be ophicarbonates.

Unit V

Interval: 366-U1498B-21R-2, 80 cm, to 22R-CC, 22 cm

Depth: 188.03–198.48 mbsf

Unit V is 10.45 m thick and consists of bluish gray to light green serpentinite pebbly mud with lithic rock clasts. The mud has experienced severe drilling disturbance; green and blue serpentinite mud and dark gray rock clasts are all elongated, brecciated, and mixed together. In Section 22R-5, 128–135 cm, the recovered material is split vertically, and about half of it (the left half, as seen in the archive core photo) is lighter greenish gray serpentinite pebbly mud. The same type of matrix is at the top of the next section (22R-6, 0–22 cm), but the rest of the section (22R-6, 22–53 cm) was taken as whole rounds. The core catcher (Section 22R-CC) consists of medium greenish gray serpentinite pebbly mud.

Unit VI

Interval: 366-U1498B-23R-1, 0 cm, to 23R-1, 100 cm

Depth: 200.10–201.10 mbsf

Unit VI is 1.00 m thick and consists of green metavolcanic rock with pervasive oriented thin (millimeter to centimeter) white veins of carbonate and silicate minerals. White amygdules are also observed in some mafic clasts. Section 23R-1, 0–12 and 82–100 cm, consists of light greenish gray serpentinite pebbly mud with numerous clasts of both metavolcanic rock and white streaks, as well as a patch (Section 23R-1, 91–96 cm) of soft slightly soupy pale greenish gray mud.

Unit VII

Interval: 366-U1498B-23R-1, 100 cm, to 24R-1, 8 cm

Depth: 201.10–209.98 mbsf

Unit VII is 8.88 m thick and consists of bluish gray serpentinite pebbly mud with lithic clasts. Dark blue and greenish serpentinite mud and dark gray, plastically deformed serpentinitized ultramafic rocks are mingled together due to drilling disturbance. A moderately serpentinitized solid ultramafic rock clast fills the core in Sections 23R-3, 0–33 cm, and 24R-1, 0–8 cm.

Unit VIII

Interval: 366-U1498B-24R-1, 8 cm, to 27R-CC, 20 cm

Depth: 209.98–240.59 mbsf

Unit VIII is 30.61 m thick and consists of very dark gray nanofossil-bearing lithified volcanic ash with zones containing fine lamination, lapillistones, small-scale faults, and bioturbation. Zones of bluish black serpentinite gravel from fall-in are observed in Sections 25R-1, 0–13 cm, and 27R-1, 0–13 cm.

A whole round was taken from Section 24R-2, 36–52 cm.

Petrology

Lithic material from Site U1498 includes serpentinite mudflows with a range of lithic clasts and ash-rich pelagic sediments from beneath the mud volcano edifice; Hole U1498A also has a thin coating of recent pelagic sediment covering the mudflows. Hard rock clasts recovered from Site U1498 are dominantly dark gray serpentinitized ultramafic rocks. Basaltic metavolcanic rocks and sedimentary rocks including limestone, cherty limestone, sandstone, mudstone, and shale occur episodically.

There are three types of sediment at Site U1498. Pelagic sediment is found only in Hole U1498A. Serpentinite mud underlies the pelagic sediment in Hole U1498A and forms the upper sediment in Hole U1498B. In both holes, the serpentinite mudflows are underlain by a volcanic ash layer, which is typically lithified. In Hole U1498A, pelagic sediments are siliceous ooze or siliceous calcareous ooze in Unit I and clay in Subunit VIB. The mineralogy of serpentinite mud from Holes U1498A and U1498B is similar. Serpentine is dominant, and chlorite, brucite, spinel, garnet, and Fe oxide are the common accessory minerals. However, the serpentinite mud and sand from Hole U1498A is much coarser and more colorful than the serpentinite mud from Hole U1498B (primarily light greenish and bluish gray serpentinite mud). Carbonate species in the two holes are also different; aragonite is common in Hole U1498A, whereas calcite is common in Hole U1498B. Tremolite is found in Unit VII of Hole U1498B at the bottom of the serpentinite mud. Volcanic ashes recovered in the bottom of these two holes are very similar, composed of dominant clear glass with abundant disoclasts and coccoliths.

Sediment and mudflow matrix

Based on lithology changes, 25 samples from Hole U1498A (Figure F9) and 21 samples from Hole U1498B (Figure F10) were selected for smear slides.

Hole U1498A

The top of Hole U1498A (Sample 1R-1, 18 cm) is siliceous ooze with dominant microfossils (~70%), clay matrix (up to ~20%), and minor volcanoclastic fragments (~10%) (Figure F11). Microfossils include abundant radiolarians and diatoms, minor sponge spicules, and trace silicoflagellates and foraminifers. Most of the volcanoclasts are possibly fragments of basalt or dolerite, as inferred from the phenocrysts. Fragments of pyroxene and feldspar are also common.

Figure F9. Downhole changes in mud composition, Hole U1498A. D = dominant (>50%), A = abundant (20%–50%), C = common (10%–20%), R = rare (1%–10%), Tr = trace (<1%).

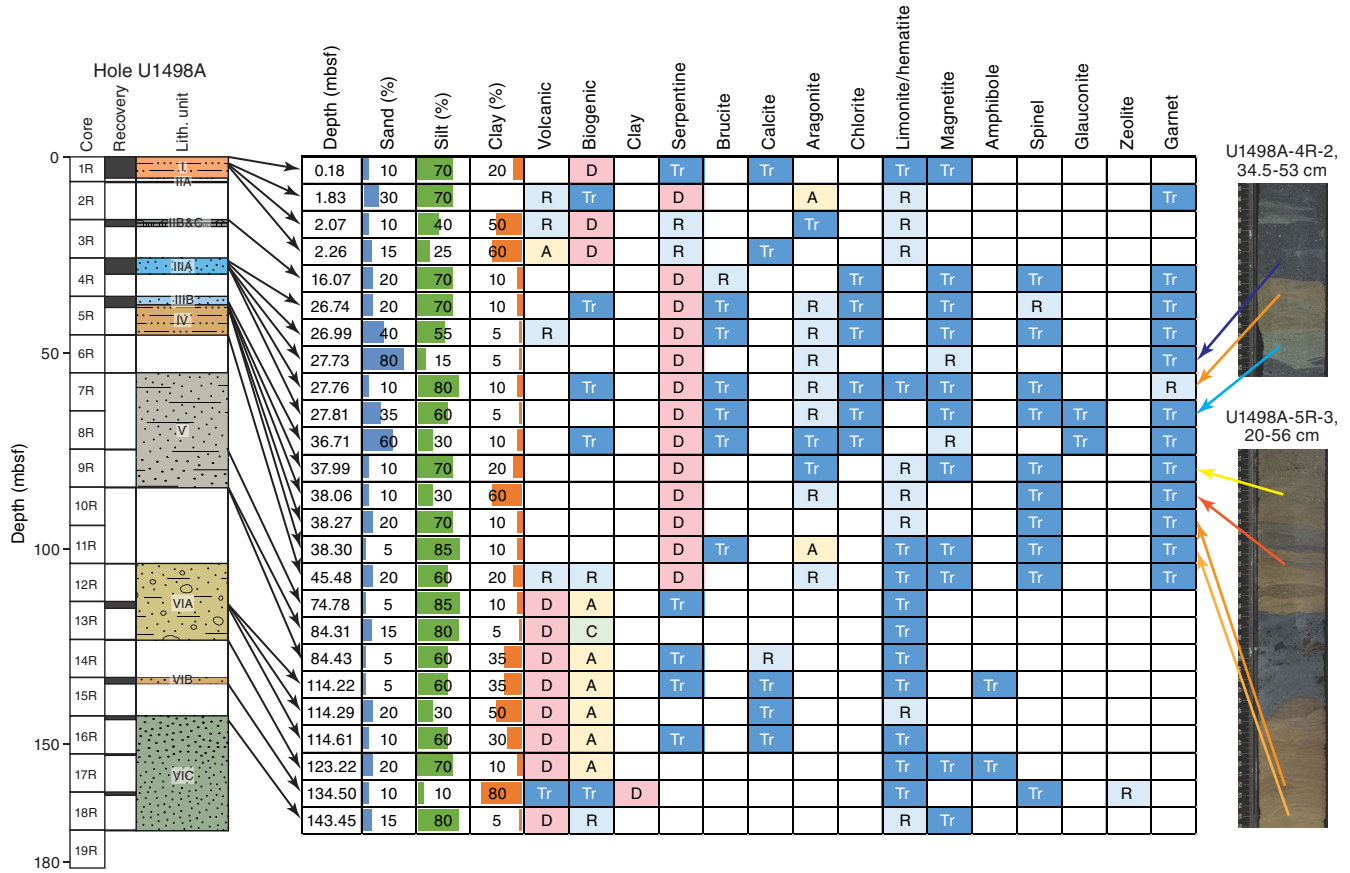


Figure F10. Downhole changes in mud composition, Hole U1498B. D = dominant (>50%), A = abundant (20%–50%), C = common (10%–20%), R = rare (1%–10%), Tr = trace (<1%). The sample at 200.21 mbsf is scratched from a green metabasite.

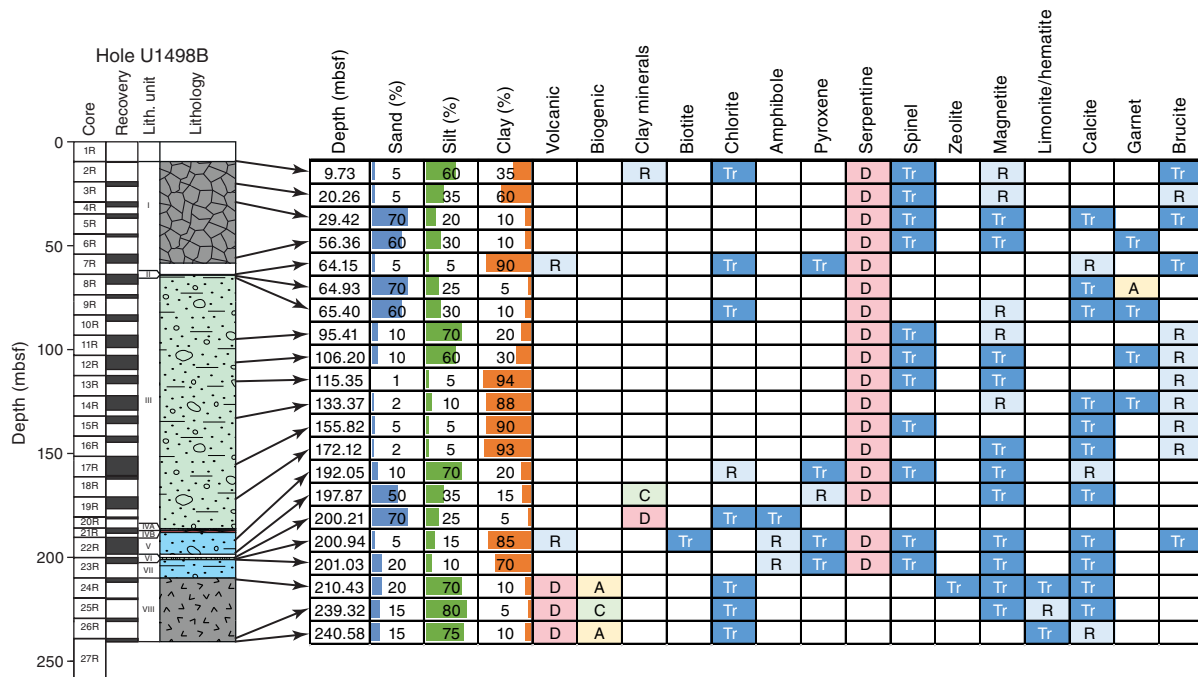


Figure F11. Pelagic sediment and embedded serpentinite mud in Unit I, Hole U1498A. A, B. Siliceous microfossils, pumice (Pum) fragments, and volcanic crystal fragments (1R-1, 18 cm) Rad = radiolarian, Spg spc = sponge spicule. C, D. Embedded serpentine (Srp) with partly oxidized serpentine, acicular aragonite (Arg) crystals, and a radiolarian (1R-2, 33 cm). Glt = glauconite. E, F. Calcareous microfossils, a discoaster, and volcaniclastic fragments including feldspar and small crystal fragments (1R-2, 57 cm). Foram = foraminifer, Pl = plagioclase, Ptp = pteropod, Dsc = discoaster.

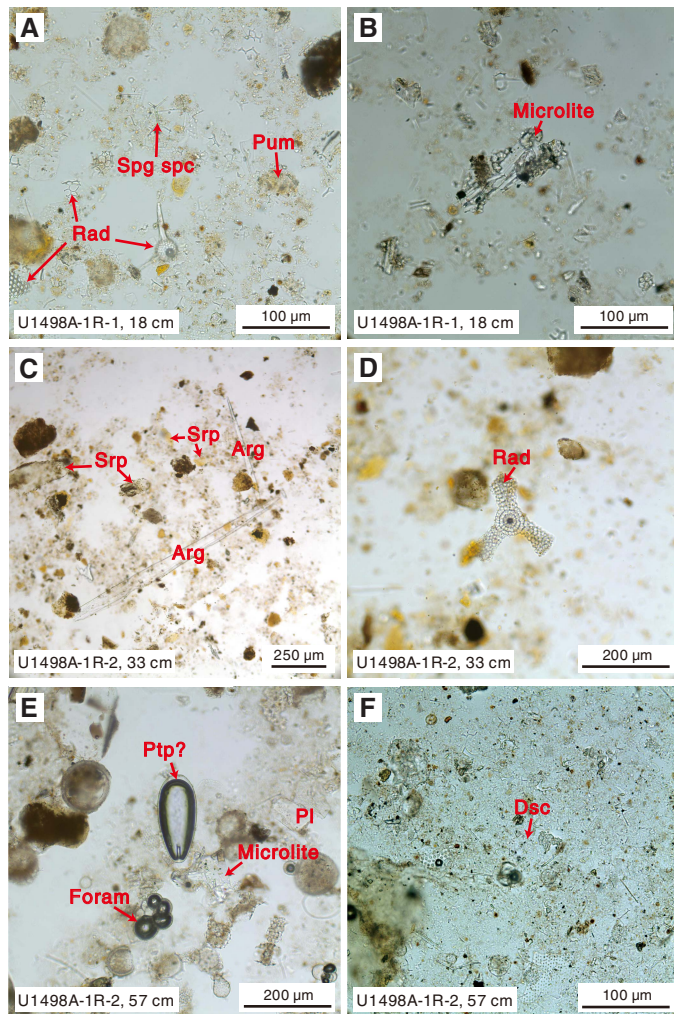
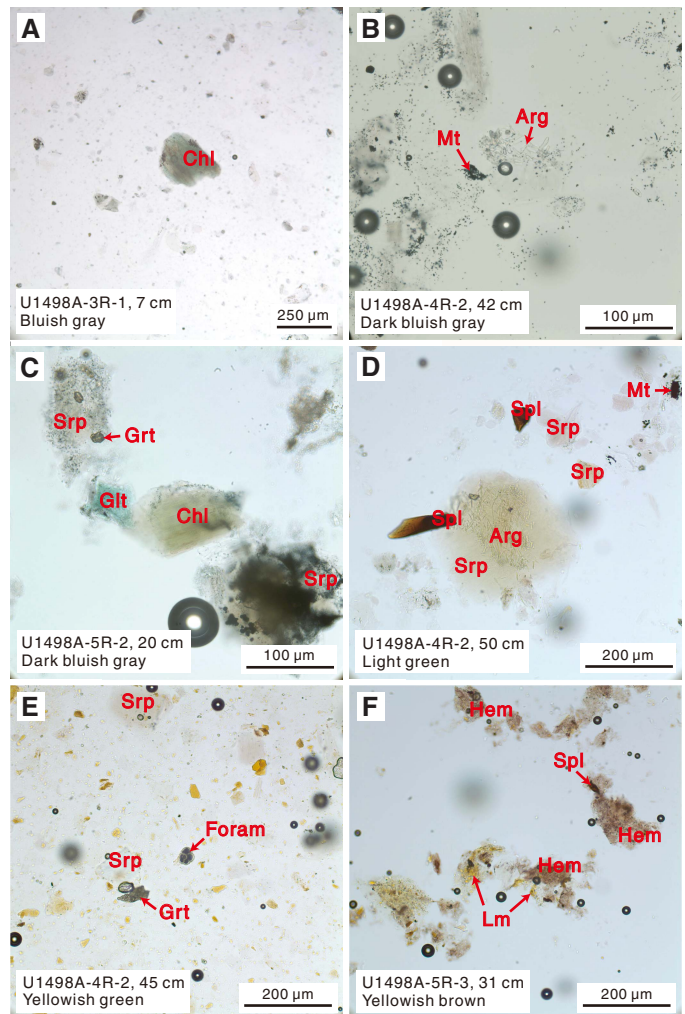


Figure F12. Serpentinite mud in Units II-IV, Hole U1498A. A. Chlorite (Chl) grain (3R-1, 7 cm). B. Aragonite (Arg) crystals and minute magnetite (Mt) in matrix (4R-2, 42 cm). C. Garnet (Grt) and chlorite (5R-2, 20 cm). Srp = serpentine. D. Aragonite inclusion in clear serpentine grain (4R-2, 50 cm). Magnetite, glauconite (Glc), and spinel (Spl) are also shown. E. Foraminifer (Foram) in serpentinite mud (4R-2, 45 cm). Most serpentine grains are yellowish in color due of oxidization. F. Limonite (Lm) and hematite (Hem) grains in oxidized layer (5R-3, 31 cm).



Trace colorless to brown glass, magnetite, limonite, serpentine, and carbonate grains were also observed. The thin lenses of yellowish brown oxidized serpentinite sand-silt (Sample 1R-2, 33 cm) in this layer are composed of dominant colorless to yellowish serpentine with abundant sand- to clay-sized acicular aragonite (~20%). The yellowish serpentine is probably rich in limonite due to oxidization. Trace garnet grains, pyroxene and feldspar fragments, and radiolarians were also observed. Distinct to the siliceous ooze at the top of this hole, the pelagic sediments beneath the oxidized serpentinite mud are siliceous calcareous ooze composed of dominant calcareous fossils, abundant siliceous microfossils, and minor volcanic clasts, including pumice, small crystals, pyroxene, and feldspar. Calcareous fossils include abundant nannofossils (~45%; mostly coccoliths), minor foraminifers (~20%), and some calcisphere (~5%) and trace ceratoliths (U-shape). A 0.1 mm long ellipse-shaped microfossil with a calcareous shell was observed (pteropod?). A few dis-

coasters, which have been extinct for about 2 My, are in Samples 1R-2, 57 cm, and 1R-2, 76 cm. Siliceous microfossils include abundant radiolarians, minor sponge spicules, diatoms, and trace silicoflagellates. Rare serpentine, hematite, and trace carbonate were also observed.

The bluish gray serpentinite mud (Sample 3R-1, 7 cm) from Unit II is composed of dominant sandy to silty colorless to dusty serpentine (~98%), minor sand-sized brucite (~1%), trace spinel, and magnetite and chlorite (Figure F12).

The colorful serpentinite mud in Units III and IV mainly includes three colors: dark bluish gray, light green, and yellowish green to yellowish brown. The dark bluish gray serpentinite mud is composed of dominant sand- to silt-sized dusty serpentine (~92–96%) filled with minute magnetite grains (~2–5%) and minor acicular or aggregates of aragonite (trace to ~2%). Trace brucite, garnet, glauconite, and chlorite were also observed. Small acicular arago-

nite, euhedral garnet, and subhedral magnetite grains are sometimes included inside of serpentine grains. Fragments of foraminifers were occasionally observed.

The light green serpentinite mud is composed of dominant sandy to silty clear serpentine (~96%–97%), minor acicular-radial aragonite or aggregate (~1%–2%), sand- to silt-sized chromium spinel (trace to 1%), and trace brucite, chlorite, garnet, and magnetite. Euhedral garnet and magnetite and acicular aragonite are sometimes included inside of serpentine grains. Fragments of foraminifers were occasionally observed.

The yellowish green to yellowish brown serpentinite mud is composed of dominant sand- to silt-sized colorless to yellowish serpentine (~94%–98%) with minor acicular aragonite (as much as 5%). The yellowish serpentine is probably rich in limonite due to oxidization. Limonite is also developed on the surface or inside of serpentine, which could be oxidized from magnetite. Trace chlorite, magnetite, brucite, garnet, and spinel are also found as accessory minerals. Some sand- to silt-sized aragonite laths and minute grains of carbonate in the matrix were occasionally observed. Trace volcaniclastic materials including glass, small crystals, some pyroxene fragments, foraminifers, and coccoliths were also observed in this layer. Hematite and limonite are both common in the yellowish brown serpentinite mud of Unit IV (Sample 5R-3, 31 cm).

Gray to brown silt- to sand-sized volcanic ash (~70%) that generally contains abundant clay-sized calcareous nannofossils and trace fragments of siliceous microfossils is found at the bottom of this hole (Figure F13). Volcanic grains consist of dominant clear glass (~68%–69%), minor (1%) to trace pumice, small crystal grains, and trace fragments of pyroxene, feldspar, and amphibole. Calcareous nannofossils in this layer include abundant discoasters and trace coccoliths. Siliceous microfossils include radiolarians and some

sponge spicules. Small grains of calcite (trace to 1%) are also present in the mud matrix. Radiolarians are the dominant microfossils in Sample 9R-CC, 18 cm, in which no calcareous fossils are observed. Trace serpentine and limonite grains were also observed. A dark brown ash lens (Sample 13R-2, 59 cm) embedded in this layer is a bit different in composition and contains abundant small crystal fragments. A mud sample composed of dominant clay with rare volcanic clasts and trace siliceous microfossils including radiolarians and sponge spicules was observed in Sample 15R-CC, 3 cm.

Hole U1498B

Pelagic sediment was not recovered in Hole U1498B, and serpentine dominates the muds in Units I–VII. Because of drilling disturbance, serpentinite mud from different units appears similar, with a thin, dark bluish and green curved layer along the core. In general, this serpentinite mud consists of dominant serpentine with sandy-clayey sized minor brucite, chlorite, magnetite, spinel, garnet, and calcite as common accessories (Figure F14). The bluish gray serpentinite mud often contains dusty serpentine filled with minute magnetite grains (~2%–4%), and the light green serpentinite

Figure F13. Volcanic ash layers, Holes U1498A and U1498B. A. Clear glass, feldspar (Fsp) fragment, sponge spicule (Spg spc), and discoasters (Dsc) (366-U1498A-13R-2, 52 cm). B. Coccoliths (C) and discoasters (13R-3, 14 cm; cross-polarized light [XPL]). C. Foraminifer (Foram) and clear glass (366-U1498B-24R-1, 53 cm). D. Discoasters and clear glass (27R-1, 22 cm).

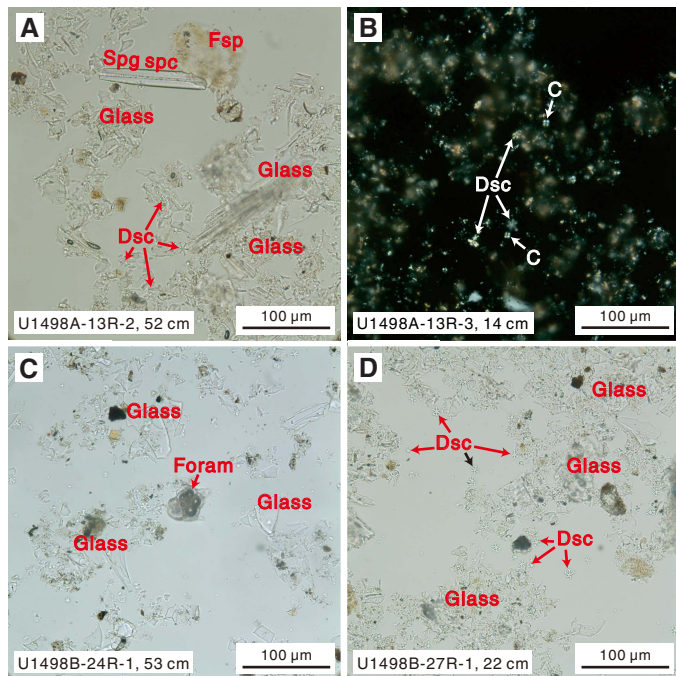
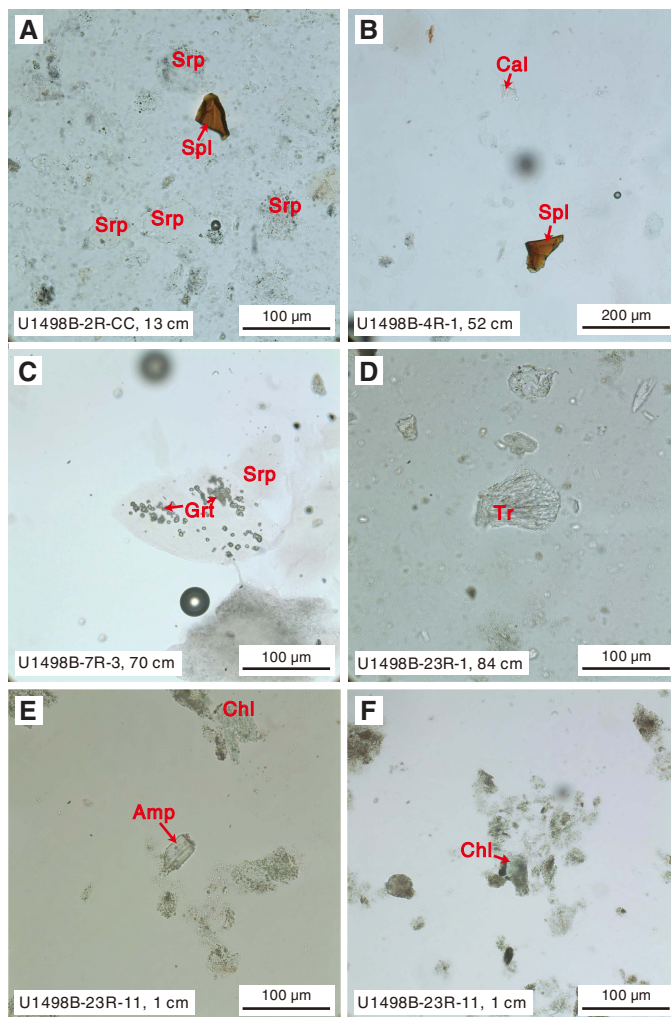


Figure F14. Serpentinite mud and metabasite, Hole U1498B. A. Spinel (Spl) in a dusty serpentine (Srp) matrix (2R-CC, 13 cm). B. Spinel and colorless calcite (Cal) grains (4R-1, 52 cm). C. Tiny garnet (Grt) grains in a clear serpentine flake (7R-3, 70 cm). D. Radial tremolite (Tr) fibers (23R-1, 84 cm). E, F. Metabasite with amphibole (Amp) and chlorite (Chl) flakes (23R-1, 11 cm).



mud always contains clear serpentine flakes. The small garnet grains are sometimes developed inside of serpentine grains. Some white-green mud contains abundant colorless sand- to clay-sized anhedral granular or aggregates of garnet (20% in Sample 8R-2, 70 cm). Minor tremolite fibers or laths (up to 5% in Sample 23R-1, 95 cm) were observed at the bottom of serpentinite mud section (Unit VII) beneath the metabasite.

Powder scratched from the metabasite in Unit VI is composed of 99% sand- to silt-sized grains of an unidentified clay-rich dusty mineral. However, some greenish chlorite grains with green to brown pleochroism and trace amphibole were also observed.

Dark gray ash at the bottom of this hole is similar to that found in Hole U1498A and is composed of silty volcanic ash with calcareous nannofossils (Figure F13). Volcanic ash consists of dominant clear glass (~60%–68%), small crystal fragments (~10%–15%), pumice (~4%–5%), brownish glass (~1%–5%), and trace pyroxene (orthopyroxene and clinopyroxene) and feldspar fragments. Calcareous nannofossils (~15%–25%) in this layer are dominantly discoasters and minor coccoliths. Fragments of foraminifers, radiolarians, and sponge spicules were found, as well as trace chlorite, magnetite, Fe oxide, and calcite.

Ultramafic rocks

Ultramafic rocks include harzburgite and dunite. All are serpentinized to some degree, and many are totally serpentinized. Most serpentinization is pseudomorphic, which allows the primary modal mineralogy to be estimated and primary textures to be inferred even when serpentinization is complete. Other samples, however, have an interpenetrating serpentine fabric that destroyed all primary textural information.

Serpentinite

A few samples are totally serpentinized, with an interpenetrating serpentine fabric that destroyed all primary textural information. These samples may contain antigorite, but this composition must be confirmed by Raman or X-ray diffraction (XRD) analyses.

Sample 366-U1498A-2R-CC, 20–22 cm (TS 115), is completely serpentinized peridotite that contains both pseudomorphic and nonpseudomorphic serpentine. A few bastite pseudomorphs can be recognized, as well as mesh-texture pseudomorphs of olivine. Much of the section, however, contains blue-gray nonpseudomorphic serpentine. The color is very unusual for serpentine and may be related to the blue serpentinite mud.

Sample 3R-2, 126–128 cm (TS 122), consists of serpentinite with an interpenetrating texture. There are a few bastite pseudomorphs and trace amounts of chrome spinel, but otherwise the sample is totally nonpseudomorphically altered.

Harzburgite

Harzburgites vary from relatively unaltered to totally serpentinized but with recognizable textures that can be used to infer primary mineralogy. Some still preserve their primary textures, especially in pyroxene and spinel, allowing inferences about their original modal compositions. Remarkably, many of the thoroughly serpentinized harzburgites retain relict olivine, orthopyroxene, and clinopyroxene, as well as chrome spinel.

Sample 366-U1498A-3R-2, 9–12 cm (TS 116), is partially serpentinized harzburgite (about 70% serpentinization) with pseudomorphic mesh and bastite serpentine textures. Relict unaltered olivine, orthopyroxene, and clinopyroxene were observed. Olivine grains show undulatory extinction, and their grain sizes are medium

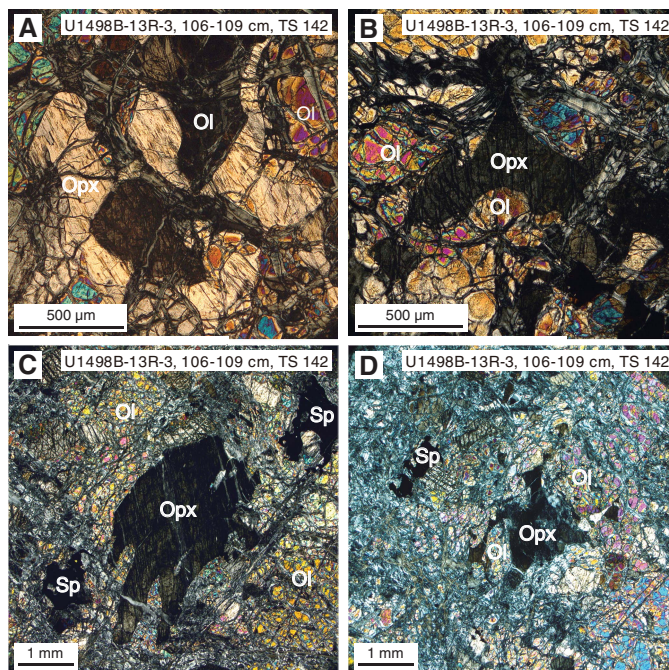
(a few hundred micrometers) with polygonal shapes, indicating that they were deformed in the lithospheric mantle.

Samples 366-U1498A-3R-3, 10–12 cm (TS 123), and 366-U1498B-7R-4, 120–123 cm (TS 136), are partly serpentinized harzburgite with about 80% serpentinization. Relict olivine and orthopyroxene are similarly medium to coarse grained with protogranular texture. Orthopyroxene often has lobate and irregular boundaries with surrounding olivine grains, suggesting dissolution of orthopyroxene and replacement by olivine during melt-mantle interaction (reactive porous flow melt infiltration) (Figure F15). Some small orthopyroxenes are interstitial to olivine grains. Clinopyroxene only occurs as an interstitial phase. Reddish brown spinel about 0.4 mm in size often occurs in association with orthopyroxene and has a holly leaf texture.

Sample 366-U1498B-3R-3, 56–59 cm (TS 127), is serpentinized harzburgite. Serpentinization is nearly complete (about 98%), but relict spinel, orthopyroxene, and clinopyroxene are preserved and associated in spinel–pyroxene clusters. Olivine is mostly replaced by pseudomorphic serpentine. Orthopyroxene is preserved in the center of pseudomorphic bastite. Brownish veins of fibrous serpentine with perhaps chlorite crosscut the rock.

Sample 3R-3, 95–98 cm (TS 128), contains two domains: (1) moderately serpentinized (~40%) harzburgite crosscut by serpentine veins and (2) completely serpentinized harzburgite. Domain 1 consists of 75% olivine, 24% orthopyroxene, 1% clinopyroxene, and trace amounts of spinel. It has a protogranular texture with olivine and orthopyroxene grains around 2–4 mm long.

Figure F15. Reactive diffuse porous flow textures in harzburgite (366-U1498B-13R-3, 106–109 cm; TS 142; XPL). A. Orthopyroxene (Opx; tan) filling in between and enclosing olivine (Ol). B. Orthopyroxene in center of view at extinction, filling in between olivine grains. Lobate margins against olivine, and cusps point into olivine grain boundaries. C. Orthopyroxene grain at extinction (black) with ragged margins. SP = spinel. D. Orthopyroxene grain at extinction (black) with ragged grain boundaries, extreme interstitial textures, and disconnected fragments that are optically continuous with the main body.



A 0.3 mm clinopyroxene is interstitial to orthopyroxene grain boundaries. Amoeboid chromian spinels occur in association with orthopyroxene. Olivine and orthopyroxene are partly altered to mesh and bastite serpentine, respectively. Domain 2 appears to have the same protolith as Domain 1.

Sample 13R-3, 106–109 cm (TS 142), is relatively fresh harzburgite (50% serpentinized) with coarse equigranular texture and porous flow melt reaction textures. Olivines are very coarse, with a 1.5:1 to 2.5:1 aspect ratio and grains 4–6 mm in size. Orthopyroxenes are resistant to serpentinization and are ragged with cusps pointing into olivine at small apical angles in poikilitic-like crystals. Textures resemble porous flow melt reaction textures but with fresh olivine and pyroxene. Clinopyroxenes form small anhedral grains associated with orthopyroxene. The serpentine crystallized as veins with pseudomorphic textures. The rock is cut by many fibrous veins with a brown birefringence, possibly serpentine + chlorite.

Sample 18R-1, 11–14 cm (TS 143), is serpentinized harzburgite (about 70% serpentinization). The olivine is crosscut by serpentine veins with pseudomorphic textures, whereas the orthopyroxene is relatively resistant to the serpentinization process. The serpentine is locally blue or brown. Porous flow reactive melt texture was observed, with lobate interstitial ragged orthopyroxene.

Sample 20R-1, 17–19 cm (TS 144), is serpentinized harzburgite (about 60% serpentinization) composed of 80% olivine, 19% orthopyroxene, and 1% spinel. Olivine and orthopyroxene are coarse grained and similar in size, with a protogranular texture. Grain boundaries are lobate and irregular. Most orthopyroxenes are embayed by olivine. Some olivines are nearly euhedral and intergrown with orthopyroxene, possibly replacing orthopyroxene due to melt reaction. Spinel commonly occur associated with orthopyroxene. The mantle minerals are crosscut by several generations of serpentine veins with mostly pseudomorphic textures (some fibrous serpentine with a brown/blue birefringence were also observed, possibly serpentine + chlorite). The orthopyroxene is little affected by the serpentinization and shows possible porous flow reaction textures.

Mafic igneous rocks

Mafic igneous rocks occur in both Holes U1498A and U1498B. They are typically metamorphosed at relatively low temperatures, producing clays, chlorite, and serpentine (in olivine-bearing basalts). Blue saponite vesicle fillings are found in some samples, whereas others have a green clay filling, possibly celadonite. Primary igneous textures are preserved, including volcanic glass in some samples. In other samples, the fine-grained mesostasis phases are altered.

Basalt

Basalt commonly occurs as small fragments at other Expedition 366 sites, but at Site U1498, it occurs as relatively large clasts, as long as 1 m. Sample 366-U1498A-3R-2, 80–82 cm (TS 118), is fine-grained, aphyric metabasalt with an intergranular texture (Figure F16). Plagioclase and the mesostasis are altered, but relict augite is preserved throughout. This clast contains an inner zone of relatively unaltered basalt, but its outer rim is highly altered and most phases are unrecognizable. Nonetheless, some relict augite remains in the rim, despite the high degree of alteration. This alteration must have occurred at a relatively low temperature, however, because macroscopically observed vesicles contain blue clay (saponite); this clay would not survive even low-grade metamorphism (i.e., zeolite facies). Clinopyroxenes from this sample were analyzed by electron

microprobe and are normally zoned low-Ti augites with compositions consistent with formation in tholeiitic mid-ocean-ridge basalts.

Volcanic microbreccia

Volcanic clasts are the dominant component of the microbreccias in Core 366-U1498A-3R, with black serpentinized ultramafic clasts as a minor component. The microbreccia matrix consists of very fine grained detritus derived from the volcanic clasts, which may have been glassy originally; this composition implies little or no metamorphic overprint. The volcanic clasts appear to include both basalt and boninite; the latter inference is based on crystals of what appears to be enstatite growing in some of the glass blebs.

Samples 3R-2, 113–117 cm (TS 124), 3R-2, 121–122 cm (TS 121), 3R-2, 103–105 cm (TS 120), and 3R-2, 94–96 cm (TS 119), are all matrix-supported microbreccias consisting of volcanic clasts as large as 1 cm in diameter in very fine grained (glassy) matrix with small (≤ 1.2 mm) rounded serpentine clasts. Some of the clasts are fine-grained aphyric basalt with an intergranular texture. Plagioclase and the mesostasis are altered, but most augite is fresh and may have finely crystalline rims of chlorite that outline the grains.

Other fragments are highly vesicular, with vesicles filled by a bright green mineral, possibly celadonite (Figure F17). They formed originally as hyaloclastite deposits. One rounded clast consists of pale tan glass (no vesicles) with acicular prisms of subcalcic clinopyroxene. Electron microprobe analyses of the glass bleb and the

Figure F16. Fine-grained aphyric basalt with intergranular texture and elongate plagioclase and interstitial clinopyroxene (Cpx) (366-U1498A-3R-2, 80–82 cm; TS 118; XPL).

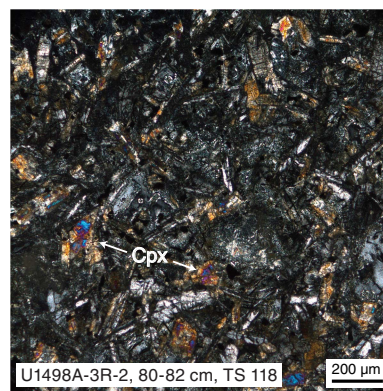
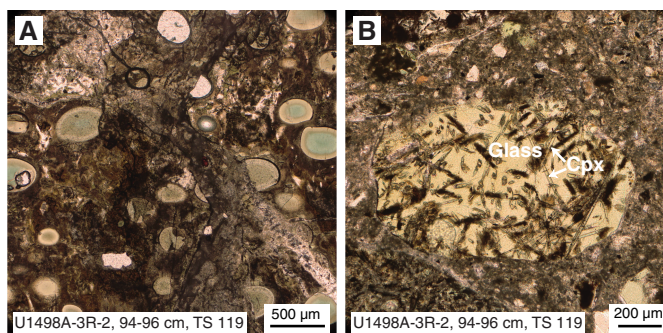


Figure F17. Microbreccia (366-U1498A-3R-2, 94–96 cm; TS 119; plane-polarized light). A. Vesicles filled by bright green minerals in microbreccia matrix. B. Elliptical pale green glass bleb with prismatic clinopyroxene (Cpx) crystals.



acicular prisms reveal unusual compositions. The pyroxenes are low-Ca, high-Fe clinopyroxenes. The glass totals consistently average about 90 wt%. The analyzed glass bleb is clear and shows no signs of secondary alteration, and the low totals may be primary, suggesting strongly hydrous compositions originating from a highly hydrous melt. Glass compositions have up to 3–5 wt% K₂O, 0.5–0.8 wt% Na₂O, 0.2–0.3 wt% CaO, 12–16 wt% MgO, 8–15 wt% Al₂O₃, and 48–51 wt% SiO₂. The provenance of this clast of the microbreccia is uncertain at this stage.

Mafic metavolcanic rocks

Mafic metavolcanic rocks are found prominently in Hole U1498B. Core 21R contains a >1 m long clast of metabasalt or meta-dolerite that is in fault contact with ultramafic rock at one end and in depositional contact with metamorphosed cherty limestone at the other. Core 23R contains another >1 m long clast of greenstone (metabasalt) cut by abundant quartz veins. Both are metamorphosed under prehnite-pumpellyite or low greenschist conditions and brittlely deformed.

Sample 21R-1, 56–58 cm (TS 145), is microcrystalline aphyric basalt in contact with tectonic(?) breccia. The basalt consists mainly of 50 µm acicular or elongate plagioclase and interstitial clinopyroxene with an intergranular texture. Some interstices between plagioclases are also filled with microcrystalline secondary minerals. The tectonic breccia is composed of cryptocrystalline matrix and brecciated volcanic clasts that appear to have the same original lithology as the adjacent aphyric basalt. The clasts are severely altered, and the mafic minerals are chloritized but still preserve some relict clinopyroxenes.

(Meta-)sedimentary rocks

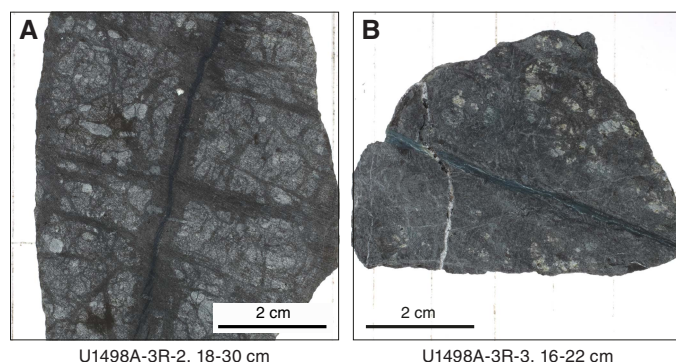
Sample 366-U1498B-21R-2, 38–40 cm (TS 146), is carbonated chert breccia. The rock is composed of interstitial calcite forming an irregular vein network with blocky calcite associated with trace amounts of muscovite and quartz. The calcite envelops large and thinly recrystallized areas up to 0.5 mm wide. The chert matrix contains radiolarian fossils completely recrystallized to quartz, as well as fine-grained carbonate.

Structure

Veins

Veins were observed in serpentinized ultramafic and mafic rock clasts from Holes U1498A and U1498B (Figures F8, F18, F19). The

Figure F18. Veined ultramafic rock clasts, Hole U1498A. A. Serpentine veins (3R-2, 18–30 cm). B. Serpentine veins (dark) crosscut by a carbonate vein (bright) (3R-3, 16–22 cm).



U1498A-3R-2, 18-30 cm

U1498A-3R-3, 16-22 cm

veined serpentinized ultramafic rock clasts are largely observed in both holes; the veined volcanic clasts are only observed in Hole U1498B in the top part of Section 8R-1.

The ultramafic clasts are dominantly crosscut by 1 mm thick serpentine veins that occur as single to multiple sets. The isolated veins are often haloed with a serpentine seam up to 6 mm wide. The networks are composed of various vein types with geometry ranging from straight to kinked and colors ranging from black to pale green to white.

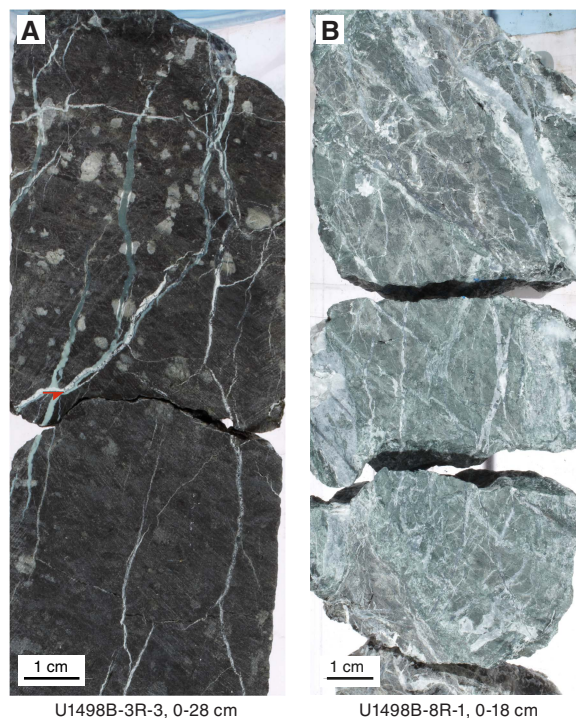
Apart from serpentine veins in serpentinized ultramafic clasts, single occurrences of veins with other filling material are noticeable. A single fibrous calcium carbonate vein crosscutting a serpentine vein was recovered in an ultramafic rock clast in Section 366-U1498A-3R-3, 16–22 cm. Several thick (up to 5 mm) white single veins crosscut potential mafic clasts.

Few breccia were recovered from Cores 366-U1498A-2R and 3R. These breccia are polymict and contain clasts of ultramafic rock, vesicular volcanic rock, green and white serpentine chips, and nonvesicular basalt. The clasts are mainly granule sized, with several reaching 2 cm (Figure F20).

Core 366-U1498B-21R contains ultramafic rock and mafic rock with few carbonate veins, as well as metamorphic cherty limestone with chert layers, all embedded in serpentinite mud (Figure F8). The contact between the ultramafic rock and the metabasite is sheared along a 5 cm wide cataclastic shear zone, whereas the primary contact between the metabasic rock and the cherty limestone is preserved, though in an inverted stratification. The layering and the carbonate/greenstone contact have dip angles of 5° to 30° within the drill hole.

The fine-grained micritic carbonates are brecciated due to cataclastic deformation, macroscopically representing a protocataclastic cemented by coarse-grained sparitic calcite with a still-

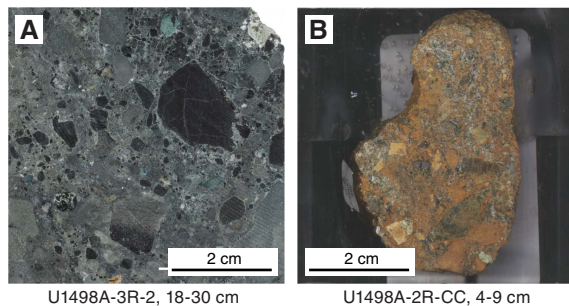
Figure F19. Large veined clasts, Hole U1498B. A. Ultramafic rock clasts with serpentine veins (3F-3, 0–28 cm). B. Mafic rock clasts with wide carbonate veins (8R-1, 0–18 cm). Red arrow = direction of movement on the wide fault trace filled by carbonate.



U1498B-3R-3, 0-28 cm

U1498B-8R-1, 0-18 cm

Figure F20. Breccias, Hole U1498A. A. Polymict breccia (3R-2 [Piece 15, 18–30 cm]). B. Oxidized polymict breccia clast (2R-CC [Piece 2, 4–9 cm]).



discernible primary sedimentary layering, subsequently sheared along conjugate high-angle normal faults that have dip angles between 70° and 80° within the drill hole. Coarse-grained sparitic calcite was precipitated within veins and gashes. Precipitation of calcite from mobilized fluids was also observed along the bottom contact of the carbonates toward serpentinite mud, forming a reaction seam with ophicarbonates.

Core 23R contains a tectonic breccia that crosscuts a greenstone (Figure F21). This breccia is composed of clasts of the host rock and thin white veins that are not carbonate. This breccia and a light green clay layer of the host rock that thins horizontally from 3 to 1 cm are both displaced by approximately 5 mm. Two thick (>0.5 cm) white veins vertically crosscut the structure.

Lithostratigraphy, petrology, and structure summary

Site U1498 consists of a wide variety of components, including multicolored serpentinite sand and silt, bluish gray serpentinite mud with ultramafic rock clasts (stones and boulders), boulders of metabasite (Cores 366-U1498B-21R and 23R), cherty limestone (Core 21R), and microbreccia clasts that contain droplets of hydrous glass of unusual composition and uncertain provenance, boulders of serpentinitized harzburgite, microfossiliferous sediment, and metavolcanic rocks in a vitric mesostasis (Core 366-U1498A-3R). These clasts and boulders are invariably embedded within serpentinite pebbly mud, although much of that matrix was lost to mud circulation during rotary drilling.

The colorful serpentinite sequences of Subunit IIIA in Hole U1498A are composed of aragonite-enriched brownish serpentinite mud (as much as 5% in Sample 4R-2, 45 cm), light green layers with clear serpentine grains, and a magnetite-enriched dark blue layer and are exactly comparable with Unit I in Hole U1492A in both color and mineral composition. The aragonite is likely the product of reaction between serpentinite mud pore fluid and seawater, and the limonite or hematite in the brownish layer suggests oxidation of magnetite. We infer that the brown and light green layers represent redox boundaries within single serpentinite mudflow layers or the distal edges of individual mudflows.

Within Core 366-U1498B-21R, the metavolcanic boulder overlies cherty limestone and the preserved primary contact between them is inverted. The texture and mineralogical composition of both the metavolcanic (greenstone with chlorite and amphibole) and cherty limestone indicate low- to medium-grade metamorphic overprint of these lithologies. Preserved cataclastic faults and extensional structures within these metamorphic rocks (high-angle normal faults and extensional veins) might either be related to shearing within the subduction channel and bending of the lower

Figure F21. Fault zone in large greenstone clast (366-U1498B-23R-1, 35–70 cm). Red arrows = direction of displacement on faults bounding the fault zone.

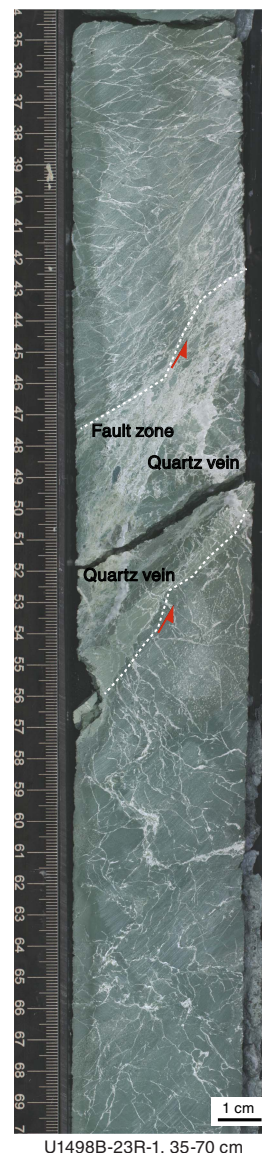


plate during subduction or to faulting during the early stages of exhumation. In addition, the deformed sediments appear to contain microfossils such as radiolarians that are common in older sediments of the Pacific plate, and the presence of ultracataclasite requires severe brittle deformation that is not likely to occur in sediments lying on top of the upper plate. For these reasons, the metavolcanic–carbonate interval is tentatively inferred to be a remnant of a subducted guyot from the Pacific plate. The lowermost cored intervals in Holes U1498A and U1498B are deposits of microfossil-bearing volcanic ash defining the seafloor upon which the mud volcano was built.

Rock and sediment geochemistry

Elemental abundances for Site U1498 samples selected by the shipboard scientific party were determined using inductively coupled plasma–atomic emission spectroscopy (ICP-AES) and porta-

ble X-ray fluorescence spectrometer (pXRF) analysis. pXRF calibration curves are provided in Figure F2 in Johnston and Ryan (2018). The examined samples included serpentinite muds and serpentinitized ultramafic rocks (harzburgites and/or dunites). A full discussion of Expedition 366 rock and sediment data is found in **Sediment and rock chemistry** in the Expedition 366 summary chapter (Fryer et al., 2018b).

Fluid geochemistry

Headspace analysis of CH₄ and other hydrocarbons

Interstitial water CH₄ and C₂H₆ concentrations were below detection limit in samples from Hole U1498A (the deeper of two flank sites of Fantangisña Seamount) (Table T4). However, in Hole U1498B (the shallower of two flank sites of Fantangisña Seamount), interstitial water CH₄ and C₂H₆ concentrations were detected at several depths by gas chromatograph (GC)–flame ionization detector (FID). Both CH₄ and C₂H₆ concentrations are generally low, but at 115.7 mbsf (Section 366-U1498B-13R-4), high interstitial water CH₄ concentrations were measured (Figure F22). This sample has a C₁/C₂ ratio that is generally high (2.6–59.3) for serpentinite mud volcanoes, corresponding to the range of typical thermogenic methane rather than that of fluid conduit methane (200–500) observed in other serpentinite mud volcanoes in the Mariana forearc (see **Fluid geochemistry** in the Site U1496 chapter [Fryer et al., 2018e]). The depth-dependent profiles of CH₄ and C₂H₆ do not correlate with the interstitial water H₂ concentration profile. In addition, no significant signature of microbial sulfate reduction was observed, as indicated by AVS concentrations. These results suggest that the interstitial water CH₄ and C₂H₆ may be derived from abiotic sources.

Electrochemical sensor measurements of H₂ and H₂S

There was no detectable H₂ in samples from Hole U1498A (Table T5). However, relatively low H₂ concentrations were detected in more than half of the samples from Hole U1498B, as measured by an H₂ electrochemical sensor. The highest H₂ concentration was measured in a sample from 75 mbsf (Section 366-U1498B-9R-1), where no significant CH₄ was detected (Table T4). The only detect-

able AVS concentrations were in a single zone (201.6 mbsf; Section 23R-2) that corresponds to the depth where considerable H₂ was detected (Figure F22). These elevated H₂ and sulfide concentrations do not correspond to any patterns of interstitial water pH, chloride, or sulfate concentrations at Site U1498.

Interstitial water

The salinity, pH, alkalinity, and chlorinity of the 17 interstitial water samples collected from Holes U1498A and U1498B were measured within a few hours after sampling. Samples were analyzed for ammonium, phosphate, and H₂S by UV-vis spectrophotometry; Ca, Mg, K, Na, Br, and SO₄²⁻ concentrations were measured by ion chromatography; and trace (Si, Li, B, Mn, Fe, Sr, and Ba) cation concentrations were measured using the shipboard Teledyne Leeman Labs Prodigy ICP-AES instrument. The wavelengths examined for these elements are in Table T1 in the Expedition 366 methods chapter (Fryer et al., 2018a). The results of these analyses are reported below.

Alkalinity, pH, salinity, and chlorinity

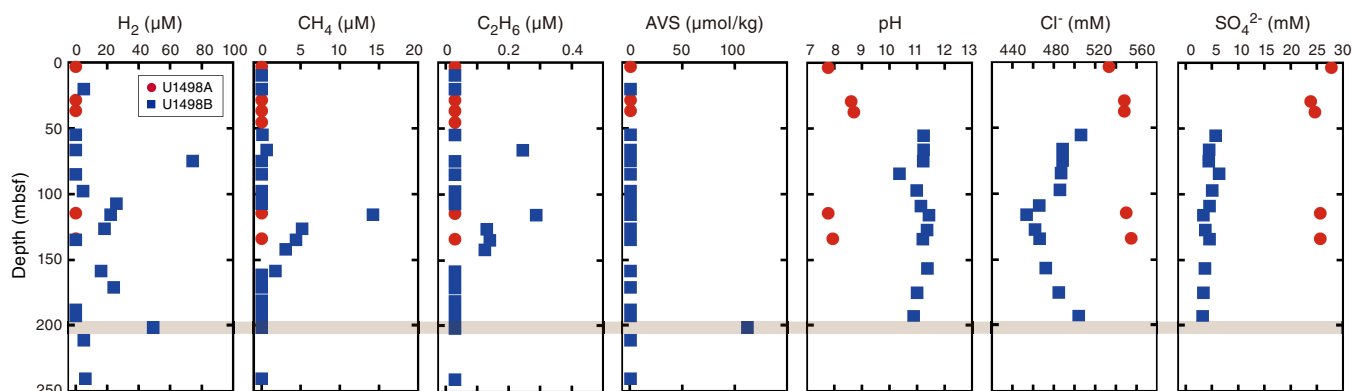
Deeper than ~4 mbsf in Hole U1498A, alkalinity is lower than the seawater value (minimum of 0.5 mM vs. 2.3 mM in seawater), whereas in Hole U1498B, alkalinity is highly variable (2.0–5.4 mM) but consistently higher than the seawater value, reaching a maximum of 5.4 mM at ~116 mbsf (Table T6; Figure F23). Significant differences in pH are evident between Holes U1498A and U1498B; in Hole U1498A, pH ranges from 7.8 to 8.7, whereas in Hole U1498B, pH ranges from 10.4 to 11.4. In general, pH and alkalinity correlate with each other ($R^2 = 0.9$), except for one sample at ~85 mbsf.

Salinity is also considerably different in Holes U1498A and U1498B. In Hole U1498A, salinity is similar to seawater (35), ranging between 35 and 36. In contrast, salinity in Hole U1498B is considerably lower than seawater, ranging between 26 and 30; the highest value was recorded in the deepest core from this hole (193 mbsf) (Figure F23). Chlorinity values determined by titration are, like salinity, similar to seawater for Hole U1498A but significantly

Table T4. Interstitial water methane and ethane concentrations determined by GC-FID, Site U1498. [Download table in CSV format.](#)

Table T6. Interstitial water analyses, Site U1498. [Download table in CSV format.](#)

Figure F22. Headspace and interstitial water H₂, CH₄, and AVS concentrations, Holes U1498A and U1498B. CH₄/H₂ ratio and pH, chloride, and sulfate concentrations are shown for comparison. Brown shading highlights sulfidic zone potentially associated with subseafloor microbial sulfate reduction.



less for Hole U1498B, with values as low as 454 mM compared to 542 mM for seawater.

Phosphate, ammonium, sulfate, sulfide, chloride, and bromide

Phosphate concentrations in interstitial fluids from Holes U1498A and U1498B are lower than the seawater value, ranging between 0.34 and 1 μM , with the exception of Sample 366-U1498A-1R-3, 110–125 cm, which has a phosphate level of 1.96 ppm (Table T6; Figure F24).

Sulfate concentrations are similar to seawater (28 mM) in Hole U1498A but are about five times lower in Hole U1498B. This difference could reflect mixing with seawater in Hole U1498A or a much more reducing environment in Hole U1498B.

Measured ammonium concentrations increase in both holes from near 20 μM to as high as 80 μM but are generally around 42 μM deeper than 100 mbsf (Figure F24). These values are similar to ammonium concentrations recorded on the flank sites of Yinazao Seamount (Site U1491) but are lower than those at the Yinazao and Asùt Tesoru summit sites. The presence of ammonium may reflect the reduction of nitrates. These values are much higher than those measured on the Fantangisña summit (Site U1497), where concentrations approach 0 μM . HS^- concentrations are close to but slightly above the detection limit (<0.1 μM), ranging between 0.1 and 0.2 μM .

Chloride and bromide in Hole U1498A are close to seawater concentrations (Figure F25), indicating either a high degree of mix-

Figure F23. Interstitial water alkalinity, pH, and salinity concentrations, Holes U1498A and U1498B. Bottom seawater values are from Mottl et al. (2003, 2004).

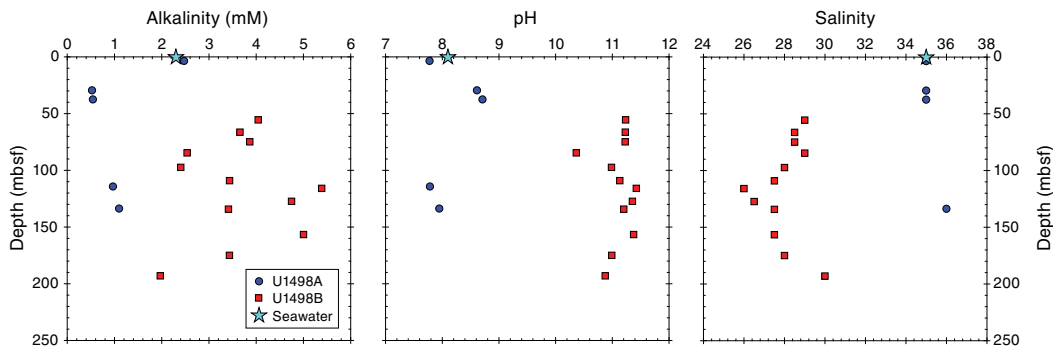


Figure F24. Interstitial water phosphate, sulfate, and ammonium concentrations, Holes U1498A and U1498B. Bottom seawater values are from Mottl et al. (2003, 2004).

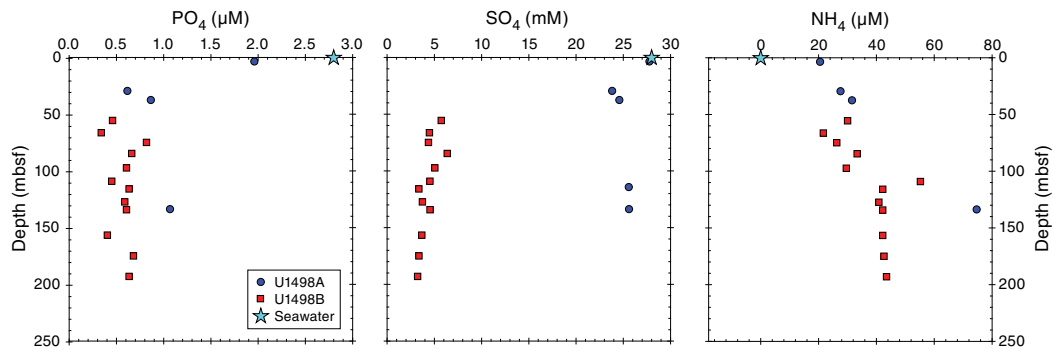
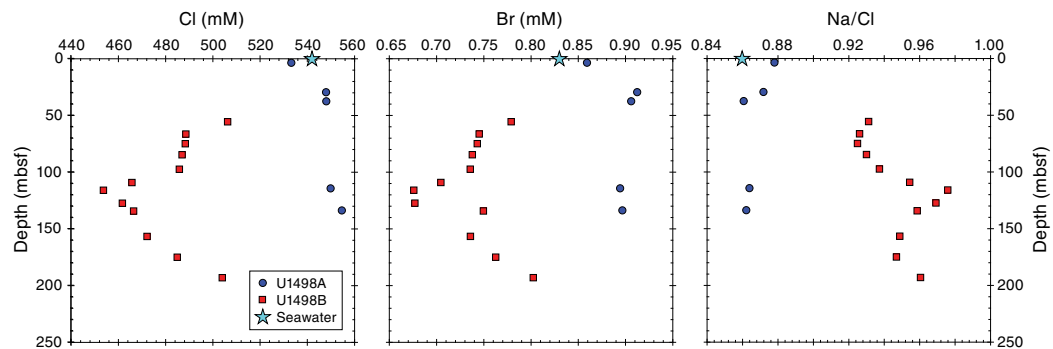


Figure F25. Interstitial water Cl, Br, and Na concentrations, Holes U1498A and U1498B. Bottom seawater values are from Mottl et al. (2003, 2004).



ing or the presence of seawater in the interstitial fluids serving as the medium for serpentinization. In contrast, chloride and bromide concentrations exhibit a different trend with depth in Hole U1498B. In the uppermost 50 m of Hole U1498B, concentrations are ~10% less than bottom seawater. Deeper than ~50 mbsf in Hole U1498B, chloride and bromide concentrations decrease with depth to 120 mbsf before increasing to near-surface values at 200 mbsf. The depletion of chloride and bromide may reflect precipitation into accessory phases or diffusive transport after a temporal input such as the deposition of serpentinite material over existing deposits.

Major and trace cations

Holes U1498A and U1498B show distinct trends in their major and trace element abundances with depth (Figure F26). Ba concentrations are consistently below the ICP-AES detection limit (0.015 μM) in samples from Hole U1498A, consistent with most samples analyzed during Expedition 366. In contrast, Ba concentrations in Hole U1498B samples increase from approximately 0.1 μM near the seafloor to 1.4 μM at 175 mbsf and are the highest Ba concentrations sampled during Expedition 366. B concentrations in interstitial waters are near the seawater value (410 μM) in Hole U1498A and significantly lower than the seawater value in Hole U1498B, ranging from ~60 to ~125 μM (Figure F26). Li concentrations generally decrease with depth in both holes, though more significantly in Hole U1498A. In contrast, Sr concentrations increase from seawater values (90 μM) to about 165 μM at 30 mbsf in Hole U1498A and to a maximum of 327 μM at 193 mbsf in Hole U1498B.

Fe concentrations in interstitial waters are below the detection limit of the ICP-AES (<0.69 μM), with the exception of two samples. Mg concentrations in Hole U1498A decrease with depth from 36 to 24 mM. In contrast, samples from Hole U1498B have Mg concentrations that are generally below the analytical detection limit (<1.6 mM). K concentrations exhibit seawater-like values of ~9–10 mM at shallow depths in both holes and decrease linearly with depth to a minimum of 7.5 mM. Ca concentrations increase from near seawater values (10.2 mM) in Hole U1498A to 36.7 mM at 133.8 mbsf and decrease from 18.3 mM at ~55 mbsf in Hole U1498B to 11.3 mM at ~193 mbsf.

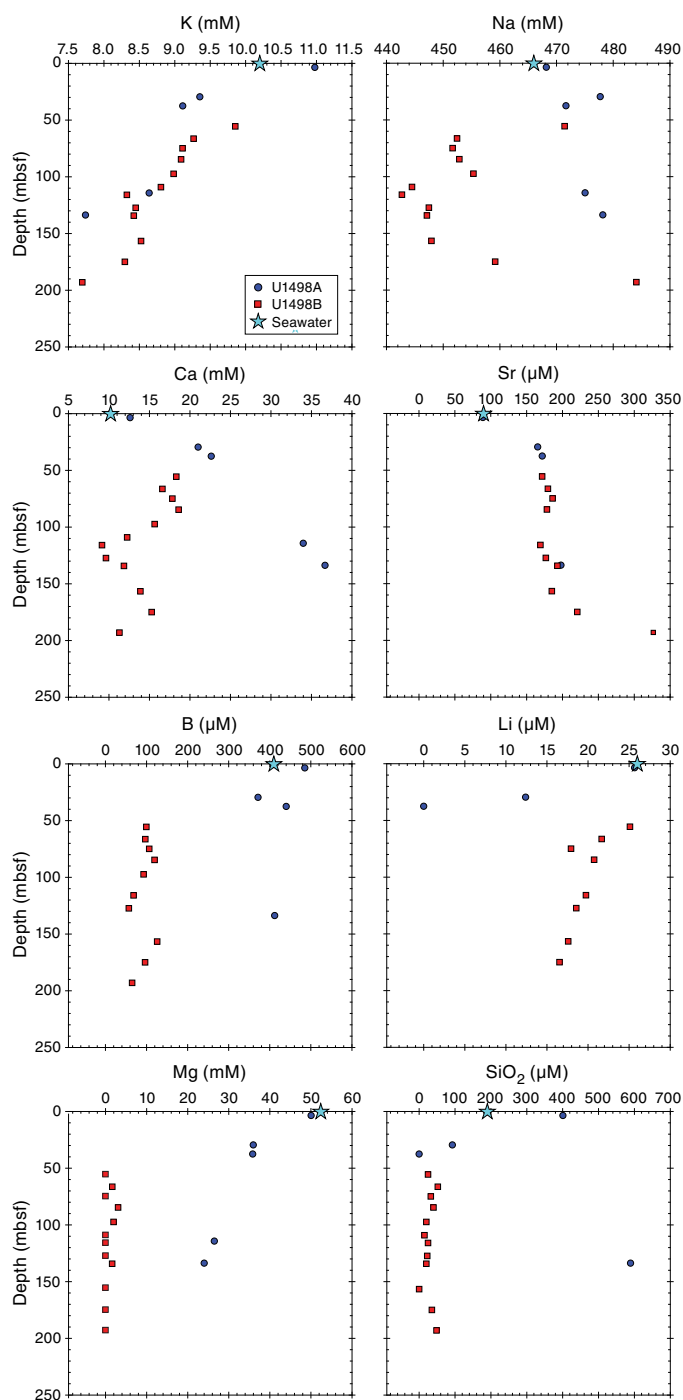
Na concentrations in interstitial fluids range from 468 to 478 mM in Hole U1498A. This range is similar to the seawater value. In Hole U1498B, concentrations of Na range between 443 and 484 mM and exhibit no particular trend downhole.

The Na/Cl ratio is similar to the seawater value (0.86) in Hole U1498A. In Hole U1498B, however, Na/Cl ratios are greater than seawater, generally increase to 0.98 at ~109 mbsf, and then decrease and are anticorrelated to the chloride concentrations.

Dissolved inorganic carbon/dissolved organic carbon

Apart from the shallowest sample from Hole U1498A (3.6 mbsf), which probably reflects a higher degree of seawater mixing with interstitial fluids, dissolved inorganic carbon (DIC) values are consistently lower than seawater (24 ppm) (Figure F27). In Holes U1498A and U1498B, DIC concentrations range between 4 and 6 ppm in the upper 80 m and up to 8–10 ppm near the base of each hole. In contrast, dissolved organic carbon (DOC) values are higher than seawater (0.5 ppm). In Hole U1498A, values range between 1.7 and 3.6 ppm above 50 mbsf and decrease to 1.4–2 ppm below 100 mbsf. In Hole U1498B, DOC concentrations display more variation. Concentrations range between 3.1 and 8.5 ppm from 50 to 150 mbsf and between 3.9 and 5 ppm below 150 mbsf.

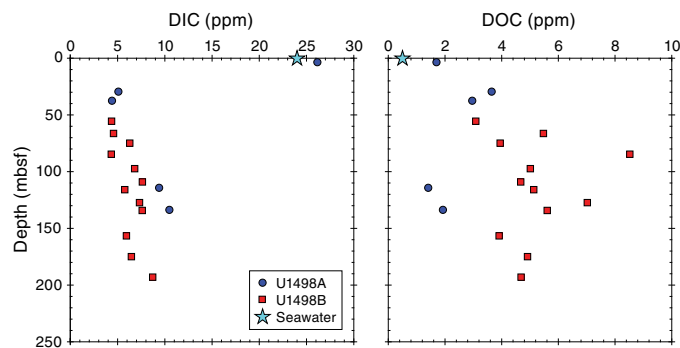
Figure F26. Interstitial water K, Na, Sr, Ca, B, Li, Mg, and SiO_2 concentrations, Holes U1498A and U1498B. Bottom seawater values are from Mottl et al. (2003, 2004).



Summary

The two holes at Site U1498 reflect markedly different conditions in terms of their interstitial water chemistries. Hole U1498A is closer to the toe of the volcano, similar to Site U1491 at Yinazao Seamount, and the fluids have a seawater-dominated signature that also reflects diagenetic reactions with serpentinite muds, clasts, and sands, as well as modified sediments. In contrast, Hole U1498B is

Figure F27. Interstitial water DIC and DOC concentrations, Holes U1498A and U1498B. Bottom seawater values are from Eglinton and Repeta (2014).



similar to a flank site (ODP Hole 779A) at Conical Seamount, which was drilled during Leg 125 (Mottl, 1992); at and below 50 mbsf, the fluid pH is consistently >10.5 , suggesting that serpentinization continues to be active in this material.

The interstitial water “fingerprint” of Fantangisña Seamount, based on trends at Site U1497 and the concentration levels of key cations and anions in Hole U1498B, appears to best match that of Yinazao Seamount, with elevated Sr, low B and K, low Na and Cl, and low salinity. The “fit” is not perfect because some cations (Ca in particular) show less overall enrichment, and Holes U1498A and U1498B have different trends, perhaps suggesting some later stage removal of Ca. In Hole U1498B, Ba concentrations are unusually high, coincident with the lowest concentrations of sulfate measured during Expedition 366.

Microbiology

Sample recovery

Microbiology sampling during Expedition 366 focused on exploring the limits of microbial life in serpentinite mud habitats across multiple depths using cultivation-based and cultivation-independent molecular biological approaches, microscopy, and assays for the detection of viruses. Sampling efforts targeted both near-surface and deeper whole-round cores, especially if there was evidence of transitions across gradients of microbiologically affecting compounds and gases (e.g., hydrogen, methane, hydrogen sulfide, and sulfate). Two 20 cm long whole-round samples were collected at each sampled depth for general microbial analyses. Additional whole-round samples were collected for individual investigations. A total of 15 whole-round samples were collected for general microbial sampling from the flank of Fantangisña Seamount at Site U1498. These samples were preserved and will be analyzed post-expedition as described in **Microbiology** in the Expedition 366 methods chapter (Fryer et al., 2018a).

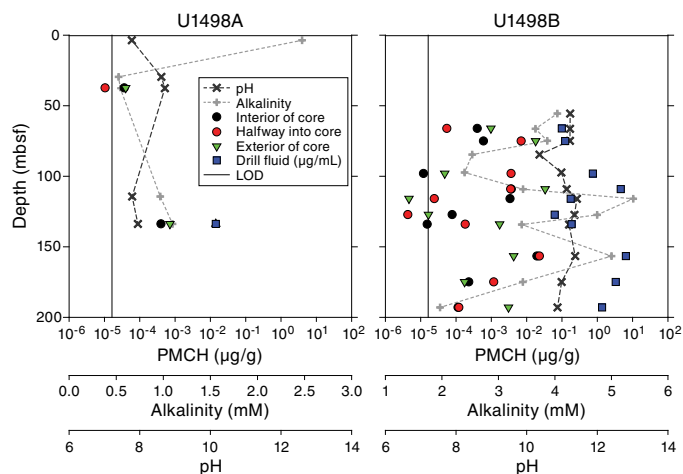
Contamination testing

Contamination testing at Site U1498 was conducted using perfluoromethylcyclohexane (PMCH) tracer. Because of low core recovery and difficulties during sampling for PMCH (e.g., rocks) in the designated microbiology whole rounds from Hole U1498A, sample recovery for PMCH tracers was low (Table T7; Figure F28). Given the limited number of tracer samples taken at this site, conclusions cannot be made as to the quality of samples for microbiological purposes from Hole U1498A. Results for Hole U1498B indicate successful tracer delivery; however, the high level of tracer concentration throughout the samples, including the interior of the

Table T7. Summary of PMCH contamination assessment data, Site U1498.

[Download table in CSV format.](#)

Figure F28. PMCH concentrations from the interior, halfway, and exterior of the microbiology whole-round, the top of the core, and the drilling fluid recovered from the top of the core, Site U1498. LOD = limit of detection for PMCH analysis. Alkalinity and pH data are shown to provide a measure for the level of active serpentinization and potential seawater contamination (see Fluid geochemistry).



core, suggest that whole-round samples may be contaminated with drilling fluid and are poor for microbiological analyses. These results were anticipated because of the use of RCB drilling. However, these samples could still be usable for certain investigations because high in situ pH levels within the mud are likely to select for indigenous microorganisms.

Physical properties

Physical property data were acquired for Site U1498, located on the flank of Fantangisña Seamount. Two holes, U1498A and U1498B, were cored 700 m apart at this site, penetrating to 181.6 and 260 mbsf, respectively. Hole U1498B is situated upslope from Hole U1498A.

The Whole-Round Multisensor Logger (WRMSL) was used to measure wet bulk density using gamma ray attenuation (GRA), magnetic susceptibility, and *P*-wave velocity on the *P*-wave logger (PWL). The whole rounds were then logged for NGR. Discrete thermal conductivity measurements were performed on one or two whole rounds per core, depending on recovery. Color reflectance and point magnetic susceptibility (MSP) were measured on archive section halves. In addition, shear strength (automated vane shear) was measured on the working halves, and discrete samples were collected for moisture and density (MAD) measurements of wet and dry bulk density.

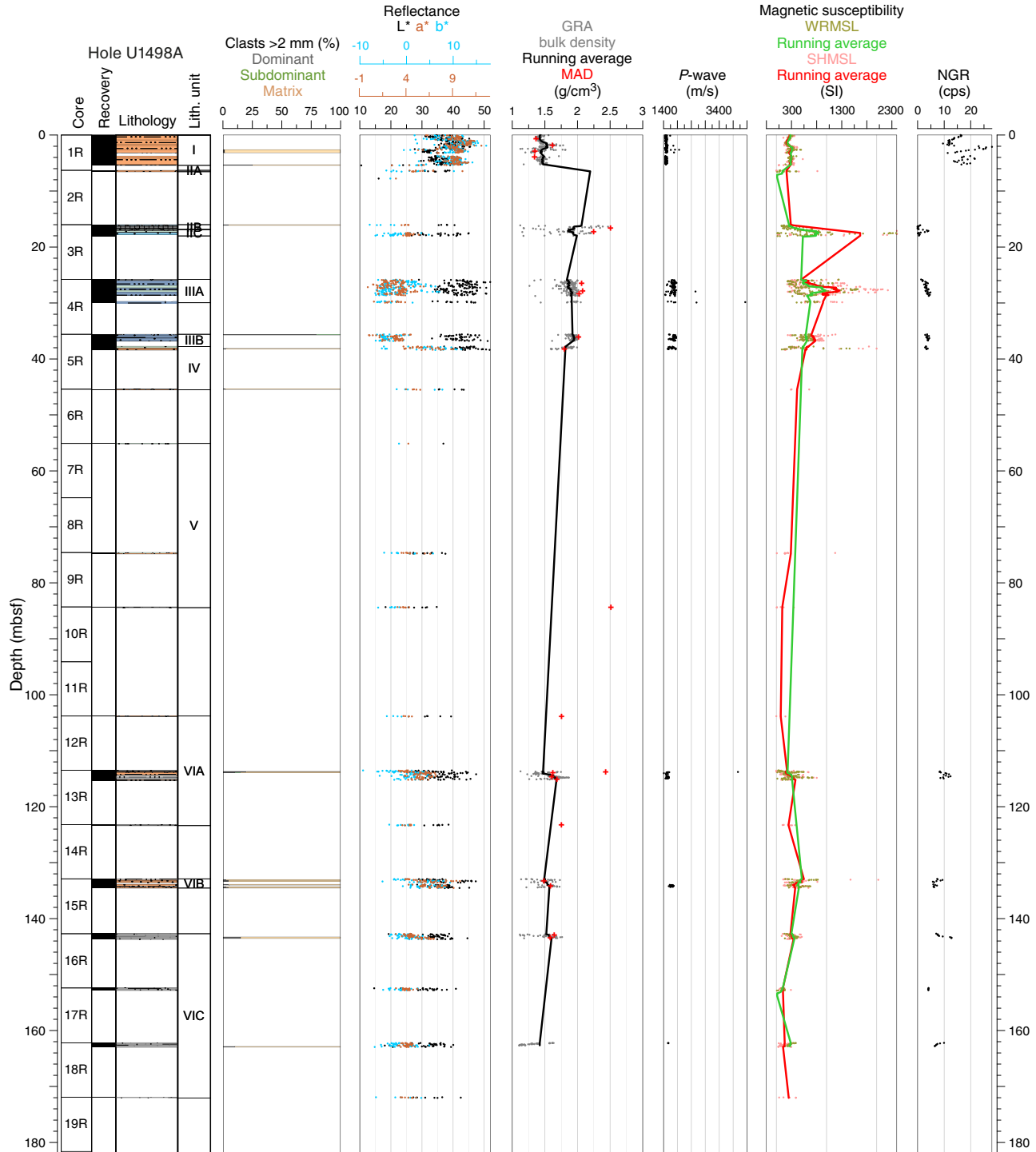
Core sections frequently contained hard rock fragments and gravel or had poor sediment-to-liner coupling, resulting in high *P*-wave velocity signal attenuation, and data acquisition on both the WRMSL and Section Half Measurement Gantry (SHMG) was compromised on such core sections. These data sets are nevertheless presented here to be consistent with the other site chapters. Other data sets are mostly of medium quality in Hole U1498B, whereas in Hole U1498A they were influenced by the low recovery (11%). Physical property measurements were performed to help characterize the lithostratigraphic units and describe the mechanical and ther-

mal states of the serpentinite mud volcanoes. Precise intervals of lithostratigraphic units and subunits from core description (see **Lithostratigraphy**) are used to describe physical property trends and calculate average values. Data in the figures were filtered to remove spurious points that correspond to empty intervals in the liner or broken pieces. All of the onboard results and data interpretation are presented below.

GRA bulk density

The Hole U1498A bulk GRA density record exhibits low continuity of the data set due to low recovery (Figure F29). The top of the hole, corresponding to the first core with ash-bearing pelagic sediment, has average GRA density values ranging between 1.4 and 1.5 g/cm³, with scattering to lower and higher density values. Below 5.4 mbsf, the record becomes very scarce, and continuous measure-

Figure F29. Color reflectance, GRA density and discrete bulk density, P-wave velocity, magnetic susceptibility, and natural gamma radiation data, Hole U1498A.

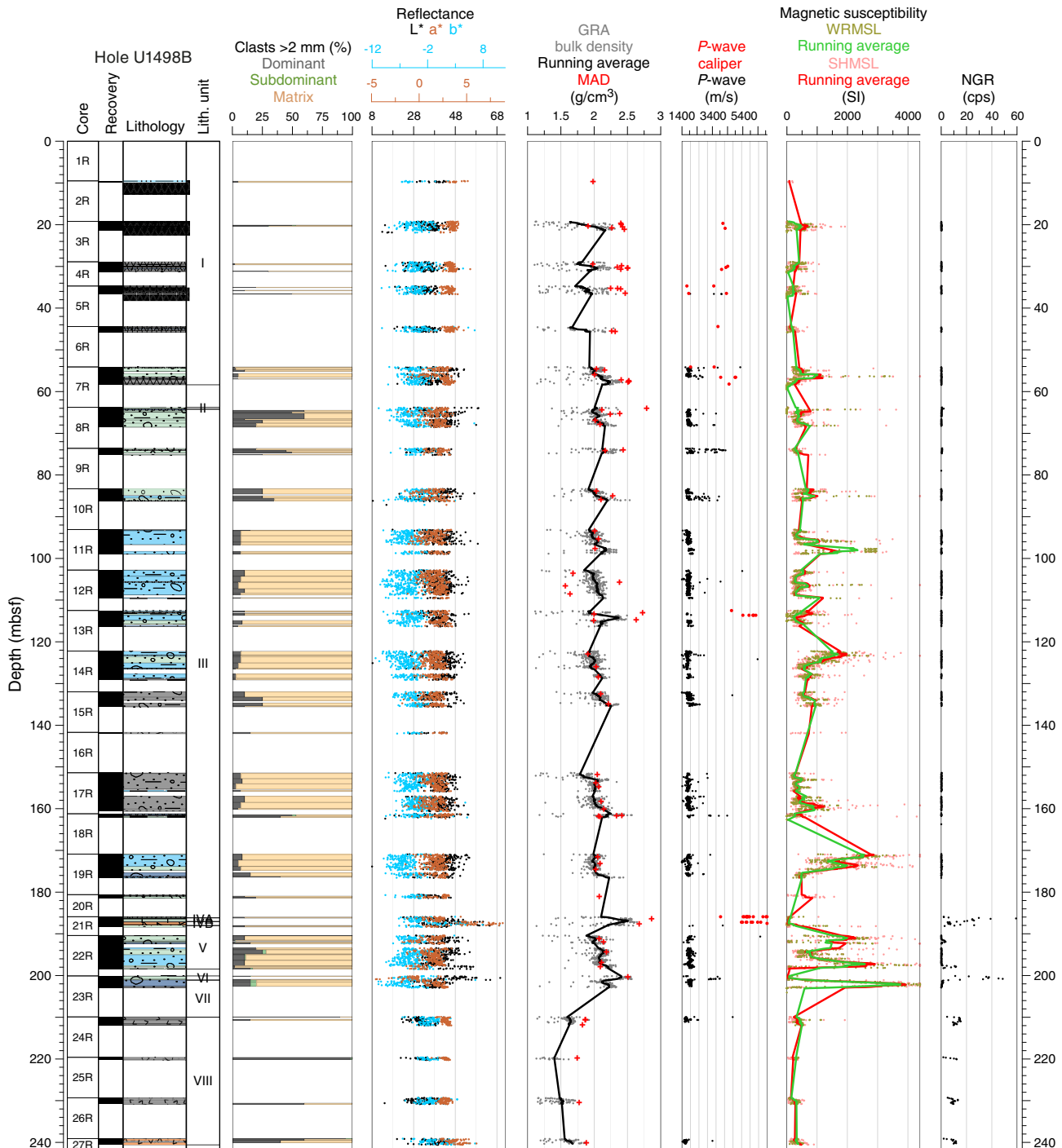


ments were only acquired in some sections in Cores 3R, 4R, 5R, 13R, 15R, and 16R. Average bulk GRA densities in Core 3R, corresponding to rock clasts (lithostratigraphic Unit II), range 1.8–2.1 g/cm³ with large scattering of values, underestimating the actual bulk density. Core 5R, which contains serpentinite sand with no clasts (Unit III), has values ranging 1.8–2.0 g/cm³. Average bulk GRA density values in Cores 13R–17R (Unit VI, volcanic ash layers rich in nannofossils) range 1.4–1.7 g/cm³ but with large scattering of the values due to either the presence of rock clasts and well-consolidated ash layers that cause increased GRA values or the pres-

ence of friable ash layers, more easily disaggregated during drilling, forming voids and empty spaces with lower GRA values.

The bulk GRA density record in Hole U1498B (Figure F30) is also discontinuous because of low recovery. The record also shows large scattering of the values, probably due to both the lithologic characteristics and the drilling method. From ~19 to 64 mbsf (Units I and II), the recovered cores, composed mainly of rock clasts with rare serpentinite mud, are prone to voids, causing scattering of the GRA density values. From ~64 to 186 mbsf, the retrieved cores are composed mainly of serpentinite mud with lithic clasts and have av-

Figure F30. Color reflectance, GRA density and discrete bulk density, *P*-wave velocity, magnetic susceptibility, and natural gamma radiation data, Hole U1498B.



erage values ranging 1.9–2.3 g/cm³, with some scattering into both lower values (due to the presence of voids) and higher values (due to the presence of large clasts). Units IV and VI are characterized by preferential recovery of rock clasts, with average GRA density values of ~2.5 g/cm³, distinctly higher than the serpentinite mud. Below ~210 mbsf in Unit VIII, which is composed of ash layers with variable compaction and consolidation, GRA density values are below 1.75 g/cm³, which is significantly lower than values in the units above.

For Holes U1498A and U1498B, GRA bulk density values are generally in good agreement with the MAD measurements. The data variations for the two methods track each other. Some high MAD density values are observed in both holes, but those measurements were made on isolated clasts or in clasts of gravel material and therefore are higher than whole-round GRA bulk density.

P-wave velocity

Whole-round and discrete *P*-wave measurements were performed using the WRMSL and the SHMG. In Hole U1498B, *P*-wave caliper (PWC) measurements were successfully done on well-consolidated rock clasts from Cores 3R–7R, 13R, 20R, and 21R. Because of difficulties in recovering sediment cores in their pristine *in situ* conditions, *P*-wave velocity measurements in most Site U1498 cores were not always possible within the required quality standards defined by the acquisition software. Consequently, the *P*-wave velocity records show several depth intervals with no velocity data. The *P*-wave velocity data are generally characterized by large scattering of the values. However, a clear clustering of most of the values usually defines a minimum velocity that is interpreted as the characteristic velocity of a particular lithology (e.g., pelagic sediment or serpentinite mud). In these holes, *P*-wave velocity data frequently exhibit dispersion above this level, indicating higher velocities that are interpreted as reflecting the presence of large individual clasts or higher numbers of rock clasts that have *P*-wave velocities higher than the mud matrix.

P-wave velocity in the uppermost core of Hole U1498A (Figure F29), which is composed mainly of pelagic sediment, shows a near-constant value of ~1500 m/s. Below this depth, between 25 and 38 mbsf, the data is more scattered, with a *P*-wave velocity threshold ranging between ~1700 and 1900 m/s. *P*-wave velocity values above this velocity threshold, which can reach as high as 3900 m/s, are interpreted as reflecting point measurements that include larger individual lithic clasts or higher amounts of clasts with high *P*-wave velocities. *P*-wave velocities below 103 mbsf in Unit VI, composed of volcanic ash deposits, range between 1500 and 1750 m/s.

WRMSL *P*-wave velocities in Hole U1497B (Figure F30) were not measured in the uppermost 50 m of the hole. From 50 to ~210 mbsf, values range from a threshold value of ~1650 m/s to ~2000 m/s, with scattering of data values up to 4000 m/s that are interpreted as resulting from the presence of large individual rock clasts or higher amounts of clasts with high *P*-wave velocities. This interpretation is supported also by the PWC velocities obtained on individual large rock clasts at ~113 (Unit III) and 187–188 mbsf (Subunit IVB), where *P*-wave velocity values range between 3675 and 6800 m/s. WRMSL *P*-wave velocities in Unit VIII, which includes the indurated volcanic ash deposits, show lower values between ~1500 and ~1700 m/s.

Reflectance spectroscopy and colorimetry

Hole U1498A color reflectance parameters show in general a good positive correlation between parameters *a** and *b**: sediments that are more green and less red (negative *a**) are also more blue

(negative *b**). Lightness is the more variable parameter throughout the hole. In the serpentinite mud breccia, no clear correlation between *L** and *a** or between *L** and *b** was observed (Figure F29), but in the uppermost core's pelagic sediment and the ash layers, a good correlation between *L** and *a** and between *L** and *b** was observed. The reflectance parameters correlate well with the lithostratigraphic units. Unit I is characterized by higher *a** (red) and higher *b** (yellow) values, whereas the serpentinite mud in Units II and III is characterized by lower *a** (green) and lower *b** (blue) values. The volcanic ash layers with nannofossils in Unit VI are characterized by intermediate *a** and *b** values relative to the other main lithologic units.

In Hole U1498B, *a** and *b** (Figure F30) have generally low variability and no clear correlation with each other. Lightness has larger variability throughout the hole, but no clear trend with depth can be identified. Subunit IVB (187–188 mbsf), composed of limestone with thin chert layers, is characterized by a positive correlation between *a** and *b** and by higher *a** (red) and *b** (yellow) values. Unit VIII (209–240 mbsf), which is composed of dark gray nannofossil-bearing lithified volcanic ash, has lower variability in all the color reflectance parameters and lower *L** values (darker color), higher *a** (red), and higher *b** (yellow) values than the serpentinite mud.

Magnetic susceptibility

In Holes U1498A and U1498B, magnetic susceptibility measurements with the WRMSL and MSP produced similar results. An offset between both magnetic susceptibility data sets was observed. However, both show similar trends and local variations. Of all physical properties, the magnetic susceptibility profiles show the largest fluctuations at the meter and submeter scales. Submeter-scale fluctuations are especially evident in the core sections with hard rock fragments, which were often recovered in incompletely filled core liners.

In Hole U1498A (Figure F29), the top thin clayey mud unit with pelagic components (Unit I) is characterized by relatively constant magnetic susceptibility values, averaging 272×10^{-5} SI. Unit II, which is composed of a series of serpentinitized ultramafic rocks partly filling the core sections, has highly variable values between 0 and over 3000×10^{-5} SI. Despite the gaps, which are responsible for the lowest values, magnetic susceptibility variations in the relatively high values suggest variable magnetic mineral content between the different ultramafic rock fragments. Unit III consists of variable thickness intercalations of different colored (blue, green, and yellow-orange) serpentinite sand and mud. Magnetic susceptibility variations in this unit are well correlated to the color variation between these layers, with values generally higher than 1000×10^{-5} SI in the blue layers and $\sim 300 \times 10^{-5}$ to 500×10^{-5} SI in the green and yellow-orange layers. Units IV and V, which were only recovered in core catcher sections, were not analyzed on the WRMSL and are not described here. The three subunits of Unit VI, which are composed of volcanoclastic deposits with variable content of pelagic and ultramafic components, have magnetic susceptibility values ranging from 36×10^{-5} to 824×10^{-5} SI (average = 322×10^{-5} SI).

In Hole U1498B (Figure F30), Unit I is composed of a series of serpentinite ultramafic rocks partly filling the core sections with intercalations of serpentinite mud. This unit has highly variable magnetic susceptibility from less than 10×10^{-5} to $\sim 3500 \times 10^{-5}$ SI for the highest peaks. Although the lowest magnetic susceptibility values are artifacts caused by air gaps between rock fragments in the liners, an average of 332×10^{-5} SI was calculated for this unit, and the magnetic susceptibility peaks suggest variable magnetic mineral content between the different ultramafic rock fragments. The lower

units (III, V, and VII) consist of serpentinite mud deposits with variable ultramafic rock clast content, the predominant material recovered in this hole. These units are characterized by average magnetic susceptibility values of 680×10^{-5} , 1401×10^{-5} , and 2484×10^{-5} SI, respectively, and show higher peak values than Unit I ($\sim 3500 \times 10^{-5}$ SI). The other units recovered in Hole U1498B are composed of different material and stand out from the serpentinitized materials described above with significantly lower magnetic susceptibility values. The metavolcanic rock of Unit II at ~ 64 mbsf has an average magnetic susceptibility of 15×10^{-5} SI. At 186–188 mbsf, Subunits IVA (metabasite) and IVB (cherty limestone) have average magnetic susceptibility values of 50×10^{-5} and 20×10^{-5} SI, respectively. The mafic metavolcanic rock in Unit VI at ~ 200 mbsf has an average magnetic susceptibility of 36×10^{-5} SI. Finally, at the bottom of this hole, the indurated volcanic ash deposits of Unit VIII are characterized by rather constant magnetic susceptibility values with an average of 322×10^{-5} SI.

Natural gamma radiation

In spite of low recovery in Hole U1498A, the NGR measurements highlight the heterogeneous materials described in the different lithostratigraphic units (Figure F29). Units IV and V were not analyzed because they were only sampled by the core catcher and were too short for NGR analysis. The top muddy silt unit with pelagic components (Unit I) is characterized by the highest NGR values observed in this hole, ranging from 9.5 to 28.0 counts/s with 16.6 counts/s on average. In Unit II, only Subunit IIB was measured. This section, which is composed of a series of serpentinitized ultramafic rocks partly filling the core liner, has very low values of less than 1 count/s. Even though the liner of the analyzed section wasn't full, these NGR values are consistent with those obtained in a full core section of similar material in Hole U1498B. Unit III consists of intercalations of different colored (blue, green, and yellow-orange) serpentinite sand and mud and is characterized by NGR values of 2–4 counts/s; the highest values are systematically located in the blue layers. The three subunits of Unit VI, which is composed of volcanoclastic deposits with variable contents of pelagic and ultramafic components, have similar NGR values ranging from 3.9 to 12.7 counts/s and averaging 8.1 counts/s.

Hole U1498B (Figure F30) is predominantly composed of ultramafic rock (Unit I) and serpentinite mud (Units III, V, and VII). Despite variations of the ratios of ultramafic rock to mud between and within these units, they all have extremely low NGR values (< 0.5 counts/s). Three relatively thin units of different material are recognized downhole by core description, and their NGR values stand out from the dominant units. Unit II, which is composed of metavolcanic and lithic clasts, shows a slight NGR increase at ~ 64 mbsf with a maximum value of 1.95 count/s. The two subsequent subunits (IVA and IVB) show a significant increase in NGR at 186–188 mbsf. In Subunit IVA, which is composed of metabasite, NGR ranges between 18.3 and 59.1 counts/s and averages 29.7 counts/s. In Subunit IVB, which is composed of metamorphosed cherty limestone, NGR ranges between 5.1 and 26.0 counts/s and averages 9.8 counts/s. Unit VI, which is located between 200.10 and 201.10 mbsf and composed of a mafic metavolcanic rock, has NGR values similar to those of Subunit IVA (metabasite), ranging from 11.0 to 48.7 counts/s with 32.3 counts/s on average. The different rock of Subunits IVA and IVB and Unit VI present relatively high deformation features, with dense fracture networks infilled with secondary material and shear bands 1 cm to several centimeters thick. The highest peak NGR values of these subunits are located near some of

these shear bands (e.g., at ~ 187.9 mbsf in Section 21R-2 and 200.8 mbsf in Section 23R-1) and may reflect significant amounts of secondary clay material precipitated in these deformation bands, although in the lower of these two rocks, the white veins are thought to be carbonate and silicate minerals. At the bottom of this hole, Unit VIII, which is composed of indurated volcanic ash deposits, is characterized by NGR ranging from 1.7 to 15.4 counts/s with 10.2 counts/s on average.

Moisture and density

Determination of MAD on discrete sediment samples was generally performed on every section of Holes U1498A and U1498B. Sampling was preferentially carried out on the most undisturbed part of a section or on rock pieces, sometimes avoiding first sections of every core. Generally, MAD values are in good agreement with GRA bulk density values.

Average bulk density for pelagic sediment on top of the serpentinite mud is 1.3 g/cm^3 , whereas for the pelagic sediment beneath the mud volcano, values are $1.7\text{--}1.9 \text{ g/cm}^3$. The serpentinite muds have mean bulk densities of $2.0\text{--}2.2 \text{ g/cm}^3$, whereas the ultramafic rock clast densities are $2.2\text{--}2.5 \text{ g/cm}^3$.

Hole U1498A has high porosity values of 80% in the pelagic sediment of Unit I, whereas Units III–V exhibit increases in porosity from 35% in the serpentinite silt and sand of Unit III to 61%–67% in the sandstone/siltstone at the bottom of the hole (Figure F31). Values between 2% and 3% represent ultramafic rock clasts (16 and 84 mbsf), and values of 23% at 16.9–17.4 mbsf are linked to metavolcanic clasts. A low porosity value at 114 mbsf corresponds to fall-in of an ultramafic rock clast. Bulk density reflects the same behavior exhibited in the porosity data. Grain density is scattered throughout the hole and ranges from 2.5 to 2.7 g/cm^3 , with the exception of a metavolcanic clast at 17 mbsf that has a value of 2.48 g/cm^3 . The highest grain density value is 2.76 g/cm^3 in the pelagic sediments of Unit I.

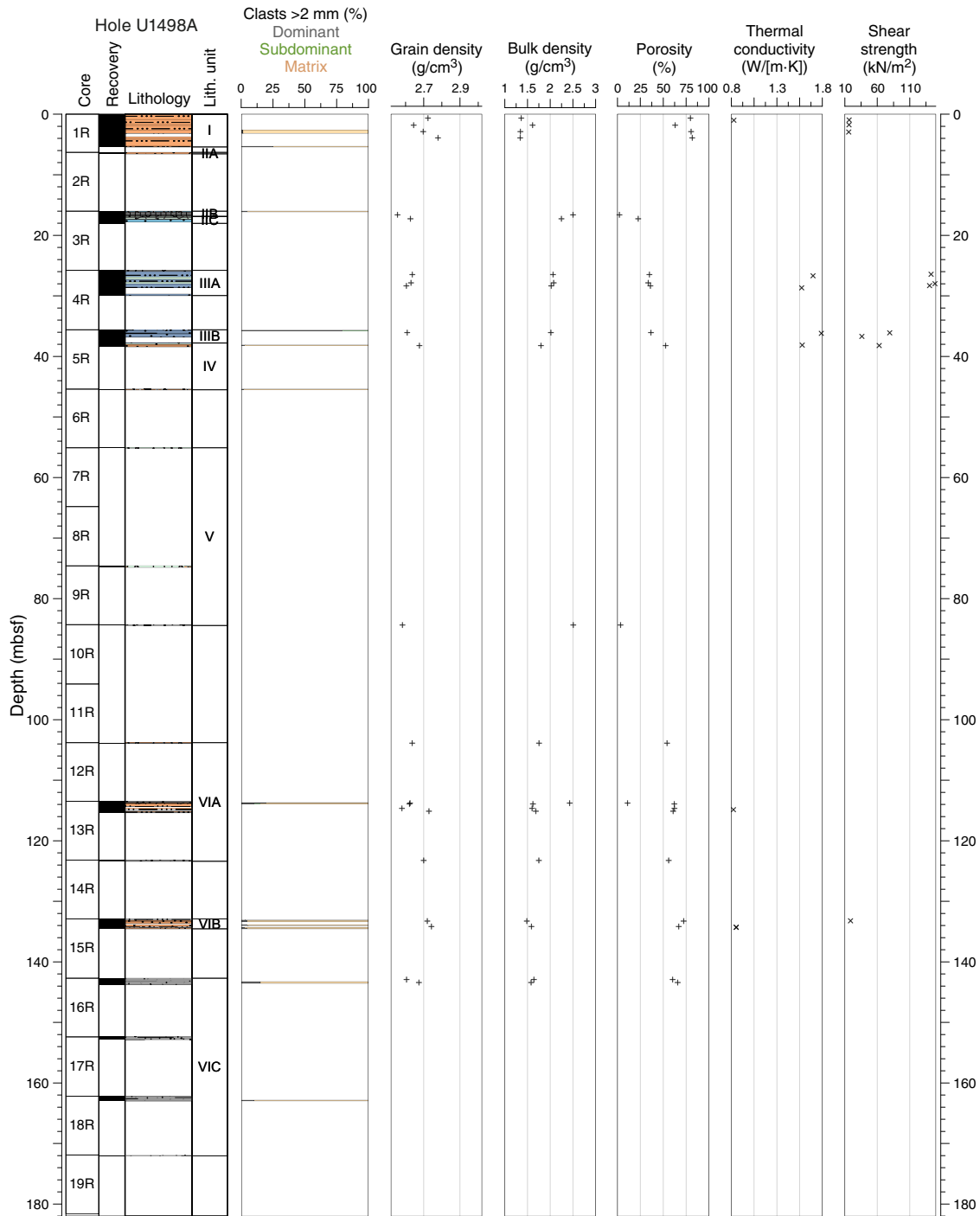
In Hole U1498B, porosity oscillates between 29% and 42% to 198 mbsf without a clear trend (Figure F32). Farther downhole, higher values of 48%–54% represent the nanofossil-bearing lithified volcanic ash of Unit VIII. Drilling disturbance is highlighted by porosities of 59%–66% measured in Core 12R. Lower porosity values between 3% and 20% at different depths in the hole are associated mainly with ultramafic rock clasts with different degrees of serpentinitization. Bulk density reflects the same behavior exhibited in the porosity data. Grain density mean values increase downhole from 2.51 to 2.69 g/cm^3 . Important outliers are the Unit II metavolcanic rock clast at 64 mbsf (2.92 g/cm^3), the Subunit IVA metabasite clast at 186 mbsf (2.91 g/cm^3), the Subunit IVB cherty limestone clast at 188 mbsf (2.80 g/cm^3), and the Unit VI metavolcanic clast at 200 mbsf (2.80 g/cm^3).

Thermal conductivity

Thermal conductivity measurements were made in Holes U1498A and U1498B at one or two per core when possible. Recovery was quite low, so measurements are sparse. Values for the two holes average $1.71 \text{ W/(m}\cdot\text{K)}$.

In Hole U1498A, the single measured Unit I value of $0.83 \text{ W/(m}\cdot\text{K)}$ is similar to values measured at other sites where pelagic sediments were recovered (see **Physical properties** in the Site U1491 chapter [Fryer et al., 2018c]). Unit II–IV values range from 1.5 to $1.8 \text{ W/(m}\cdot\text{K)}$ with no depth trend (Figure F31). In Unit VI, low values of $0.82\text{--}0.85 \text{ W/(m}\cdot\text{K)}$ were again measured, consistent with the silty mud lithology of the sediments below the seamount.

Figure F31. Index property data (grain density, bulk density, and porosity), thermal conductivity, and shear strength, Hole U1498A.



In Hole U1498B, thermal conductivity measurements were first viable at 56.4 mbsf at the base of Unit I (Figure F32). From this depth to 200 mbsf, values are fairly uniform, ranging from 1.5 to 2.0 W/(m·K). The lowest value of 1.25 W/(m·K) at 201 mbsf, measured in a mafic pebbly mud with a soupy matrix, is quite low and likely reflects drilling disturbance.

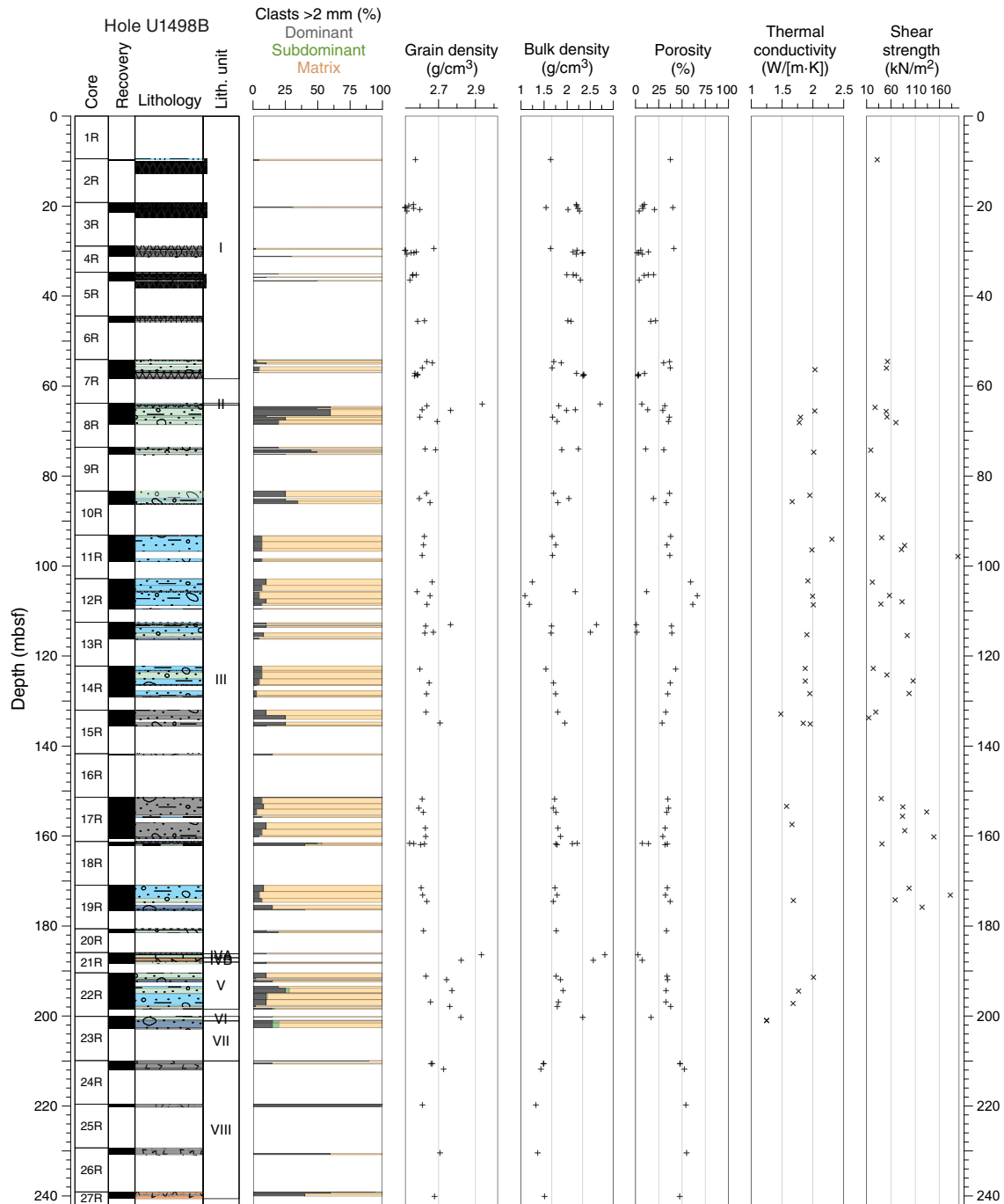
Automated vane shear

Undrained shear strength was measured with the automated vane shear in cohesive materials, but no measurements were done

in the rock-filled cores recovered throughout both Site U1498 holes. Automated vane shear data for this site are not considered representative of the formation's ultimate shear strength because the unconsolidated materials were rapidly cracking upon rotation of the vanes. This behavior was only observed in RCB cores, probably due to the high degree of disturbance to which the sediments were subjected during coring.

Hole U1498A exhibits low shear strength of 16 kN/m² in the pelagic sediments of Unit I (Figure F31) and values that increase to 141–149 kN/m² in the layered serpentinite silt and sand of Unit III.

Figure F32. Index property data (grain density, bulk density, and porosity), thermal conductivity, and shear strength, Hole U1498B.



Other values downhole are too sparse to be representative for a given unit.

Hole U1496B shows an increasing trend of mean shear strength with depth, in contrast to thermal conductivity (Figure F32). Shear strength ranges downhole between 15 and 198 kN/m². At a smaller scale, the first one or two sections of a core have systematically lower values compared to the lower sections of the same core, clearly reflecting drilling disturbance.

Discussion

Physical property measurements highlight the heterogeneous materials described in the different lithostratigraphic units of the

relatively low recovery Holes U1498A and U1498B, located at the southwestern base slope of Fantangisña Seamount. In the upper part of each hole, the units where only ultramafic rock clasts were recovered (Subunits IIA and IIB in Hole U1498A; Unit I in Hole U1498B) have physical property values consistent with those obtained on similar clasts sampled in serpentinite mud deposits from other Expedition 366 sites (see **Physical properties** in the Site U1496 chapter [Fryer et al., 2018f]). In Hole U1498B, serpentinite mud was recovered only from ~64 mbsf, which may correspond to a minimum depth to recover sufficiently consolidated/compacted mud deposits with the RCB system in comparison to the half-length APC (HLAPC) system used at other sites.

The serpentinite mud data sets are consistent with those measured along the southern flank of the Asùt Tesoru mud volcano (see **Physical properties** in the Sites U1493, U1494, and U1495 chapter [Fryer et al., 2018e]) and differ from those observed at mud volcano active summits (see **Physical properties** in the Site U1492 chapter and **Physical properties** in the Site U1496 chapter [Fryer et al., 2018d, 2018f]). In comparison to these summit sites, the serpentinite mud units have higher average bulk densities of about 2.0–2.3 g/cm³, higher *P*-wave velocities of 1700–1900 m/s, higher thermal conductivities of 1.5–2.0 W/(m·K), and lower porosities of 30%–40%. These values, obtained at a significant distance from the assumed active flow zone located at the summit of this mud volcano, may result from long-term consolidation and/or low-temperature diagenetic processes fostered by gravitational remobilization and sliding of the material along the flank.

The target of the drilling operations on this mud volcano, consisting of variably consolidated volcanic and pelagic sediment, was reached at ~104 and ~210 mbsf in Holes U1498A and U1498B, respectively. Relative to the upper serpentinite mud, these deposits have lower bulk densities of 1.5–1.7 g/cm³ and higher porosities of 50%–60%. These values probably reflect normal compaction processes compared to the overlying serpentinite mud, where additional postdepositional porosity-reducing processes (e.g., late-stage hydration of mantle and crustal materials) are occurring (see **Fluid geochemistry**).

Downhole measurements

Wireline logging was conducted in Hole U1498B after drilling to 260 mbsf. The triple combo tool string was used to measure magnetic susceptibility, NGR, electrical resistivity, borehole diameter, and borehole fluid temperature. Detailed descriptions of these logging tools are provided in **Downhole measurements** in the Expedition 366 methods chapter (Fryer et al., 2018a). No advanced piston corer temperature tool (APCT-3) temperature measurements were made in this hole.

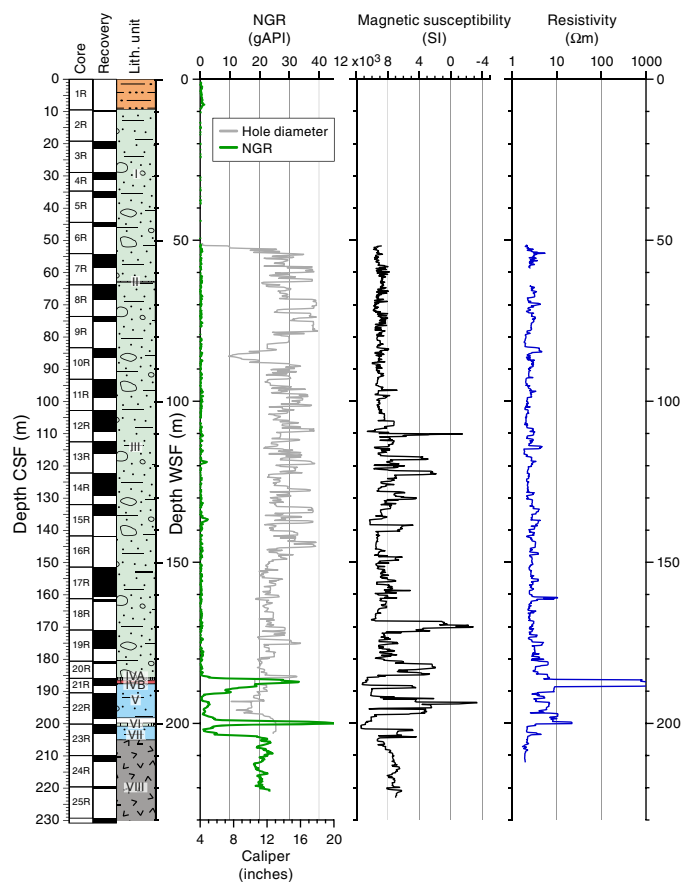
Logging included one downward pass of the tool string from the seafloor to 220 mbsf and two upward passes, the first from 220 to 105 mbsf and the second from 221 mbsf to the seafloor. Data from the second upward pass are plotted in Figure F33. The base of the drill pipe was set at 52 mbsf. Between 52 and 145 mbsf, the hole diameter varies between 12 and 18 inches; the latter is the maximum width that can be detected with the calipers. Below this depth to the bottom of the log at 200 mbsf, the average diameter is ~12 inches. In three locations, the diameter is less than 10 inches. None of these variations corresponds to a lithologic boundary.

Natural gamma radiation

The NGR logging data are effective at highlighting areas where lithologies other than serpentinite are present in Hole U1498B. The difference between NGR values inside and outside the pipe indicates that lithologies are attenuated by about a factor of 2–4 in the drill pipe. From 0 to 9 mbsf, NGR values are just above the baseline, at 1–2 gAPI, and they drop below 1 gAPI below 9 mbsf. Although there was almost no core recovered from the upper 19 m of Hole U1498B, the interval of 1–2 gAPI values likely represents 9 m of ash-rich pelagic sediment, a little thicker than the 5 m of sediment recovered in Hole U1498A, located 700 m southwest (Figure F30).

NGR values remain low to 185 mbsf, except for two small peaks at ~118 and ~137 mbsf. Shipboard NGR values measured on the cores were also low throughout these serpentinite mud units (I–III).

Figure F33. Downhole log data, core recovery, and lithostratigraphic units, Hole U1498B.



The two small NGR peaks in the log data are in locations with no recovered cores. These peaks are present at the same depth and amplitude in the NGR data from both upward logging passes. The resistivity data have no corresponding peaks, which could indicate the presence of clasts as a source of the NGR, and magnetic susceptibility values are low for the NGR peak at 137 mbsf. Thus, it is possible that these small NGR peaks may correspond to pelagic mud deposited at the seafloor between serpentinite flows.

A large NGR peak of 34 gAPI in the downhole log at 185–191 mbsf corresponds to the metabasite and cherty limestone recovered in Core 21R. A second large peak of 45 gAPI at 198–201 mbsf in the downhole log corresponds to Unit VI, which is composed of mafic metavolcanic rock recovered in Core 23R. Both of these large boulders have elevated NGR values in shipboard measurements. The boundary between the serpentinite mud and the underlying volcanic ash deposits is marked by a step in NGR values to 18–24 gAPI from 205 mbsf to the base of the log at 220 mbsf. Higher shipboard NGR values were also measured in Unit VIII on Cores 25R–27R for the corresponding depth range.

Magnetic susceptibility

Magnetic susceptibility values measured downhole in the serpentinite mud were generally low to 110 mbsf. The downhole data do not show the large spikes observed in the shipboard data between 50 and 100 mbsf (related to individual rock clasts) but are more similar to the running average, which is fairly uniform (Figure F30). Starting at about 110 mbsf to the base of the serpentinite at

205 mbsf, the downhole data have larger oscillations that were also observed in the shipboard data in the same depth intervals. The depth of the highest downhole peak at ~170 mbsf corresponds to the highest peak in the shipboard data measured in Core 19R, and the shipboard magnetic susceptibility data also are similar for Units III–VII (see **Physical properties**). Downhole data for the metabasite and limestone-chert boulders/intervals (200 and 187 mbsf) have lower magnetic susceptibility values than the surrounding serpentinite muds, which was also noted in the shipboard data. From the top of the volcanic ash to the base of the logs, the log magnetic susceptibility data were fairly uniform, as were shipboard magnetic susceptibility values for the cores recovered from this interval.

Electrical resistivity

The deep resistivity data (Figure F33) oscillate between 2 and 10 Ωm from 52 to 185 mbsf. A small peak at 113 mbsf corresponds to rock-filled Section 13R-1. Another small peak is evident at 159 mbsf, just above a rocky section collected in Section 18R-1. The largest value, over 1000 Ωm , corresponds to the cherty limestone found in Core 21R. Another peak at 200 mbsf corresponds to an 81 cm long mafic metavolcanic boulder in Unit VI.

Temperature

Borehole fluid temperatures were measured in the wireline logs. Here, they are useful for assessing the temperature perturbation caused by fluid circulation during drilling because the fluid temperature has only partially equilibrated to the formation temperature. The logged temperatures are 3.76°–4.05°C at the seafloor and 4.93°C at 220 mbsf.

Discussion

The downhole log data show good agreement with the shipboard data. The NGR log is interpreted as showing 9 m of pelagic sediments at the seabed that were not recovered in cores; it also shows the cherty limestone and metabasalt units. Two possible internal flow boundaries with pelagic sediments may be present at 118 and 137 mbsf, where NGR peaks are at similar levels to those in the Unit I ash-rich pelagic sediments. Moreover, there is no evidence in the resistivity data that these peaks are due to sedimentary clasts. The resistivity data are useful for highlighting very large clasts.

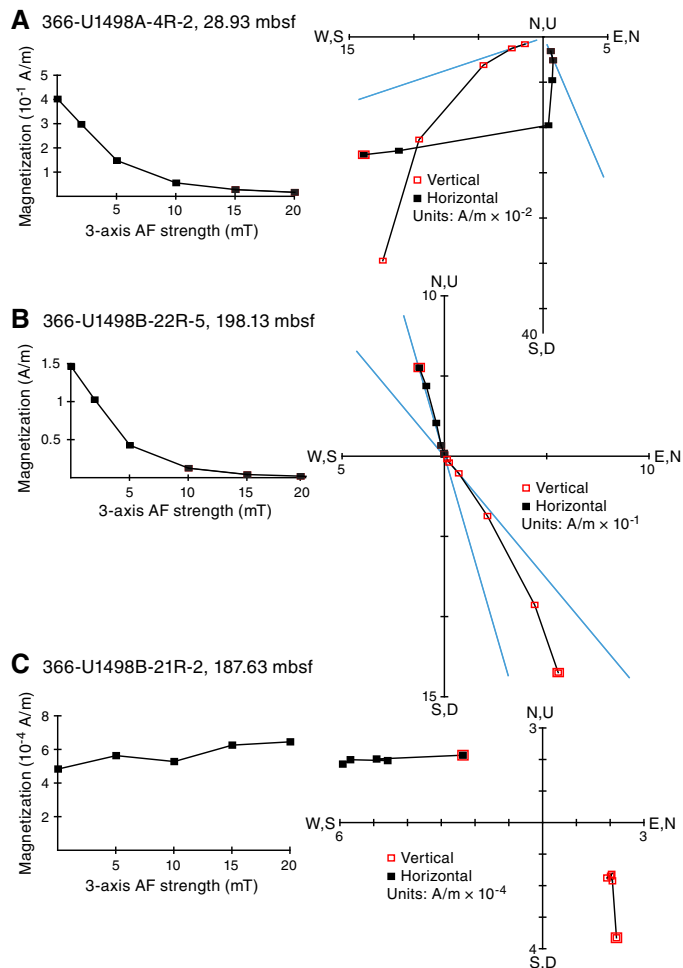
Paleomagnetism

The natural remanent magnetizations (NRM) of all archive section halves of cores from Holes U1498A and U1498B were measured at 5 cm intervals after 0, 5, 10, 15, and 20 mT alternating field (AF) demagnetization using the shipboard SRM. The NRM of 34 representative discrete samples from Hole U1498A and 54 from Hole U1498B were measured after 0–20 mT AF demagnetization using the SRM. Cores with gravel and randomly oriented rock clasts were not measured. Bulk magnetic susceptibility was measured in 24 discrete samples of representative types of rock clasts from Holes U1498A and U1498B using an AGICO KLY 4S Kappabridge instrument. RCB coring was used at this site, so declination values are only useful within coherent sections of core.

Results

The principal component analyses (PCA) of some discrete samples were performed on samples from different lithologies (Figure F34). For archive section halves, we analyzed NRM inclination, dec-

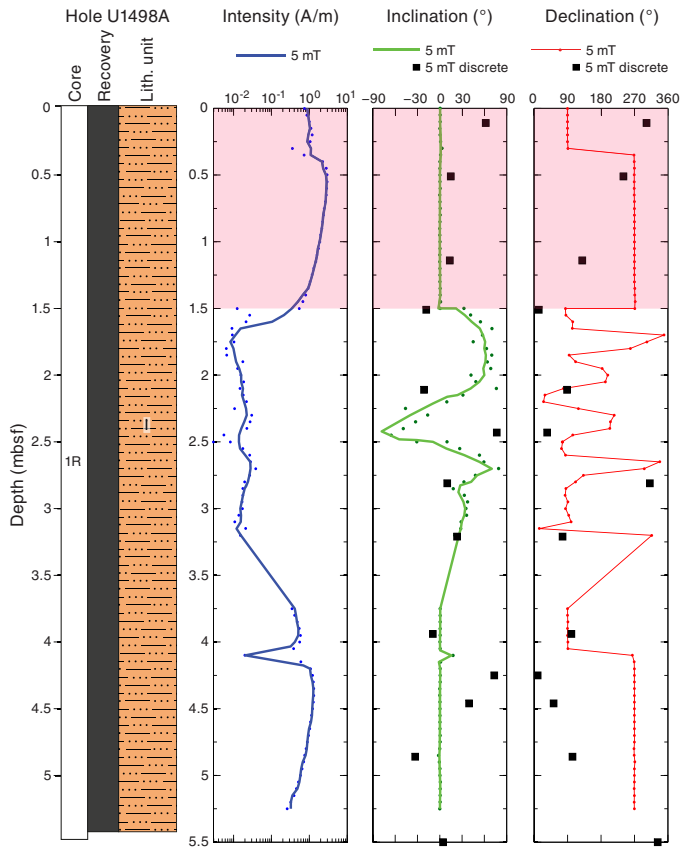
Figure F34. NRM decay (left) and AF demagnetization vector (right) diagrams of discrete samples, Site U1498. A. 366-U1498A-4R-2, 27.93 mbsf. B. 366-U1498B-22R-5, 196.93 mbsf. C. 366-U1498B-21R-2, 187.63 mbsf. Demagnetization diagrams: points = projected endpoints of the remanent magnetization vector measured for each sample in core coordinates, blue lines = principal component directions from discrete samples, open symbols = vector endpoints projected on a vertical plane, solid symbols = vector endpoints projected on a horizontal plane.



ination, and intensity on pelagic sediments from Unit I in Hole U1498A. NRM values after 5 mT AF demagnetization show a strong horizontal overprint in the upper 1.5 m of Hole U1498A (Figure F35). However, this pattern was not observed in the discrete samples from the same interval (a similar horizontal overprint pattern also occurs at Sites U1491 and U1492). Similar to Site U1497, most Hole U1498A and U1498B unconsolidated materials are not ideal for recording NRM inclination and declination. A vertical overprint, likely caused by the drilling process, is also present in most serpentinite mud intervals. The volcanic ash-rich sediment beneath the serpentinite muds is less affected by this overprint, but the relatively low recovery in this interval makes it near-impossible to construct a magnetostratigraphy, even if the original paleomagnetic direction could be isolated.

A relatively high NRM intensity value of $\sim 1.5 \times 10^{-1}$ A/m occurs in the dark layers within the serpentine sand and silt sequence from Subunit IIIA in Hole U1498A at 27.3–28.6 mbsf (Figure F36). The NRM of the ash-rich sediments from 113 to 145 mbsf in Hole

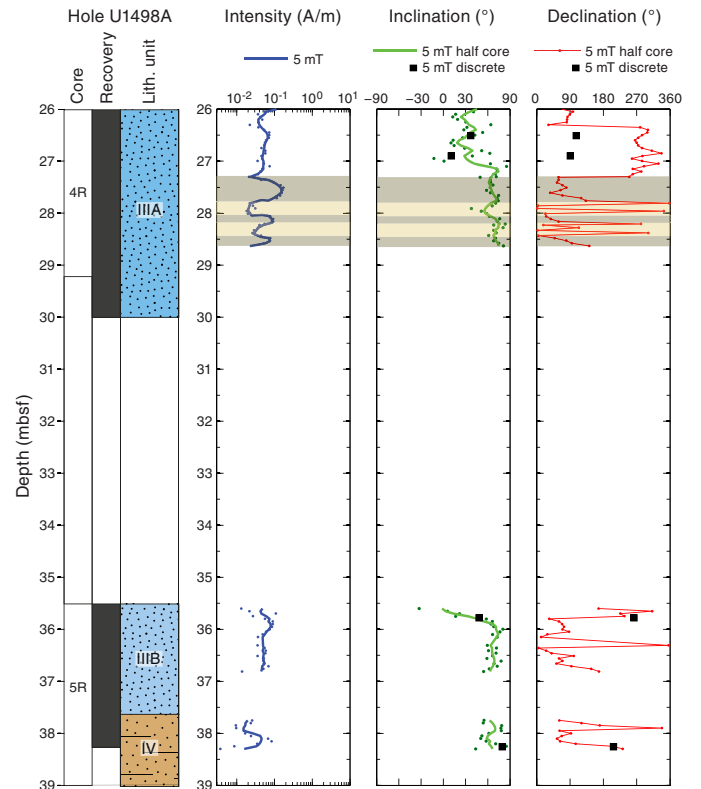
Figure F35. Paleomagnetic intensity, inclination, and declination of archive halves and discrete samples after 5 mT AF demagnetization, 0–5.2 mbsf, Hole U1498A. Pink rectangle = area of strong horizontal overprint. Both original data (dots) and running mean (line) are shown for intensity and inclination.



U1498A was taken from a low-recovery interval, and therefore we make no interpretation of paleomagnetic polarity (Figure F37). Some intervals with ultramafic clasts from Hole U1498B, Unit III (Figure F38) and Unit V (Figure F39), both composed of bluish gray serpentinite pebbly mud with lithic clasts, reach NRM intensity values of about 1 A/m after 5 mT AF demagnetization. An intermediate average NRM intensity of $\sim 2.0 \times 10^{-2}$ A/m occurs in Hole U1498B sections from Subunit IVA and Unit VI, corresponding to metabasite and mafic metavolcanic rock (greenstone), whereas the lowest NRM intensity of $\sim 5.5 \times 10^{-4}$ A/m corresponds to cherty limestone clasts from Subunit IVB (i.e., Section 366-U1498B-21R-2; 187.63 mbsf).

The NRM intensity in the volcanic ashes of Subunit VIC (Core 366-U1498A-16R) (Figure F37) is 6×10^{-2} A/m and slightly higher compared to a slightly lower intensity of $\sim 1.8 \times 10^{-2}$ A/m in the Unit VIII volcanic ashes from the base of Hole U1498B (Figure F39).

Figure F36. Paleomagnetic intensity, inclination, and declination of archive halves and discrete samples after 5 mT AF demagnetization, 26–39 mbsf, Hole U1498A. Core 4R layered serpentinite silt and sand with beds of pelagic sediment: gray shading = relatively high NRM intensities, yellow shading = relatively low NRM intensities. Both original data (dots) and running mean (line) are shown for intensity and inclination.



Bulk magnetic susceptibility values from different types of clasts corroborate the NRM variation. In Hole U1498B, the lowest values ($\sim 3.0 \times 10^{-4}$) occur in clasts in Section 21R-2 (cherty limestone), intermediate values of $\sim 2.0 \times 10^{-3}$ were observed in the mafic rocks of Section 21R-1, and the highest values of $\sim 2.0 \times 10^{-2}$ occur in the peridotite clasts of Section 23R-3 and some volcanic ashes (e.g., Section 24R-2) (Figure F39).

Differences in NRM intensities registered in Cores 366-U1498A-4R and 5R (Subunit IIIA; layered serpentinite silt and sand with beds of pelagic sediment; see Lithostratigraphy) may originate from higher concentrations of magnetite in the serpentinite intervals, which leads to higher magnetization and bulk magnetic susceptibility (Figure F36). These two cores may be more suitable for paleomagnetic analysis than the more common clast-rich serpentinite mudflows. However, inclination values remain too high ($>60^\circ$) for the latitude at this site.

Figure F37. Paleomagnetic intensity, inclination, and declination of archive halves and discrete samples after 5 mT AF demagnetization from the volcanic ash-rich units of Hole U1498A. Both original data (dots) and running mean (line) are shown for intensity and inclination.

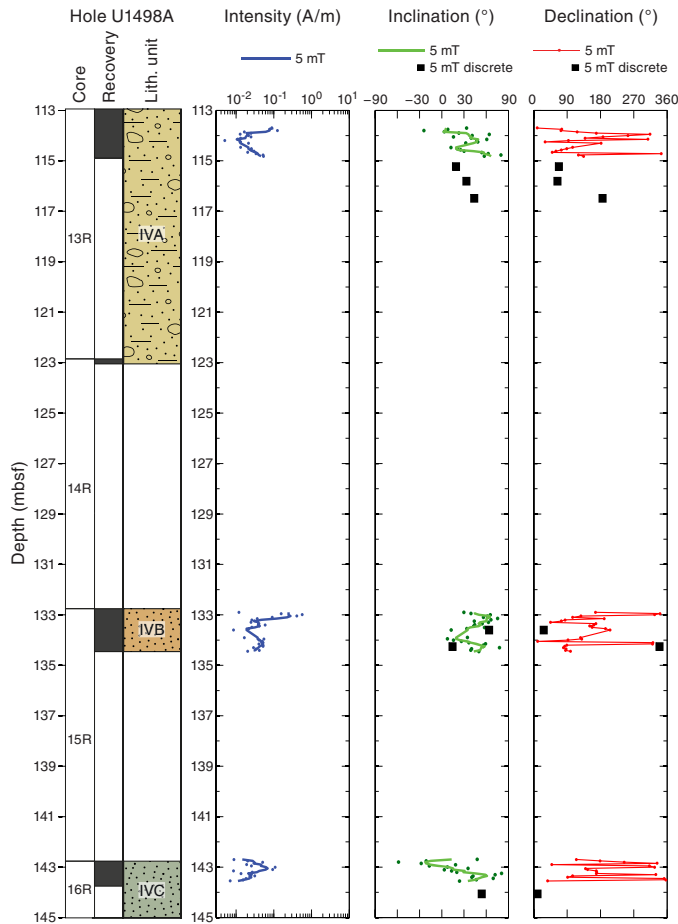


Figure F38. Paleomagnetic intensity, inclination, and declination of archive halves and discrete samples after 5 mT AF demagnetization from the serpentinite mud units of Hole U1498B. Both original data (dots) and running mean (line) are shown for intensity and inclination.

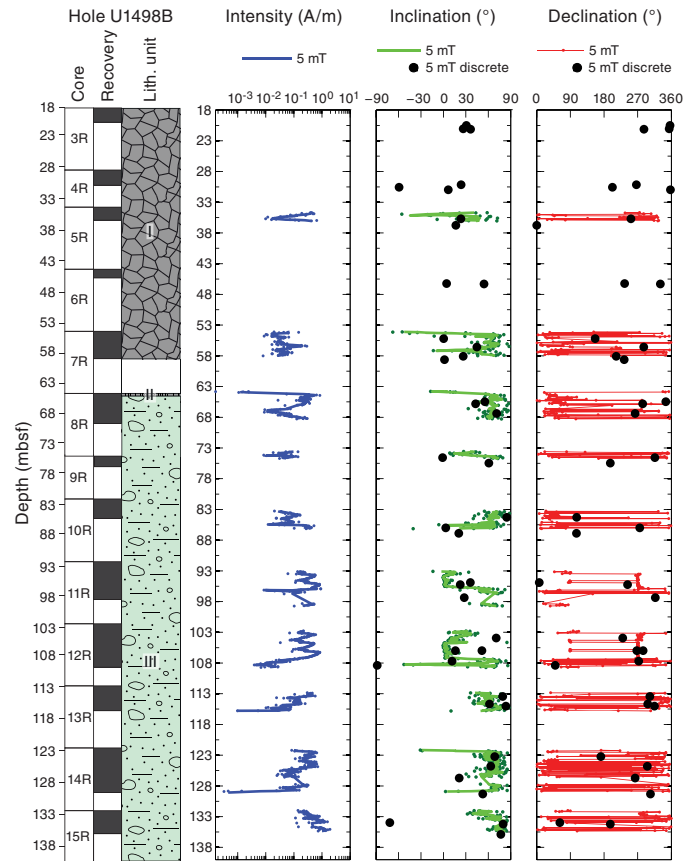
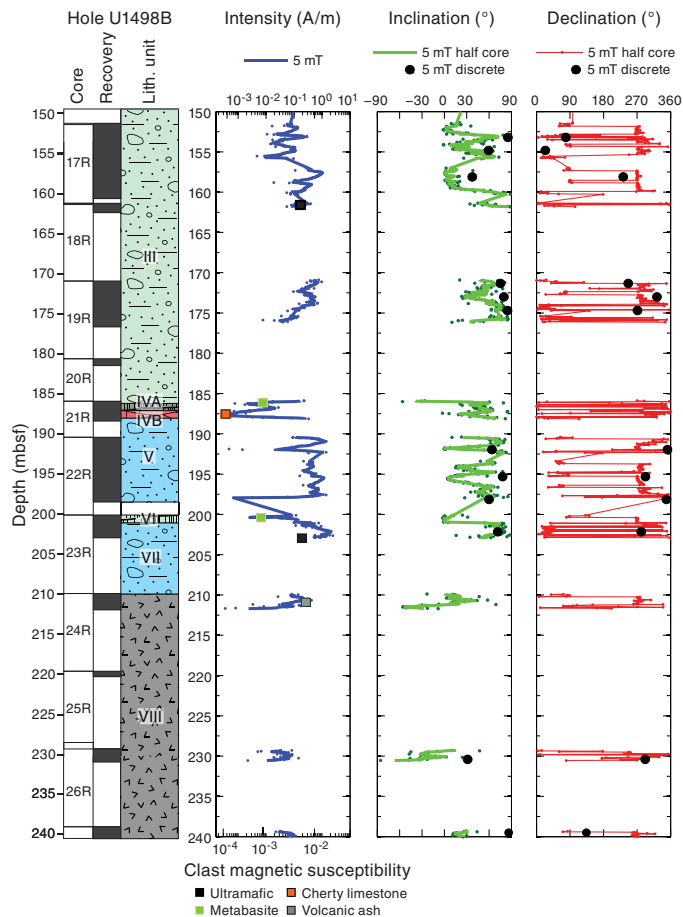


Figure F39. Paleomagnetic intensity, inclination, and declination of archive halves and discrete samples after 5 mT AF demagnetization from the lower part of Hole U1498B. Both original data (dots) and running mean (line) are shown for intensity and inclination.



References

- Eglinton, T.I., and Repeta, D.J., 2014. Organic matter in the contemporary ocean. In Mottl, M.J., and Elderfield, H. (Eds.), *Treatise on Geochemistry* (2nd Edition) (Volume 8): *The Oceans and Marine Geochemistry*. Holland, H.D., and Turekian, K.K. (Series Eds.): Oxford, United Kingdom (Elsevier), 151–189.
<https://doi.org/10.1016/B978-0-08-095975-7.00606-9>
- Fryer, P., Wheat, C.G., and Williams, T., 2016. *Expedition 366 Scientific Prospectus: Mariana Serpentine Mud Volcanism*. International Ocean Discovery Program. <https://doi.org/10.14379/iodp.sp.366.2016>
- Fryer, P., Wheat, C.G., Williams, T., Albers, E., Bekins, B., Debret, B.P.R., Deng, J., Dong, Y., Eickenbusch, P., Frery, E.A., Ichiyama, Y., Johnson, K., Johnston, R.M., Kevorkian, R.T., Kurz, W., Magalhaes, V., Mantovanelli, S.S., Menapace, W., Menzies, C.D., Michibayashi, K., Moyer, C.L., Mullan, K.K., Park, J.-W., Price, R.E., Ryan, J.G., Shervais, J.W., Sissmann, O.J., Suzuki, S., Takai, K., Walter, B., and Zhang, R., 2018a. Expedition 366 methods. In Fryer, P., Wheat, C.G., Williams, T., and the Expedition 366 Scientists, *Mariana Convergent Margin and South Chamorro Seamount*. Proceedings of the International Ocean Discovery Program, 366: College Station, TX (International Ocean Discovery Program).
<https://doi.org/10.14379/iodp.proc.366.102.2018>
- Fryer, P., Wheat, C.G., Williams, T., Albers, E., Bekins, B., Debret, B.P.R., Deng, J., Dong, Y., Eickenbusch, P., Frery, E.A., Ichiyama, Y., Johnson, K., Johnston, R.M., Kevorkian, R.T., Kurz, W., Magalhaes, V., Mantovanelli, S.S., Menapace, W., Menzies, C.D., Michibayashi, K., Moyer, C.L., Mullan, K.K., Park, J.-W., Price, R.E., Ryan, J.G., Shervais, J.W., Sissmann, O.J., Suzuki, S., Takai, K., Walter, B., and Zhang, R., 2018b. Expedition 366 summary. In Fryer, P., Wheat, C.G., Williams, T., and the Expedition 366 Scientists, *Mariana Convergent Margin and South Chamorro Seamount*. Proceedings of the International Ocean Discovery Program, 366: College Station, TX (International Ocean Discovery Program).
<https://doi.org/10.14379/iodp.proc.366.101.2018>
- Fryer, P., Wheat, C.G., Williams, T., Albers, E., Bekins, B., Debret, B.P.R., Deng, J., Dong, Y., Eickenbusch, P., Frery, E.A., Ichiyama, Y., Johnson, K., Johnston, R.M., Kevorkian, R.T., Kurz, W., Magalhaes, V., Mantovanelli, S.S., Menapace, W., Menzies, C.D., Michibayashi, K., Moyer, C.L., Mullan, K.K., Park, J.-W., Price, R.E., Ryan, J.G., Shervais, J.W., Sissmann, O.J., Suzuki, S., Takai, K., Walter, B., and Zhang, R., 2018c. Site U1491. In Fryer, P., Wheat, C.G., Williams, T., and the Expedition 366 Scientists, *Mariana Convergent Margin and South Chamorro Seamount*. Proceedings of the International Ocean Discovery Program, 366: College Station, TX (International Ocean Discovery Program).
<https://doi.org/10.14379/iodp.proc.366.104.2018>
- Fryer, P., Wheat, C.G., Williams, T., Albers, E., Bekins, B., Debret, B.P.R., Deng, J., Dong, Y., Eickenbusch, P., Frery, E.A., Ichiyama, Y., Johnson, K., Johnston, R.M., Kevorkian, R.T., Kurz, W., Magalhaes, V., Mantovanelli, S.S., Menapace, W., Menzies, C.D., Michibayashi, K., Moyer, C.L., Mullan, K.K., Park, J.-W., Price, R.E., Ryan, J.G., Shervais, J.W., Sissmann, O.J., Suzuki, S., Takai, K., Walter, B., and Zhang, R., 2018d. Site U1492. In Fryer, P., Wheat, C.G., Williams, T., and the Expedition 366 Scientists, *Mariana Convergent Margin and South Chamorro Seamount*. Proceedings of the International Ocean Discovery Program, 366: College Station, TX (International Ocean Discovery Program).
<https://doi.org/10.14379/iodp.proc.366.105.2018>
- Fryer, P., Wheat, C.G., Williams, T., Albers, E., Bekins, B., Debret, B.P.R., Deng, J., Dong, Y., Eickenbusch, P., Frery, E.A., Ichiyama, Y., Johnson, K., Johnston, R.M., Kevorkian, R.T., Kurz, W., Magalhaes, V., Mantovanelli, S.S., Menapace, W., Menzies, C.D., Michibayashi, K., Moyer, C.L., Mullan, K.K., Park, J.-W., Price, R.E., Ryan, J.G., Shervais, J.W., Sissmann, O.J., Suzuki, S., Takai, K., Walter, B., and Zhang, R., 2018e. Sites U1493, U1494, and U1495. In Fryer, P., Wheat, C.G., Williams, T., and the Expedition 366 Scientists, *Mariana Convergent Margin and South Chamorro Seamount*. Proceedings of the International Ocean Discovery Program, 366: College Station, TX (International Ocean Discovery Program).
<https://doi.org/10.14379/iodp.proc.366.106.2018>
- Fryer, P., Wheat, C.G., Williams, T., Albers, E., Bekins, B., Debret, B.P.R., Deng, J., Dong, Y., Eickenbusch, P., Frery, E.A., Ichiyama, Y., Johnson, K., Johnston, R.M., Kevorkian, R.T., Kurz, W., Magalhaes, V., Mantovanelli, S.S., Menapace, W., Menzies, C.D., Michibayashi, K., Moyer, C.L., Mullan, K.K., Park, J.-W., Price, R.E., Ryan, J.G., Shervais, J.W., Sissmann, O.J., Suzuki, S., Takai, K., Walter, B., and Zhang, R., 2018f. Site U1496. In Fryer, P., Wheat, C.G., Williams, T., and the Expedition 366 Scientists, *Mariana Convergent Margin and South Chamorro Seamount*. Proceedings of the International Ocean Discovery Program, 366: College Station, TX (International Ocean Discovery Program).
<https://doi.org/10.14379/iodp.proc.366.107.2018>
- Johnston, R.M., and Ryan, J.G., 2018. pXRF and ICP-AES characterization of shipboard rocks and sediments: protocols and strategies. In Fryer, P., Wheat, C.G., Williams, T., and the Expedition 366 Scientists, *Mariana Convergent Margin and South Chamorro Seamount*. Proceedings of the International Ocean Discovery Program, 366: College Station, TX (International Ocean Discovery Program).
<https://doi.org/10.14379/iodp.proc.366.110.2018>
- Mottl, M.J., 1992. Pore waters from serpentinite seamounts in the Mariana and Izu-Bonin forearcs, Leg 125: evidence for volatiles from the subducting slab. In Fryer, P., Pearce, J.A., Stokking, L.B., et al., *Proceedings of the Ocean Drilling Program, Scientific Results*, 125: College Station, TX (Ocean Drilling Program), 373–385.
<https://doi.org/10.2973/odp.proc.sr.125.121.1992>
- Mottl, M.J., Komor, S.C., Fryer, P., and Moyer, C.L., 2003. Deep-slab fluids fuel extremophilic Archaea on a Mariana forearc serpentinite mud volcano:

- Ocean Drilling Program Leg 195. *Geochemistry, Geophysics, Geosystems*, 4:9009. <https://doi.org/10.1029/2003GC000588>
- Mottl, M.J., Wheat, C.G., Fryer, P., Gharib, J., and Martin, J.B., 2004. Chemistry of springs across the Mariana forearc shows progressive devolatilization of the subducting plate. *Geochimica et Cosmochimica Acta*, 68(23):4915–4933. <https://doi.org/10.1016/j.gca.2004.05.037>
- Oakley, A., 2008. A multi-channel seismic and bathymetric investigation of the central Mariana convergent margin [Ph.D. dissertation]. University of Hawaii. <http://www.soest.hawaii.edu/GG/resources/theses/OakleyDissertation2008.pdf>
- Oakley, A.J., Taylor, B., Fryer, P., Moore, G.F., Goodliffe, A.M., and Morgan, J.K., 2007. Emplacement, growth, and gravitational deformation of ser-pentinite seamounts on the Mariana forearc. *Geophysical Journal International*, 170(2):615–634. <https://doi.org/10.1111/j.1365-246X.2007.03451.x>
- Oakley, A.J., Taylor, B., and Moore, G.F., 2008. Pacific plate subduction beneath the central Mariana and Izu-Bonin fore arcs: new insights from an old margin. *Geochemistry, Geophysics, Geosystems*, 9(6):Q06003. <https://doi.org/10.1029/2007GC001820>
- Rognstad, M., 1992. HAWAII MR1: a new underwater mapping tool [paper presented at the International Conference on Signal Processing and Technology, Cambridge, Massachusetts, 2–5 November 1992]. <http://www.soest.hawaii.edu/hmrg/facstaff/mark/MR1Paper.pdf>